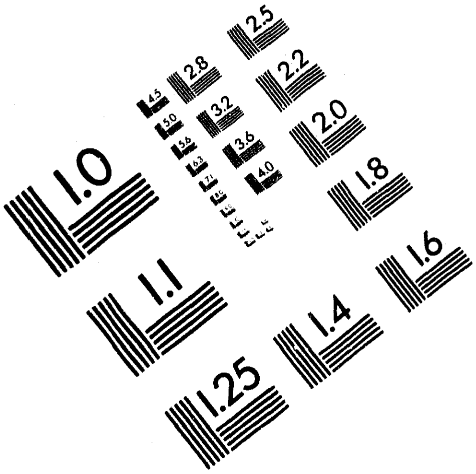

AIIM

Association for Information and Image Management

1100 Wayne Avenue, Suite 1100
Silver Spring, Maryland 20910

301/587-8202

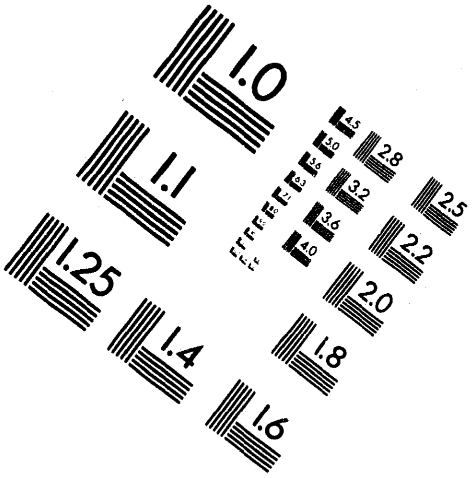

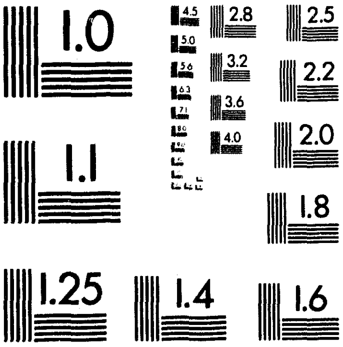

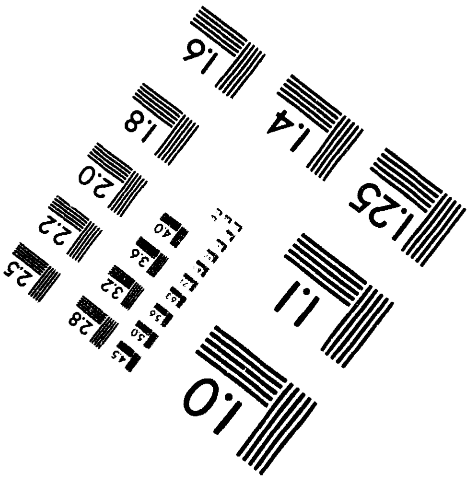

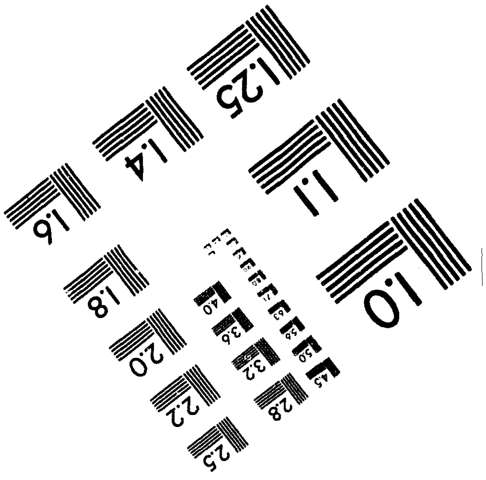

MANUFACTURED TO AIIM STANDARDS
BY APPLIED IMAGE, INC.

1 of 2

DOE/BC/14885-5
Distribution Category UC-122

DEVELOPMENT OF COST-EFFECTIVE SURFACTANT FLOODING TECHNOLOGY

First Annual Report for the Period
September 30, 1992 to September 29, 1993

by
Gary A. Pope
Kamy Sepehrnoori

August 1994

Work Performed Under Contract No. DE-AC22-92BC14885

Prepared for
U.S. Department of Energy
Assistant Secretary for Fossil Energy

Jerry Casteel, Project Manager
Bartlesville Project Office
P.O. Box 1398
Bartlesville, OK 74005

Prepared by
The University of Texas
Center for Petroleum and Geosystems Engineering
Austin, TX 78712

TABLE OF CONTENTS

LIST OF FIGURES

LIST OF TABLES

ABSTRACT

This research consists of the parallel development of a new chemical flooding simulator and the application of our existing UTCHEM simulation code to model surfactant flooding. The new code is based upon a completely new numerical method that combines for the first time higher order finite difference methods, flux limiters, and implicit algorithms. Early results indicate that this approach has significant advantages in some problems and will likely enable us to simulate much larger and more realistic chemical floods once it is fully developed. Additional improvements have also been made to the UTCHEM code and it has been applied for the first time to the study of stochastic reservoirs with and without horizontal wells to evaluate methods to reduce the cost and risk of surfactant flooding. During the first year of this contract, we have already made significant progress on both of these tasks and are ahead of schedule on both of them. We have found that there are indeed significant differences between the performance predictions based upon the traditional layered reservoir description and the more realistic and flexible descriptions using geostatistics. Our preliminary studies of surfactant flooding using horizontal wells shows that although they have significant potential to greatly reduce project life and thus improve the economics of the process, their use requires accurate reservoir descriptions and simulations to be effective. Much more needs to be done to fully understand and optimize their use and develop reliable design criteria.

EXECUTIVE SUMMARY

The objective of this research is to develop cost-effective surfactant flooding technology by using surfactant simulation studies to evaluate and optimize alternative design strategies taking into account reservoir characteristics, process chemistry, and process design options such as horizontal wells. Task 1 is the development of an improved numerical method for our simulator that will enable us to solve a wider class of these difficult simulation problems accurately and affordably. Task 2 is to apply numerical simulation to better understand and optimize the design of surfactant flooding to reduce its cost and risk.

A new algorithm that is fully implicit and higher order in both time and space has been developed. This algorithm combines the best features of several recent numerical schemes since it is both accurate and stable. Preliminary results on several one and two-dimensional test problems with known solutions look very good compared to standard finite-difference methods used in reservoir simulation including our own version of the total variation diminishing (TVD) flux limited, higher order, implicit pressure-explicit saturation method (IMPES) now used in UTCHEM. The computational efficiency of several solvers and timestepping algorithms have been evaluated by simulating two-dimensional waterfloods and polymerfloods. The code is being extended to three dimensions and additional physical and chemical properties added toward the goal of a model that is as complete as UTCHEM but computationally more efficient.

UTCHEM development has continued and several significant improvements have been made in the code during the past year. These improvements have the combined effect of making the code more versatile and efficient, which serves not only our needs better but that of a large number of external users. These users consist of not only the industrial sponsors of our enhanced oil recovery research at the University of Texas at Austin, but also a large and increasing number of academic users who use our code in a variety of oil recovery research. These users now include the following organizations:

ADREF	Amoco Production Co.
ARAMCO	Arco Oil & Gas Co.
BP Exploration, Inc.	Chevron Oil Field Research Co.
Conoco, Inc.	Cray Research

DOE	Duke University
Elf Aquitaine	Exxon Production Research Company
Idaho National Laboratories	Institute for Energy Technology
INTERA, Inc.	INTEVEP, S.A.
Japan National Oil Corp.	Japan Petroleum Exploration Co., Ltd.
Louisiana State University	Marathon Oil Company
Mobil Exploration and Producing Services	New Mexico Recovery Research Center
Norsk Hydro	Oryx Energy Co.
Oxy USA, Inc.	Pacific Northwest Laboratories
Rice University	Rogaland Research Institute
Sandia National Laboratories	Santa Fe Energy Resources
Scientific Computing Associates, Inc.	Shell Development Co.
Stanford University	Statoil
Technical University of Clausthal, Germany	Technical University of Denmark
Texaco, Inc.	Union Pacific Resources
University of Buenos Aires	University of Kansas
University of Michigan	University of Mining and Metallurgy - Poland
University of Oklahoma	University of Wyoming
UNOCAL	

A significant effort is required to provide the code and its documentation to these users as well as some support on its use. However, we do benefit from feedback from these users and occasionally even new features to the code. In addition to these application users, we also have a major collaborative research effort with the Computational and Applied Mathematics group led by Professor Mary Wheeler at Rice University to port UTCHEM to massively parallel computers as well as to develop new algorithms for future use. This research is sponsored by the High Performance Computing and Communications program of the federal government. This research is targeted at the use of massively parallel computers to solve Grand Challenge problems, which in our case means flow in permeable media problems with applications to both oil recovery and groundwater remediation. Some of our most recent UTCHEM development targeted to contaminant cleanup is sponsored by the Environmental Protection Agency. This effort includes such things as the addition of local mesh refinement, which will be very valuable to all of our applications. Thus, there is a large leverage on the research funds provided by this grant among other benefits to this related activity.

UTCHEM has been applied for the first time to the simulation of surfactant flooding using geostatistical reservoir descriptions. This approach enables us to make more realistic simulations and lends itself to the assessment of uncertainty in the results far better than the traditional layered reservoir description approach we and others have used in the past to simulate surfactant flooding. Although this study is not complete, several important conclusions have already emerged. The rate at which the surfactant and polymer can be injected into the reservoir and hence the economically important project life of the chemical flood varies strongly with the correlation length of the reservoir. The limiting case of infinite correlation length corresponding to a layered reservoir is optimistic in this respect. These and other results from our study to date show as expected a much greater sensitivity of the surfactant flood to reservoir description than waterflooding. This knowledge can be used not only to better understand the problem but to make good engineering decisions about which reservoir characterization data and how much data are justified and cost effective for surfactant flooding.

UTCHEM has also been applied for the first time to the simulation of surfactant flooding using horizontal wells. This study has just started and is very preliminary and the impact of horizontal wells is complex since it depends on many variables, but several economically important conclusions have already emerged from this study as well. The location of the horizontal well is extremely important and must be in a reasonably permeable layer of the reservoir to be effective. Otherwise, both the oil recovery and injectivity may be low. A horizontal injector and vertical producer is likely to be the optimum combination for most surfactant floods. The injectivity is very sensitive to vertical permeability at low ratios of vertical to horizontal permeability for both vertical and horizontal wells, but is even more important for horizontal wells since the more expensive horizontal wells must be very effective to justify their cost. We have done these studies for both layered and stochastic reservoir descriptions and have found significant differences. Furthermore, heterogeneity must be taken into account when simulating surfactant flooding with horizontal wells to arrive at even qualitatively correct trends. Thus, the limited results in the literature are misleading and should not be used as an indication of the potential of horizontal wells. The oil recovery from surfactant flooding using horizontal wells is even more sensitive to accurate reservoir description than it is with vertical wells and one of our most important challenges will be to quantify the degree of accuracy needed to use horizontal wells economically.

HIGH-RESOLUTION, FULLY IMPLICIT, COMPOSITIONAL SIMULATION

Introduction

The objective of this research is to develop cost-effective surfactant flooding technology by using surfactant simulation studies to evaluate and optimize alternative design strategies taking into account reservoir characteristics, process chemistry, and process design options such as horizontal wells. Task 1 is the development of an improved numerical method for our simulator that will enable us to solve a wider class of these difficult simulation problems accurately and affordably.

Compositional simulators with an IMPES formulation solve for pressure implicitly using a time-lagged mobility function and subsequently update the saturations or concentrations explicitly. This is the fastest approach on a per-timestep basis, but it can introduce stability problems that restrict the timestep size. The Courant stability criterion for an explicit scheme always requires a limited timestep size. The explicit updating of saturations or concentrations is one source of instability. The time-lagged and pressure-dependent mobility terms in the pressure equation are also sources of instability. This instability can arise from shear-dependent viscosities in polymer flooding or from the capillary number dependence of relative permeabilities in surfactant flooding. The stability restrictions means that the simulation cost for very large field problems is still high or even not feasible for sufficiently large problems.

The fully implicit method is the most stable method, where the pressure equation and the component conservation equations are solved simultaneously with the nonlinear functions of the interface flow terms evaluated at the new timestep. This approach, however, usually requires more computational work than other methods on a per-timestep basis, particularly for large grids. Furthermore, the program coding is more complicated and the implementation of the physical property models is more difficult. Because of these restrictions, standard implicit methods usually adopt lower-order finite-difference schemes for both the temporal and spatial discretizations and the advantage of the methods are overshadowed by the increased amount of numerical dispersion associated with large truncation error. This is important in all reservoir simulation problems, but it is especially important in surfactant flooding because of its complex behavior and high cost. We need accurate field simulation so that we can design the floods at a minimum cost and risk.

The solution to this dilemma and what we have done in Task 1 is to develop a new fully implicit algorithm. It is second-order correct in time and uses a third-order finite-difference method to discretize the first-order space derivatives and a new total variation diminishing flux limiter to constrain the gradients of the fluxes to obtain accurate, oscillation-free numerical solutions (Saad *et al.*, 1990; Datta Gupta *et al.*, 1991; Liu *et al.*, 1993). This algorithm combines the best features of several recent numerical schemes since it is both stable and accurate. Unlike many numerical schemes in the literature, there are no problems with generalizations of this scheme to multidimensional, multicomponent, multiphase flow problems such as those arising in the simulation of compositional chemical flow problems that are the specific focus of this project. Preliminary results look very good compared to the use of standard finite-difference methods. The overall increase in accuracy through the use of the TVD flux-limited high-order method and the fully implicit formulation makes it possible to reduce the overall computational cost by taking larger timestep sizes and fewer nonlinear iterations without sacrificing accuracy or stability. The effects of different solvers and timestepping algorithms on the computational efficiency were also studied. Improved computing technologies, including large-scale vector and parallel architectures, and the development of more efficient and robust solution solvers have made the application of this fully implicit algorithm more realistic.

Physical and Mathematical Model

In an oil reservoir, molecular species can undergo transport within phases and exchange across phase boundaries. For example, many enhanced oil recovery processes rely on the effects of interphase mass transfer to alter fluid properties in ways that benefit oil production. The simulation of any of these phenomena requires a fully compositional formulation. For a mathematical model of chemical flooding processes, we simulate multiphase, multicomponent three-dimensional flow in porous media. The basic governing equations consist of a mass conservation equation for each component, an energy balance, Darcy's law generalized for multiphase flow, and an overall mass conservation or continuity equation that determines the pressure. Various phenomena such as velocity-dependent dispersion, adsorption, chemical reactions, complex phase behavior, variable phase viscosities and relative permeabilities are required to model chemical transport in oil reservoirs. The major assumptions used in the development of our mathematical model for chemical flooding processes are given by Saad, 1989 and Delshad *et al.*, 1994. Various other assumptions and detailed discussions of formulating specific physical models can be found in Pope and Nelson (1978), Datta Gupta *et al.* (1986), Camilleri *et al* (1987), Bhuyan *et al.* (1988), and Delshad *et al.* (1994).

Mass conservation equations

With the slightly compressible flow assumptions, the mass balance equation for component κ is (Saad, 1989; Delshad *et al.*, 1994)

$$\phi_R \frac{\partial}{\partial t} \{\tilde{C}_\kappa [1+(C_f+C_\kappa^0)\,\Delta P_R]\}$$

$$+ \vec{\nabla}\cdot(1+C_\kappa^0 \Delta P_R) \sum_{\ell=1}^{n_p} (C_{\kappa\ell}\vec{u}_\ell - \phi S_\ell\, \vec{\vec{K}}_{\kappa\ell}\cdot\vec{\nabla}C_{\kappa\ell}) = q_\kappa$$

$$\kappa = 1, \ldots, n_c\,. \qquad (1)$$

The compressibility effects are functions of the pressure change ΔP, defined as

$$\Delta P_R = P_R - P_{R0}\,, \qquad (2)$$

where P_R is the pressure of a reference phase and P_{R0} is the pressure at which all compressibility reference values are defined. C_f is the pore volume compressibility and C_κ^0 is the compressibility of component κ. The overall concentration of each component κ is given by

$$\tilde{C}_\kappa = (1-\sum_{\kappa=1}^{n_{cv}} \hat{C}_\kappa) \sum_{\ell=1}^{n_p} S_\ell C_{\kappa\ell} + \hat{C}_\kappa \, , \tag{3}$$

where n_{cv} is the number of volumetric components, $\hat{C}_\kappa$ is the volume of component κ adsorbed on the rock surface per unit pore volume, and $1-\sum_{\kappa=1}^{n_{cv}} \hat{C}_\kappa$ represents the reduction in pore volume due to adsorption.

Physical dispersion is modeled in a precise manner, using the full dispersion tensor. In a Cartesian coordinate system it is given by:

$$\vec{\vec{K}}_{\kappa\ell} = \begin{bmatrix} K_{xx\kappa\ell} & K_{xy\kappa\ell} & K_{xz\kappa\ell} \\ K_{yx\kappa\ell} & K_{yy\kappa\ell} & K_{yz\kappa\ell} \\ K_{zx\kappa\ell} & K_{zy\kappa\ell} & K_{zz\kappa\ell} \end{bmatrix} . \tag{4}$$

The elements of the dispersion tensor for multiphase, multicomponent flow in permeable media including molecular diffusion are:

$$K_{xx\kappa\ell} = \frac{D_{\kappa\ell}}{\tau} + \frac{\alpha_{L\ell} u_{x\ell}^2 + \alpha_{T\ell} (u_{y\ell}^2 + u_{z\ell}^2)}{\phi S_\ell \, |u_\ell|} \tag{5a}$$

$$K_{yy\kappa\ell} = \frac{D_{\kappa\ell}}{\tau} + \frac{\alpha_{L\ell} u_{y\ell}^2 + \alpha_{T\ell} (u_{z\ell}^2 + u_{x\ell}^2)}{\phi S_\ell \, |u_\ell|} \tag{5b}$$

$$K_{zz\kappa\ell} = \frac{D_{\kappa\ell}}{\tau} + \frac{\alpha_{L\ell} u_{z\ell}^2 + \alpha_{T\ell} (u_{x\ell}^2 + u_{y\ell}^2)}{\phi S_\ell \, |u_\ell|} \tag{5c}$$

$$K_{xy\kappa\ell} = K_{yx\kappa\ell} = \frac{u_{x\ell} u_{y\ell} (\alpha_{L\ell} - \alpha_{T\ell})}{\phi S_\ell \, |u_\ell|} \tag{5d}$$

$$K_{yz\kappa\ell} = K_{zy\kappa\ell} = \frac{u_{y\ell} u_{z\ell} (\alpha_{L\ell} - \alpha_{T\ell})}{\phi S_\ell \, |u_\ell|} \tag{5e}$$

$$K_{zx\kappa\ell} = K_{xz\kappa\ell} = \frac{u_{z\ell} u_{x\ell} (\alpha_{L\ell} - \alpha_{T\ell})}{\phi S_\ell \, |u_\ell|} \, , \tag{5f}$$

where

$$|u_\ell| = (u_{x\ell}^2+u_{y\ell}^2+u_{z\ell}^2)^{1/2} \ . \qquad (6)$$

The fluxes $u_{x\ell}$, $u_{y\ell}$, and $u_{z\ell}$, are modeled through the use of Darcy's law for multiphase flow through permeable media:

$$\vec{u}_\ell = -\vec{\vec{k}}\,\lambda_{r\ell}\cdot(\vec{\nabla}P_\ell-\gamma_\ell\vec{\nabla}D) \ , \qquad (7)$$

where $\vec{\vec{k}}$ is a diagonal permeability tensor.

The source terms q_κ are a combination of volumetric injection/production rate ($q_{\kappa f}$) per bulk volume and volumetric reaction rate ($q_{\kappa r}$) per pore volume for component κ and may be expressed as

$$q_\kappa = q_{\kappa f}+q_{\kappa r} \qquad (8a)$$

with

$$q_{\kappa r} = \phi_R[1+(C_f+C_\kappa^0)\,\Delta P_R]\,(\sum_{\ell=1}^{n_p} S_\ell r_{\kappa\ell}+r_{\kappa S}) \ , \qquad (8b)$$

where $r_{\kappa\ell}$ and $r_{\kappa S}$ are the reaction rates in liquid and solid phases, respectively.

For tracer components, the total phase saturation includes the flowing (S_ℓ^f) and dendritic (S_ℓ^d) portions:

$$S_\ell = S_\ell^f + S_\ell^d \ . \qquad (9a)$$

The mass transfer between the two portions is given by a Coats-Smith type capacitance model (Coats and Smith, 1964; Smith *et al.*, 1988):

$$\frac{\partial}{\partial t}(S_\ell^d C_{\kappa\ell}^d) = M_{\kappa\ell}\,(C_{\kappa\ell}^f-C_{\kappa\ell}^d) \ , \qquad (9b)$$

where $M_{\kappa\ell}$ is a constant mass transfer coefficient. The flowing fraction, defined as:

$$F_\ell = S_\ell^f/S_\ell \qquad (9c)$$

is considered a linear function of the fractional flow function f_ℓ (Smith *et al.*, 1988)

$$F_\ell = F_{\ell 0}+(F_{\ell 1}-F_{\ell 0})f_\ell \ , \qquad (9d)$$

where $F_{\ell 0}$ and $F_{\ell 1}$ are the flowing fractions corresponding to the fractional flow function at zero and one.

Substituting Darcy's law for the volumetric flux $\vec{u}_\ell$, we can also write the general conservation equations in the form

$$\phi_R \frac{\partial}{\partial t} \{\tilde{C}_\kappa [1+(C_f+C_\kappa^0)\, \Delta P_R]\}$$

$$- \vec{\nabla}\cdot(1+C_\kappa^0 \Delta P_R) \sum_{\ell=1}^{n_p} [C_{\kappa\ell} \overset{\rightrightarrows}{k}\, \lambda_{r\ell} \bullet (\vec{\nabla} P_\ell - \gamma_\ell \vec{\nabla} D) + \phi S_\ell\, \overset{\rightrightarrows}{K}_{\kappa\ell} \cdot \vec{\nabla} C_{\kappa\ell}] = q_\kappa$$

$$\kappa = 1, \ldots, n_c . \qquad (10)$$

Pressure equation

The overall material balance equation is the summation of all volumetric component conservation equations:

$$\phi_R C_t \frac{\partial P_R}{\partial t} + \vec{\nabla} \cdot \sum_{\ell=1}^{n_p} \vec{u}_\ell\, (1+\Delta P_R \sum_{\kappa=1}^{n_{cv}} C_\kappa^0 C_{\kappa\ell}) = \sum_{\kappa=1}^{n_{cv}} q_\kappa , \qquad (11)$$

where C_t is the total compressibility defined as

$$C_t = C_f + \sum_{\kappa=1}^{n_{cv}} C_\kappa^0 \tilde{C}_\kappa . \qquad (12)$$

By substituting Darcy's law for the volumetric flux $\vec{u}_\ell$ and using the capillary pressure relations:

$$P_\ell = P_R + P_{c\ell R} \qquad \ell = 1, \ldots, n_p \qquad (13)$$

the pressure equation is obtained in terms of the reference phase pressure P_R:

$$\phi_R C_t \frac{\partial P_R}{\partial t} - \vec{\nabla}\, \overset{\rightrightarrows}{k} \sum_{\ell=1}^{n_p} \lambda_{r\ell} \left(1 + \Delta P_R \sum_{\kappa=1}^{n_{cv}} C_\kappa^0 C_{\kappa\ell} \right) \vec{\nabla} P_R$$

$$- \vec{\nabla}\, \overset{\rightrightarrows}{k} \sum_{\ell=1}^{n_p} \left[\lambda_{r\ell} \left(1 + \Delta P_R \sum_{\kappa=1}^{n_{cv}} C_\kappa^0 C_{\kappa\ell} \right) \left(\vec{\nabla} P_{c\ell R} - \gamma_\ell \vec{\nabla} D \right) \right] = \sum_{\kappa=1}^{n_{cv}} q_\kappa \quad . \qquad (14)$$

Energy balance equation

The energy balance equation is derived by assuming that the only sources of energy are work against pressure, gravity forces, and heat loss to the overburden and underburden rocks (Delshad *et al.*, 1994). Heat loss to the overburden and underburden rocks is computed using the Vinsome and Westerveld (1980) heat loss method:

$$\frac{\partial}{\partial t}[(1-\phi)\rho_s C_{vs} + \phi \sum_{\ell=1}^{n_p} \rho_\ell C_{v\ell} S_\ell] T + \vec{\nabla} \cdot \sum_{\ell=1}^{n_p} (\rho_\ell C_{p\ell} \vec{u}_\ell T - \lambda_T \nabla T) = q_H \, , \qquad (15)$$

where ρ_s and ρ_ℓ are the densities of the rock and phase ℓ, T is the reservoir temperature, C_{vs} and $C_{v\ell}$ are the constant volume heat capacities of the rock and phase ℓ, $C_{p\ell}$ is the constant pressure heat capacity of phase ℓ, λ_T is the constant thermal conductivity, and q_H is the enthalpy source term per bulk volume.

The description and the derivation of the conservation equations and the pressure equation are given in detail in references (Saad, 1989; Delshad *et al.*, 1994, Liu *et al.*, 1993).

Initial and boundary conditions

The initial values of the concentration of each component are specified at each point in the reservoir. For compressible flow cases, the initial pressure distributions are also required. The pressure equation is parabolic in nature, and requires either the pressure or its normal derivative to be specified at each point on the boundary. The conservation equations have a hyperbolic element associated with the convective terms that requires that the composition of any fluid entering through the boundary be specified, but requires no boundary condition on outflow boundaries, nor on any boundary through which no flow is allowed. Physical dispersion introduces a parabolic element to these equations and when present requires composition or its normal derivative to be specified on all boundaries through which dispersive flux is possible.

The basic boundary condition assumed in the model is no flow and no dispersive flux through all impermeable boundaries:

$$\vec{n} \cdot \vec{u}_\ell = 0 \qquad (16)$$

and

$$\vec{n} \cdot \vec{\vec{K}}_{\kappa\ell} \cdot \vec{\nabla} C_{\kappa\ell} = 0 \, . \qquad (17)$$

where $\vec{n}$ is the unit vector normal to the boundary. For the inflow boundary, the normal component of the phase species flux must be known as a function of time. For flow in thermodynamic equilibrium, this condition can be imposed by specifying the total injection rate for each component or alternatively the overall composition and one pressure. For the outflow boundary, we require continuity of fluxes across the reservoir wellbore interfaces and no physical dispersion within the wellbore. The total flow rate or one pressure is specified.

Constitutive relations

The basic governing equations are complemented by a number of constitutive relations that relate the number of phases present and their compositions, saturations, densities, viscosities, interfacial tensions, and capillary pressures to the overall component concentrations and pressure (Lake *et al.*, 1984). Further constitutive relations determine adsorption, residual saturation, and relative permeability.

A brief list of these relations is given here and the quantities appearing in brackets are the number of independent equations corresponding to each relation.

(1) Saturation constraint [1]

$$\sum_{\ell=1}^{n_p} S_\ell = 1$$

(2) Phase concentration constraint [n_p]

$$\sum_{\kappa=1}^{ncv} C_{\kappa\ell} = 1$$

(3) Total concentration definition [n_c]

$$C_\kappa = \sum_{\ell=1}^{n_p} C_{\kappa\ell} S_\ell$$

(4) The adsorption isotherms [n_c]

$$\hat{C}_\kappa = \hat{C}_\kappa (\vec{C})$$

$\vec{C}$ is a vector with C_κ as its elements.

(5) Phase equilibrium relations [$n_c(n_c-1)$]

$$f(\overset{\rightrightarrows}{C}, \vec{C}) = 0$$

$\overset{\rightrightarrows}{C}$ is a matrix with $C_{\kappa\ell}$ as its elements.

(6) Phase viscosities [n_p]

$$\mu_\ell = \mu_\ell (\overset{\rightrightarrows}{C}, \vec{u}_\ell)$$

(7) Phase densities [n_p]

$$\rho_\ell = \rho_\ell (\overset{\rightrightarrows}{C}, P_\ell)$$

(8) Relative permeabilities [n_p]

$$k_{r\ell} = k_{r\ell} (\vec{S})$$

$\vec{S}$ is a vector with S_ℓ as its elements.

(9) Capillary pressure relations [n_p-1]

$$P_{c\ell'\ell} = P_{\ell'} - P_\ell .$$

The conservation equations, the pressure equation, and the constitutive relations are the basic equations describing the isothermal, multicomponent, multiphase flow in permeable media. They result in $2n_c + (5+n_c)n_p$ independent scalar equations equal to the number of dependent variables listed below:

(1)	Total concentration of component κ, C_k	$[n_c]$
(2)	Concentration of component κ adsorbed on the stationary phase, $\hat{C}_\kappa$	$[n_c]$
(3)	Concentration of component κ in phase ℓ, $C_{k\ell}$	$[n_p \text{-} n_c]$
(4)	Phase saturation, S_ℓ	$[n_p]$
(5)	Relative permeabilities, $k_{r\ell}$	$[n_p]$
(6)	Phase viscosities, μ_ℓ	$[n_p]$
(7)	Phase densities, ρ_ℓ	$[n_p]$
(9)	Phase pressures, P_ℓ	$[n_p]$

Fully Implicit Formulation

Our numerical model for the fully implicit simulator is built on the mathematical model. The simulated spatial domain is a rectangular prism and the Cartesian coordinate system used by the simulator is referred to as (x, y, z). The finite-difference grid is block-centered and numbered from 1 to $N_x N_y N_z$, where N_x, N_y, and N_z correspond to the number of gridblocks in each direction. The volume of the mth block (i, j, k) is $\Delta V_m = \Delta x_m \Delta y_m \Delta z_m$. The delta operator δ denotes discrete differences:

$$\begin{aligned} &\delta_t f^n = f^{n+1} - f^n \\ &\delta_x f_m = f_m - f_{m-1}, \delta_x f_i = f_i - f_{i-1} \\ &\delta_y f_m = f_m - f_{m-Nx}, \delta_y f_j = f_j - f_{j-1} \\ &\delta_z f_m = f_m - f_{m-NxNy}, \delta_z f_k = f_k - f_{k-1}. \end{aligned} \tag{18}$$

Most variables, including pressure, concentrations, adsorbed concentrations, saturations, capillary pressures, phase properties such as density, viscosity, interfacial tension, and relative permeabilities are calculated and stored at gridblock centers. Some auxiliary variables, such as transmissibilities and phase velocities, are evaluated at the faces between gridblocks. We illustrate the system of finite difference equations by applying the finite-difference approximations to the species conservation equations (Eq. 10) and the pressure equation (Eq. 14) for a two-dimensional problem.

The component conservation equation for component κ at gridpoint m is

$$(F_{a\kappa})_m^{n+1} + \delta_t t^n (F_{t\kappa} + F_{q\kappa})_m^{n+1}/2 = (F_{a\kappa})_m^n - \delta_t t^n (F_{t\kappa} + F_{q\kappa})_m^n/2 \ . \tag{19}$$

The species accumulation term, $F_{a\kappa}$, is

$$(F_{a\kappa})_m = \{\phi_R \, \Delta V[(1-\sum_{\kappa=1}^{n_{cv}} \hat{C}_\kappa) \sum_{\ell=1}^{n_p} S_\ell C_{\kappa\ell}+\hat{C}_\kappa] \, [1+(C_f+C_\kappa^0)(P_R-P_{R0})]\}_m \tag{20}$$

and the transport term, $F_{t\kappa}$, is

$$\begin{aligned}(F_{t\kappa})_m = & -\delta_x \, [1+C_\kappa^0(P_R-P_{R0})]_m \sum_{\ell=1}^{n_p} \{(C_{x\kappa\ell})_m(\overline{T}_{x\ell})_m \\ & \quad \cdot[\delta_x(P_R+P_{c\ell R})_{m+1}-(\bar{\gamma}_{x\ell})_m\delta_x(D)_{m+1}] \\ & \quad + (\overline{K}_{xx\kappa\ell})_m\delta_x(C_{\kappa\ell})_{m+1}+ (\overline{K}_{xy\kappa\ell})_m\delta_y[(C_{\kappa\ell})_m+(C_{\kappa\ell})_{m+Nx}]\} \\ & -\delta_y[1+C_\kappa^0(P_R-P_{R0})]_m \sum_{\ell=1}^{n_p} \{(C_{y\kappa\ell})_m(\overline{T}_{y\ell})_m \\ & \quad \cdot[\delta_y(P_R+P_{c\ell R})_{m+Nx} -(\bar{\gamma}_{y\ell})_m\delta_y(D)_{m+Nx}] \\ & \quad + (\overline{K}_{yy\kappa\ell})_m\delta_y(C_{\kappa\ell})_{m+Nx}+ (\overline{K}_{yx\kappa\ell})_m\delta_x[(C_{\kappa\ell})_m+(C_{\kappa\ell})_{m+1}]\} \ , \end{aligned} \tag{21}$$

where concentrations $C_{x\kappa\ell}$, $C_{y\kappa\ell}$, and convection coefficients, $\overline{T}_{x\ell}$, and $\overline{T}_{y\ell}$, are computed by

$$\begin{aligned}(C_{x\kappa\ell})_m &= (C_{\kappa\ell})_m+\varphi_m\{r_{xm}[(C_{\kappa\ell})_m]\}\delta_x(C_{\kappa\ell})_{m+1} \\ (C_{y\kappa\ell})_m &= (C_{\kappa\ell})_m+\varphi_m\{r_{ym}[(C_{\kappa\ell})_m]\}\delta_y(C_{\kappa\ell})_{m+Nx}\end{aligned} \tag{22}$$

$$\begin{aligned}(\overline{T}_{x\ell})_m &= (T_{x\ell})_m+\varphi_m\{r_{xm}[(T_{x\ell})_m]\}\delta_x(T_{x\ell})_{m+1} \\ (\overline{T}_{y\ell})_m &= (T_{y\ell})_m+\varphi_m\{r_{ym}[(T_{y\ell})_m]\}\delta_y(T_{y\ell})_{m+Nx}\end{aligned} \tag{23}$$

with $(T_x)_m$ and $(T_y)_m$, given by

$$\begin{aligned}(T_x)_m &= 2(\Delta y\Delta z)_m/(\Delta x_m/k_m+\Delta x_{m+1}/k_{m+1}) \\ (T_y)_m &= 2(\Delta x\Delta z)_m/(\Delta y_m/k_m+\Delta y_{m+Nx}/k_{m+Nx})\end{aligned} \tag{24}$$

are transmissibilities.

φ_m is the flux function and constrained by

$$0 \leq \varphi_m \leq \varphi_{bm} = \min(1, r_m) \qquad (25)$$

with

$$r_{xm}[(C_{\kappa\ell})_m] = \delta_x(C_{\kappa\ell})_m/\delta_x(C_{\kappa\ell})_{m+1}$$

$$r_{ym}[(C_{\kappa\ell})_m] = \delta_y(C_{\kappa\ell})_m/\delta_y(C_{\kappa\ell})_{m+Nx}$$

$$r_{xm}[(k_{r\ell})_m] = \delta_x(k_{r\ell})_m/\delta_x(k_{r\ell})_{m+1}$$

$$r_{ym}[(k_{r\ell})_m] = \delta_y(k_{r\ell})_m/\delta_y(k_{r\ell})_{m+Nx} \quad . \qquad (26)$$

With the fully implicit formulation, all variables and TVD limiter functions are evaluated using the values of the new timestep. Besides the flux limiter function φ_m, we also need to evaluate the derivatives of the flux-limiter functions with respect to the related neighboring gridpoint variables. Results are given in Table 1. The flux-limiter functions and their derivatives corresponding to the different schemes are shown in Figs. 1 and 2.

The dispersion coefficients $\overline{K}_{xx\kappa\ell}$, $\overline{K}_{yy\kappa\ell}$, $\overline{K}_{xy\kappa\ell}$, and $\overline{K}_{yx\kappa\ell}$ measure the physical dispersion:

$$(\overline{K}_{xx\kappa\ell})_m = \Delta y_m \Delta z_m/[(\Delta x_m+\Delta x_{m+1})/2]\ (\phi_R S_\ell K_{xx\kappa\ell})_m$$

$$(\overline{K}_{xy\kappa\ell})_m = \Delta y_m \Delta z_m/[\Delta y_m+(\Delta y_{m-Nx}+\Delta y_{m+Nx})/2]\ (\phi_R S_\ell K_{xy\kappa\ell})_m$$

$$(\overline{K}_{yy\kappa\ell})_m = \Delta x_m \Delta z_m/[(\Delta y_m+\Delta y_{m+Nx})/2]\ (\phi_R S_\ell K_{yy\kappa\ell})_m$$

$$(\overline{K}_{yx\kappa\ell})_m = \Delta x_m \Delta z_m/[\Delta x_m+(\Delta x_{m-1}+\Delta x_{m+1})/2](\phi_R S_\ell K_{yx\kappa\ell})_m \quad . \qquad (27)$$

The average specific weight of phase ℓ is calculated from

$$(\overline{\gamma}_{x\ell})_m = [(\gamma_\ell E_\ell \Delta x)_m+(\gamma_\ell E_\ell \Delta x)_{m+1}]/([(E_\ell \Delta x)_m+(E_\ell \Delta x)_{m+1}]$$

$$(\overline{\gamma}_{y\ell})_m = [(\gamma_\ell E_\ell \Delta y)_m+(\gamma_\ell E_\ell \Delta y)_{m+Nx}]/([(E_\ell \Delta y)_m+(E_\ell \Delta y)_{m+Nx}] \quad , \qquad (28a)$$

where E_ℓ is the existence index of phase ℓ and is defined as

$$(E_\ell)_m = \begin{cases} 0 & (S_\ell)_m = 0 \\ 1 & (S_\ell)_m > 0 \ . \end{cases} \qquad (28b)$$

Phase saturations and phase concentrations in the transport term are the flowing portions of the total phase saturations and phase concentrations if we consider the capacitance properties. The dendritic portions, S^d_ℓ and $C^d_{\kappa\ell}$, are calculated from:

$$(S^d_\ell)_m = [(1-F_\ell)S_\ell]_m = \{[1-F_{\ell 0}-(F_{\ell 1}-F_{\ell 0})f_\ell]S_\ell\}_m \tag{29}$$

and

$$(C^d_{\kappa\ell})_m = (C^d_{\kappa\ell}S^d_\ell)_m/(S^d_\kappa)_m \ , \tag{30}$$

where the product $(C^d_{\kappa\ell}S^d_\ell)_m$ is evaluated using the Coats-Smith type capacitance model (Coats and Smith, 1964; Smith *et al.*, 1988):

$$(C^d_{\kappa\ell}S^d_\ell)^{n+1}_m+\delta_t t^n M_{\kappa\ell}(C^f_{\kappa\ell}-C^d_{\kappa\ell})^{n+1}_m/2 = (C^d_{\kappa\ell}S^d_\ell)^n_m-\delta_t t^n M_{\kappa\ell}(C^f_{\kappa\ell}-C^d_{\kappa\ell})^n_m/2 \ . \tag{31}$$

The flowing phase saturations S^f_ℓ are determined from

$$(S^f_\ell)_m = (F_\ell S_\ell)_m \tag{32}$$

and the total flowing concentrations C^f_κ are computed by

$$(C^f_\kappa)_m = \sum_{\ell=1}^{n_p} (C^f_{\kappa\ell}S^f_\ell)_m = (C_\kappa)_m-\sum_{\ell=1}^{n_p} (C^d_{\kappa\ell}S^d_\ell)_m . \tag{33}$$

The flowing phase concentrations $C^f_{\kappa\ell}$ then can be obtained using the partitioning method.

The source and sink term, $F_{q\kappa}$, is expressed as

$$\begin{aligned}(F_{q\kappa})_m = \{ &\sum_{\ell=1}^{n_p} [Q_\ell+(PI)_\ell(P_{wf}-P_R-P_{c\ell R})]\, C_{\kappa\ell} \\ &+\phi_R\Delta V[1+(C_f+C^0_\kappa)(P_R-P_{R0})](\sum_{\ell=1}^{n_p} S_\ell r_{\kappa\ell}+r_{\kappa S})\}_m \ .\end{aligned} \tag{34}$$

The pressure equation at gridpoint m is

$$(F_a)^{n+1}_m+\delta_t t^n(F_t+F_q)^{n+1}_m/2 = (F_a)^n_m-\delta_t t^n(F_t+F_q)^n_m/2 \ , \tag{35}$$

where the total accumulation F_a is

$$(F_a)_m = (\phi_R \Delta V)_m \{ C_f + \sum_{\kappa=1}^{n_{cv}} C_\kappa^0 [(1 - \sum_{\kappa=1}^{n_{cv}} \hat{C}_\kappa) \sum_{\ell=1}^{n_p} S_\ell C_{\kappa\ell} + \hat{C}_\kappa] \}_m (P_R)_m \, , \tag{36}$$

the total transport F_t is

$$\begin{aligned}(F_t)_m = & -\delta_x \{ \sum_{\ell=1}^{n_p} (\overline{T}_{x\ell})_m [1 + (P_R - P_{R0}) \sum_{\kappa=1}^{n_{cv}} C_\kappa^0 C_{\kappa\ell}]_m \\ & \cdot [\delta_x (P_R + P_{c\ell R})_{m+1} - (\overline{\gamma}_{x\ell})_m \delta_x (D)_{m+1}] \} \\ & -\delta_y \{ \sum_{\ell=1}^{n_p} (\overline{T}_{y\ell})_m [1 + (P_R - P_{R0}) \sum_{\kappa=1}^{n_{cv}} C_\kappa^0 C_{\kappa\ell}]_m \\ & \cdot [\delta_y (P_R + P_{c\ell R})_{m+Nx} - (\overline{\gamma}_{y\ell})_m \delta_y (D)_{m+Nx}] \}\end{aligned} \tag{37}$$

and the total source and sink F_q is

$$(F_q)_m = \sum_{\ell=1}^{n_p} [Q_\ell + (PI)_\ell (P_{wf} - P_R - P_{c\ell R})]_m \, . \tag{38}$$

The capillary pressure model allows us to simulate intermediate-wettability cases (Ferreira, 1992). Capillary pressure effects are considered in the well model.

Solution of the Nonlinear System of Equations

At each gridpoint, we have a total of n_c finite-difference residual equations consisting of n_c-1 component conservation equations and one pressure equation. This means that the total number of independent or primary variables is n_c. Besides the reference phase pressure and saturation, we choose some relevant phase concentrations as the other primary variables. The remaining phase saturations, concentrations, pressures, and physical properties are secondary variables and depend on the primary variables. They can be obtained using saturation constraints, phase equilibrium relations, capillary pressure relations, and all other constitutive relations.

The nonlinear system of residual equations can be linearized and solved using a Newton iteration, defined by

$$J \delta P = -f, \tag{39}$$

where J is the Jacobian matrix formed by differentiating the nonlinear system of residual equations $f(P)$ with respect to the primary variables P. The Jacobian matrix and the residual equations are updated at the end of each iteration, and the iteration continues until the relative changes in the primary variables between two successive approximations are small enough to satisfy given tolerance criteria.

For a two-dimensional simulation problem of n_c components using N_xN_y gridblocks, the total number of equations is $n_cN_xN_y$. The Jacobian matrix is constructed such that the primary variable indices are the faster-changing indices in the solution vector. With the high-order scheme, a total of 13 gridpoints may be involved in the finite-difference equations (Fig. 3) and $13n_c$-8 partial differentiation computations are required for each equation to build the Jacobian matrix. The Jacobian matrix may have the same number of nonzero elements in each row and a bandwidth of $2n_c(2N_x+1)-1$. Figure 4 shows the matrix structure for a two-dimensional, two-component problem using the high-order scheme and 5x5 gridblocks.

The solution of the linear system of equations represents the most costly aspect of a fully implicit simulator. Using an efficient solution solver can greatly improve the efficiency of the simulator. Both direct and iterative solvers can be employed to solve the system of equations, although iterative solvers are preferred for multidimensional problems, where the Jacobian matrices have a large bandwidth.

Timestepping Algorithms

The choice of timestep size is dictated by accuracy considerations and stability constraints. Since a fully implicit solution technique is employed, the numerical solution is stable for all timestep sizes. There are, however, other limitations that must be considered. For example, Newton's method is guaranteed to converge only from good starting guesses. For a simulation problem, there may be some times when solution gradients are very large, such as near breakthrough. Simply using the solution of the last timestep as the starting guess for the current timestep may not converge. In addition, some important physical phenomena may be missed by using an arbitrarily large timestep size.

Using the past information of the relative changes in the primary variables to decide the current timestep size is a strategy employed by most timestepping algorithms. The timestep size selection is based on the information from the most recent iterations and user-specified maximum and minimum timestep sizes denoted $(Dt)_{max}$ and $(Dt)_{min}$, such that the current timestep size $d_t t^n$ follows

$$(\Delta t)_{min} \, \Delta \, (\Delta t)^n \, \Delta \, (\Delta t)_{max}. \tag{40}$$

Besides constant timestepping, which often requires a smaller timestep size to guarantee convergence and takes more simulation time, we employ three timestepping algorithms for the simulator.

Algorithm 1 is the one used in The University of Texas fully implicit steamflood simulator (UTTHERM) (Brantferger, 1991). The ratio of the current to the previous timestep size is proportional to the relative changes in the primary variables ε_p:

$$(\Delta t)^n \propto \varepsilon_p^{n-1}(\Delta t)^{n-1}. \tag{41}$$

ε_p^n is expressed as

$$\varepsilon_p^n = \min_{N_b} \left| P^n/(P^n - P^{n-1}) \right|. \tag{42}$$

where N_b is the total number of gridblocks.

Algorithm 2 uses the ratio of relative changes in the primary variables between the last two timesteps to decide the current timestep size:

$$(\Delta t)^n \propto (\varepsilon_p^{n-2}/\varepsilon_p^{n-1})(\Delta t)^{n-1}. \tag{43}$$

Algorithm 3 simply chooses the current timestep size by comparing the number of iterations N_i required by the last two steps:

$$(\Delta t)^n \propto (N_i^{n-1}/N_i^{n-2})(\Delta t)^{n-1}. \tag{44}$$

More sophisticated timestepping algorithms have been proposed where the timestep size selection is based on truncation error analysis (Mehra *et al.*, 1983; Rubin and Buchanan, 1985). A sensitivity vector is computed and used to obtain an optimal timestep sequence for a specified global truncation error. Considerably extra storage and computational effort are needed to get the required vector for the algorithm, which may overshadow the algorithm, especially when simulating difficult problems.

The timestep size chosen by any of the timestepping selection algorithms is not guaranteed to produce convergence results. A recovery feature is included in the simulator to continue the simulation in case an iteration fails. It stores the necessary information of the last timestep, automatically reduces the current timestep size, and restarts the iteration until a successful iteration is completed with a suitable timestep size.

Simulation Results and Analyses

Simulator verification

To establish the validity of the formulation of the conservation equations, the results of a one-dimensional miscible flow are compared with the analytical solution of the convection-diffusion equation. Figure 5 shows a comparison of the analytical solution and the numerical solution at 0.5 PV injected for a Peclet number (the ratio of convective to dispersive transport) of 1000. One hundred gridblocks with Courant numbers (measure of dimensionless timestep size) of 0.5, 1.0, and 1.5 are used. The agreement between the analytical solution and the simulation results is remarkable even at the higher Courant numbers. Similar agreement is also shown in Fig. 6 for the same problem but at a lower Peclet number of 100. Note that with the IMPES formulation, smaller timestep sizes are required for processes dominated by physical dispersion. This requirement does not exist with the fully implicit formulation.

One hundred gridblocks and a Courant number of 0.5 are used to simulate an example one-dimensional waterflood problem with zero capillary pressure and a mobility ratio of 3. Figure 7 shows the simulation results along with the analytical solution at 0.2 PV injected. The simulated solution matches the analytical solution very well except for small numerical smearing at the displacement fronts.

The boundary conditions on the outflow boundary coupled with the requirement that the phase pressure be continuous across the boundary results in a phenomenon called the "capillary end effect" (Richardson *et al.*, 1952; Amyx *et al.*, 1960). An analytical solution of the saturation profile along a one-dimensional, homogeneous porous medium is given by Richardson *et al.* (1952). A one-dimensional simulation example simulated by Chang (1990) is used to check the implementation of the outflow boundary condition in the simulator. The problem has a Rapoport and Leas number (the ratio of viscous to capillary force) of 2.78 and a residual oil saturation of 0.35. Figure 8 shows the good agreement between the analytical solution and the simulation results. One hundred gridblocks and a Courant number of 1 are used.

The capillary pressure model in our simulator allows us to simulate intermediate-wettability cases (Ferreira, 1992). A water saturation S* is defined where the capillary pressure is zero. The capillary end effect of the intermediate-wettability case with S*=0.5 and Rapoport and Leas number of one was tested. Figure 9 shows the water saturation profiles at times of 1, 5, 10, and 50 PV injected. As time increases, the profiles approach the analytical solution, which is derived under the assumption of infinite flooding time or steady-state. One hundred gridblocks and a Courant number of 1 are used.

Figure 10 shows the results of Holing's one-dimensional polymerflood problem at 0.5 pore volumes injected (Holing *et al.*, 1990). One hundred gridblocks and a Courant number of 0.5 are used. The porous medium was initially filled with 70% oleic-phase fluid and 30% aqueous-phase fluid with 0.9 wt% polymer, then injected with 100% aqueous-phase fluid with 0.1 wt% polymer. The analytical solutions of the saturation and polymer concentration profiles were calculated using fractional flow theory (Pope, 1980). Good resolution in both the water saturation and polymer concentration fronts is obtained and the numerical solution matches the analytical solution well.

An analytical solution is available for an ideal tracer flow at unit mobility ratio for a homogeneous five-spot well pattern (Abbaszadeh-Denghani and Brigham, 1984). The simulation domain is one-quarter of the well pattern with a length of 330 ft. A 30x30 grid and a Courant number of 1 were used to simulate the flow of a 2% PV tracer slug with a longitudinal dispersivity of 0.66 ft and a Peclet number of 500 (P_{Δ}=8.33). The effluent tracer concentration is normalized by the product of slug size and the square root of the Peclet number. Figure 11 shows a comparison of the analytical solution with the simulation results. The overall match is very good, and the small discrepancy between the two solutions can be reduced using finer grids and smaller timestep sizes.

Comparison with IMPES formulation

The simulation results of the one-dimensional convection-diffusion, one- and two-dimensional waterflood, and one- and two-dimensional polymerflood problems are compared with those obtained using the IMPES formulation. Figure 12 compares the absolute errors and computation times (VAX 3540) of simulating the one-dimensional convection-diffusion problem (N_{pe}=100) using the two formulations with 100 gridblocks. The fully implicit formulation demonstrates its computational efficiency by producing smaller errors compared to the IMPES formulation for the same CPU time. Figure 13 plots the absolute errors corresponding to different Courant numbers. The IMPES formulation has larger errors for Courant numbers greater than one and becomes unstable as the Courant number approaches one. The errors of the fully implicit formulation are almost identical at small Courant numbers. This can be explained by the second-order accuracy of the Crank-Nicolson time derivative approximations. The errors caused by time derivative approximations are small and the total error is mainly from spatial truncation errors for small Courant numbers.

The higher-order scheme with the IMPES formulation is less stable when simulating both convection-dominated and dissipation-dominated problems. The dissipation is mainly provided by dispersive forces for miscible displacements and by capillary forces for immiscible displacements. The one-dimensional waterflood with a Rapoport and Leas number of 5 is simulated using both formulations with 100 gridblocks and Courant numbers of 0.1 and 0.5. Figure 14 shows the instability of the IMPES formulation when a Courant number of 0.5 is used. Figures 15 and 16 show the simulation results of oil recovery, water-oil ratio, and water cut for the two-dimensional waterflood. The reservoir dimensions, properties, and well pattern and conditions are the same as those for the tracer flow in a five-spot pattern. The reservoir has an initial oil saturation of 0.8 and is then flooded by water. The mobilities of water and oil are characterized by S^2 and $(1-S)^2/2$, where S is the water saturation. A 10x10 grid is used for both formulations. Figure 15 shows the results of the IMPES formulation, which failed at a Courant number of one, while the results of the fully implicit formulation are almost the same at Courant numbers of 0.1 and 3.

The time-lagged and pressure-dependent mobility terms in the pressure equation are another source of instability in the IMPES formulation. For a polymerflood, this instability can arise because of the explicit treatment of both the relative permeability and viscosity terms. Figure 17 shows this instability when simulating Holing's one-dimensional polymerflood problem. The IMPES formulation becomes unstable at a Courant of number of 0.5. The results using the fully implicit formulation with the same Courant number given in Fig. 11 show that they are stable and close to the analytical solution. A simulation of a two-dimensional polymerflood in a five-spot pattern is also conducted to compare the two formulations. All input data are the same as those of the waterflood except that the aqueous phase viscosity becomes $1+10C_{4a}$ where C_{4a} is the polymer concentration in the aqueous phase, and 0.1 wt% polymer is injected instead of pure water. The results of oil recovery, water cut, and effluent polymer concentration are obtained using the TVD third-order scheme with a 10x10 grid. At a Courant number of 0.1, the two formulations give almost same results (Fig. 18). At larger Courant numbers, the results of the fully implicit formulation show nearly no change (Fig. 19) while the IMPES formulation becomes unstable, which is characterized by oscillations and late polymer breakthrough (Fig. 20). To test the effect of heterogeneity, we then simulated the same problem using a heterogeneous permeability field with a Dykstra-Parsons coefficient of 0.8 (Dykstra and Parsons, 1950). The Dykstra-Parsons coefficient is a measure of the variability of permeability values and is defined as

$$V_{DP} = 1 - (k)_{0.841} / (k)_{0.5} \, , \qquad (45)$$

where $(k)_{0.5}$ is the median of the permeability and $(k)_{0.841}$ is one standard deviation below the median. A Dykstra-Parsons coefficient between 0 and 1 represents the degree of heterogeneity. From the results shown in Figs. 21 to 23, we can draw similar conclusions to those of the homogeneous case with regard to the comparison of the two formulations. We also observe that for both formulations smaller Courant numbers are required to simulate the heterogeneous case than to simulate the homogeneous case.

Comparison with lower-order spatial discretization scheme

The lower-order space discretization one- and two-point upstream schemes are available in our fully implicit simulator for comparison purposes. These are the conventional finite-difference schemes employed by most fully implicit simulators. Figure 24 compares the errors simulating the one-dimensional convection-diffusion problem using the one-point upstream scheme with those using the TVD flux-limited third-order scheme at different Courant numbers. The number of gridblocks used for both schemes is 100. The one-point upstream scheme produces larger errors in practical Courant number regions. The differences become smaller at larger Courant numbers where time-truncation errors dominate. Figure 25 shows the results of the one-dimensional polymerflood simulated using the one-point upstream scheme. In contrast to the third-order scheme (Fig. 11), both the water saturation and polymer concentration shocks are spread out, which results in inaccurate prediction of both recoveries and breakthrough times and leads to erroneous conclusions. This can be illustrated by the results of the two-dimensional waterflood (Fig. 26) and polymerflood (Fig. 27). Water cut, water-oil ratio, and effluent polymer concentration curves given by the one-point upstream scheme show early breakthroughs of both water and polymer. The differences between the lower-order scheme and the higher-order scheme can also be observed from the simulation results of the two-dimensional polymerflood of heterogeneous case (Fig. 28). For reference, the comparisons between the lower-order scheme and the higher-order scheme using the IMPES formulation are shown in Figs. 29 and 30.

Effect of TVD flux limiter

We have given numerous examples to show the improvements in simulation results using a TVD flux limiter with the third-order scheme for the IMPES formulation. One example is given here to show the flux limiter effect on the third-order scheme using the fully implicit formulation. Figure 31 shows the water saturation and polymer concentration profiles of Holing's one-dimensional polymerflood problem simulated using the third-order scheme without flux limiting. Comparison with the flux-limited results (Fig. 11) clearly demonstrates the importance of flux limiting to the high-order scheme for the fully implicit formulation.

Improvements in computational efficiency

To study the effects of the linear equation solvers on the efficiency of the simulator, tracer flow in a five-spot pattern is simulated up to 1.3 PV injected using both direct (LU decomposition) and iterative (OMIN algorithms, a truncated and restarted method for nonsymmetric systems) solvers with 30x30 grids and a Courant number of 3. The iterative solver is provided by the NSPCG package (Oppe *et al.*, 1988). Table 2 shows a comparison of the two solvers. The ratio of the total CPU time (CRAY Y-MP) using the iterative solver to that using the direct solver is 0.56 and the total time saving is 42%. The iterative solver is definitely preferred here. Since solving the linear system of equations is the most costly part of total simulation time (95% using the iterative solver and 98% using the direct solver), using the more efficient solver greatly improves the more computational efficiency of the fully implicit simulator.

The timestepping strategy was studied simulating the two-dimensional polymerflood. A 5x5 grid was used for the test. The oil recovery, water cut, and effluent polymer concentration results are shown in Fig. 32. The three timestepping algorithms are compared with same initial Courant number of 1. The maximum and minimum Courant numbers are 3 and 0.01, respectively. Simulation using a constant timestep size using a Courant number of 0.5 is also conducted for the purpose of comparison. The Courant number and the iteration numbers corresponding to different algorithms over the entire simulation period are shown in Figs. 33 and 34. After breakthrough, the curves of algorithm 1 change more dramatically compared to those of the other algorithms. The simulation time (CRAY Y-MP), total number of timesteps, total iterations, and average Courant numbers are listed in Table 3. Algorithm 1 takes more iterations, more timesteps, more computer time, and smaller average Courant number to complete the simulation. The comparison emphasizes the importance of using a suitable timestepping algorithm.

Summary, Conclusions, and Future Work

We have developed a fully implicit algorithm for compositional, chemical flooding simulation and a simulator with all the numerical features. The pressure equation and the component conservation equations are solved simultaneously. The temporal derivative is discretized using a Crank-Nicolson-type scheme. The interface concentration and mobilities are computed using the third-order scheme with TVD flux limiting. The finite-difference approximation has overall second-order temporal accuracy, third-order spatial accuracy for convection problems, and is total variation diminishing. The resulting nonlinear system of residual equations are solved for the primary variables which consist of a reference phase pressure, a reference phase saturation, and relevant phase concentrations. For the fully implicit formulation, besides the flux-limiter functions, we also need to evaluate the derivatives of flux limiter functions with respect to the related neighboring gridpoint solutions. The corresponding evaluation formulas are given in this study. The nonlinear system of residual equations are linearized and solved using Newton iterations. The Jacobian matrix of the Newton iteration and the flux-limiter functions and their derivatives are updated at the end of each iteration.

Test cases are shown to verify both the mathematical formulations and the finite-difference schemes and to ensure the correctness of the program coding. Verification cases with analytical solutions include problems of one-dimensional convection-diffusion, waterflood, polymerflood, capillary end effects, and two-dimensional ideal tracer flow in a five-spot pattern. The results of one-dimensional convection-diffusion, one- and two-dimensional waterflood, and one-dimensional polymerflood problems were used to compare the accuracy and efficiency of different simulation methods. With both using TVD high-order schemes, the fully implicit formulation is compared with the IMPES formulation. Using the fully implicit formulation, the first-order spatial discretization scheme is compared with the high-order spatial discretization scheme, and the high-order scheme is compared with the TVD high-order scheme. The computational efficiencies of different solvers and timestepping algorithms have been studied simulating a two-dimensional polymerflood and ideal tracer flow in a five-spot pattern.

The simulator is verified by the good agreement between the numerical results and analytical solutions. The results demonstrate that the TVD high-order scheme with a fully implicit formulation is more stable than that with an IMPES formulation. Using the fully implicit formulation, the TVD high-order scheme is more accurate than the lower-order spatial discretization scheme and the high-order spatial discretization scheme without TVD flux-limiting. The computationally efficiency of the simulator can be greatly improved by using suitable timestepping algorithms and effective solution solvers to solve the linear systems of equations, which represents the most costly aspect of a fully implicit simulator.

We are now testing our implicit method on two-dimensional problems involving more physical-chemical properties such as heterogeneity, capillarity, dispersion, adsorption, etc. We will continue testing our solution schemes by using different solvers and timestepping algorithms. We will later extend our implicit method to three-dimensional polymer and surfactant flood problems.

OPTIMIZATION OF SURFACTANT FLOODING

Introduction

The main objective of Task 2 is to develop the knowledge and capability of how to use simulation effectively to lower the risk and cost of surfactant flooding. The reduction of the risk and cost of surfactant flooding are closely related tasks, since any reduction in risk will directly improve the economics of a commercial field application. Affordable reservoir simulation realistically taking into account reservoir characteristics is the only method that the reservoir engineer has to optimize the design of surfactant floods. The importance of good reservoir characterization and the large impact of reservoir characteristics on surfactant flooding as well as other tertiary oil recovery processes have been well-established during the past twenty years. Improved means to assess the risk and performance of surfactant flooding taking into account realistic reservoir characteristics are clearly needed. The most important of these reservoir characteristics is heterogeneity.

In the past, we and others have used the traditional layered-reservoir description in our simulations of surfactant flooding. Although the theoretical basis for using more flexible and realistic reservoir descriptions based upon geostatistical methods has been available now for several years, and we and many others have applied these methods to the simulation of other processes such as waterflooding, their application to surfactant flooding has not been attempted to date. This is unfortunate since surfactant flooding is generally more sensitive to reservoir characteristics than simpler processes and the need for cost and risk reduction much greater. Clearly, the use of stochastic simulations lends itself to the quantitative assessment of uncertainty, since multiple realizations of the same statistical description can be made and some idea of the probability distribution of outcomes computed. In addition, the stochastic approach can be used to better understand the impact of reservoir characteristics and then to improve the design of the surfactant flood so that it will be more robust and efficient and our predictions more accurate.

We illustrate a few of our simulation results in this report based upon our initial efforts to accomplish this goal, which is part of task 2 of our research project. Using geostatistics, we perform a systematic evaluation of the impact of heterogeneity on surfactant flooding. Permeability fields as a function of the variance and correlation lengths are generated using geostatistical methods. When well data and other deterministic information about the reservoir are superimposed on these descriptions, the process is known as conditional simulation. Conditional simulations have been used in waterflooding and miscible flooding but not in surfactant flooding.

To study the effect of stochastic modeling on surfactant flooding, several multiple realization studies were conducted. To generate different realizations only the random number seed is changed, keeping other statistical parameters the same. To quantify the uncertainty, various geostatistical parameters such as correlation length, reservoir heterogeneity (Dykstra-Parsons coefficient), and vertical-to-horizontal permeability ratio were chosen. All of the above parameters have been studied with multiple realizations of the same permeability field.

Surfactant floods should benefit from the improved injectivity brought about by horizontal wellbores. Simulation could help us in determining the benefits and drawbacks of horizontal wellbores when used in surfactant floods. In this report, simulation is used to study the effect of a horizontal injection wellbore on the injectivity and sweep efficiency of surfactant floods under a variety of reservoir conditions. These conditions are different well spacings, different wellbore lengths, different vertical-to-horizontal permeability ratios, and different permeability field realizations.

Base Case Simulation

All simulation runs were carried out using UTCHEM, a three-dimensional chemical flooding simulator developed at The University of Texas at Austin. A quarter-symmetry element of a 40-acre five-spot pattern is considered. The simulated quarter five-spot is 660 ft in the x direction, 660 ft in the y direction, and 140 ft in the z direction. The simulation grid, as shown in Fig. 35, is 11x11x5, so the gridblocks are 60 feet each in the x and y directions and 28 feet in the z direction. The porosity is uniform and equal to 0.136. The permeability field was generated stochastically. The Dykstra-Parsons coefficient (V_{DP}) is 0.8 and the geometric mean permeability is 50 md. This description is an idealization of an actual mid-Continent U.S. sandstone oil reservoir that is a potential candidate for surfactant flooding since it has already been waterflooded to near its economic limit and is otherwise subject to abandonment. The stochastic reservoir description was generated using a University of Texas program based upon the matrix decomposition method (Yang, 1990). A spherical variogram and a log normal permeability distribution were used. The permeability distribution for correlation lengths of 660 feet in the x and y directions and 28 feet in the z direction, $V_{DP} = 0.8$ (the standard deviation of the logarithm of the permeability is 1.609), and Realization No. 1 are shown in Fig. 36.. Permeability values range between 0.17 and 2,550 md.

Physical properties used in all the simulations described here are shown in Figs. 37 through 46. Figures 37 and 38 show the oil and water relative permeability curves used at low and high capillary numbers, respectively. Figure 39 shows the relative permeability for microemulsion and oil at high capillary number. Polymer properties are typical of a xanthan gum solution. Figure 40 shows the polymer adsorption modeled by a Langmuir-type isotherm as a function of polymer concentration. Polymer viscosity as a function of polymer concentration and shear rate is shown in Fig. 41. Figure 42 shows the plot of permeability reduction factor against polymer concentration. Figure 43 shows the capillary desaturation curves for oil, water, and microemulsion phases, which indicate the mobilization of these phases as a function of a dimensionless capillary number. Interfacial tensions for oil and microemulsion and water and microemulsion are shown as a function of solubilization ratios in Fig. 44. Figure 45 shows the surfactant adsorption as a function of surfactant concentration. The ternary diagram for the Type III phase environment of the oil, water, and surfactant mixture at a salinity of 0.611 meq/ml (35,700 mg/l) is plotted in Fig. 46. Although the surfactant and polymer properties are extremely important and have been carefully selected to be close to optimal for these conditions, but still realistic based upon the best of recent chemical research developments, we do not go into this aspect of the process simulation since we want to focus on the stochastic simulation aspect in this report. The simulated chemical properties will be varied in future reports. A detailed description of the physical property modeling in UTCHEM is given by Saad (1989).

To mimic conditions before the start of tertiary oil recovery, the reservoir was first waterflooded with a low initial water saturation of 0.2, and the simulation ended when a water cut of 98% was reached. In the future, we plan to study the effect of variable residual saturations and initial saturations in the reservoir, which is more realistic as the permeability is stochastically distributed. The resulting pressure and saturation distributions were then used as the initial distributions for the surfactant flood simulations. The average oil saturation was 30.97% at the end of the waterflood for this base case. After waterflooding, 0.25 pore volumes of 2.5 vol.% of surfactant was injected. The surfactant slug contained 1,000 ppm polymer and was followed by another 0.5 pore volumes of polymer at the same concentration and finally by water for another 3.25 pore volumes. The wells were vertical and pressure-constrained, and a total of 1,000 psia pressure drop between the injector and the producer was used. The input parameters and the injection scheme for the base case are given in Tables 4 and 5.

The results of the surfactant flood are shown in Figs. 47 through 54. Cumulative oil recovery as a fraction of oil in place at the time of chemical flooding is shown versus pore volumes injected in Fig. 47 and versus time in Fig. 48. The fraction of oil recovered is about 0.6 at 4 pore volumes and it takes about 33 years to reach this value. The results are shown as a function of both time and pore volumes, since the wells are pressure-constrained and therefore the injection rate varies with time. The pore volumes injected as a function of time is shown in Fig. 49, which indicates the increased injectivity during the postflush (pore volumes > 0.75). The plot of oil production rate (Fig. 50) shows that the surfactant/polymer slug and polymer drive have effectively displaced the oil bank with an oil rate peak of 200 B/D. The history of total injection rate (Fig. 51) indicates a low injectivity of about 650 B/D during the injection of surfactant/polymer slug and polymer drive, and the injectivity increases to about 4,700 B/D for the injection of low-viscosity water during the chase waterflood. Total surfactant and polymer concentrations at the producer are plotted in Figs. 52 and 53, respectively. Figure 54 shows the effective salinity.

Correlation Length

To investigate the effect of correlation length on surfactant flooding, the - and y-direction correlation lengths were varied simultaneously keeping other statistical parameters the same as those of the base case. The spatial correlation length is the distance over which neighboring permeability values are related to one another. The correlation length can be determined from the variogram, which is the variance of the differences between the permeabilities at two locations separated by a distance h (Kerbs, 1986). The value of h at which the variogram levels off is the correlation length. Correlation length of zero indicates a fully random distribution where the permeability at a given location is independent of its neighbors. With increasing correlation length, the range of influence of one permeability on its neighbors increases up to a distance equal to the correlation length. As the correlation length approaches infinity, the permeability field becomes layered.

Correlation lengths were 330 ft, 660 ft (base case), 1,320 ft and 2,640 ft in the x and y directions. Figures 55 and 56 show the permeability distribution for realization 1 and correlation lengths of 330 feet and 2,640 feet. We also compared a surfactant flood in a reservoir described with uniform permeability layers. This layered reservoir had the same average permeability and standard deviation of permeability to those of the stochastic reservoir. The five vertical gridblocks for the layered description had permeabilities from top to bottom of 275 md, 4.5 md, 197 md, 12.8 md, and 104 md and a uniform porosity of 0.136.

Simulations were conducted as described above for the base case with only the permeability field varied. Figure 57 shows the effect of correlation length on cumulative oil recovery as a fraction of oil in place after the waterflood for the layered description and for the four stochastic cases. We have elected to represent these results as a function of time rather than pore volumes to emphasize the impact of correlation length on injectivity. Both the injector and producer are pressure-constrained wells, so the injection rate varies with time (Fig. 58) as a sensitive function of the reservoir description, and this has a major impact on the project life and thus the economics of the project. As the ratio of the correlation length in the x and y directions to the length in the z direction increases, the reservoir looks more and more like a layered reservoir, and this is clearly reflected in the oil recovery curves of Fig. 57. This shows that there is indeed an incentive to consider reservoir descriptions other than the layered description traditionally used to simulate surfactant flooding. As correlation length increases, the recovery is accelerated but the ultimate recovery decreases. These results can be explained by examining the permeability distribution for each case. This is because, with increase in correlation length, there is channeling in the reservoir through high-permeability layers, and this causes oil to be bypassed in low-permeability layers, resulting in lower oil recovery (Fig. 56). In lower correlation length reservoirs, injectivity is lowered as there are no channels of high permeability (Fig. 55). Low permeability causes more uniform distribution of the injected fluids, and hence higher oil recovery, but at a lower rate.

Reservoir Heterogeneity

To study the effect of reservoir heterogeneity, permeability fields were generated for Dykstra-Parsons coefficients (V_{DP}) of 0.6, 0.8 (base case), 0.85, and 0.9. We selected these values of V_{DP} because they are representative of oil reservoirs that are potential targets of surfactant flooding in the U.S. The simulations were carried out as the base case using these permeability distributions in both waterflood and surfactant/polymer floods. Figures 59 and 60 show the permeability distributions for V_{DP} of 0.6 and 0.9 and realization 1. These figures show the contrast in heterogeneity for the two extreme cases.

Figure 61 shows the effect of reservoir heterogeneity on the cumulative oil recovery. This figure shows that the increase in reservoir heterogeneity accelerates the oil recovery but the ultimate oil recovery is less. Higher V_{DP} means higher variance in permeability. Hence the difference of permeability in neighboring blocks will be greater than for the case of lower V_{DP}. Because of this permeability distribution, oil in low-permeability zones is bypassed, which results in lower cumulative recovery. Lower V_{DP} has higher cumulative recovery because of better sweep efficiency caused by relatively more-uniform distribution of permeability. Accelerated recovery for high V_{DP} is because channeling of the injected fluids results in higher injectivity (Fig. 62). Low permeability constrains the path of injected fluid and hence fluids take path of the least resistance, causing accelerated recovery.

Multiple Realizations of the Same Permeability Field

To study the effect of multiple realizations of the same permeability field on surfactant flooding, four realizations were generated with the same log-normal statistics as the base case but a different random seed number. The statistics of these permeability fields are listed in Table 6.

Similar simulations to those of the base case were repeated using these permeability distributions. The results comparing the oil recovery versus time and pore volumes injected are shown in Figs. 63 and 64. Realizations 1 and 4 give similar results, whereas realizations 5 and 2 show the fastest and slowest recovery rate, respectively (Fig. 63). The oil recovery versus pore volumes plot shows that realizations 1 and 2 have the same ultimate recovery while realization 4 shows the lowest ultimate recovery. Ultimate recovery for realization 2 was about the same, but it took about 132 years for that recovery. Total injection rates are shown in Fig. 65, which shows a similar injectivity for realizations 1, 4, and 5 but an extremely low injectivity for realization 2. This was because the injector was located in a low-permeability layer (Fig. 66). Figure 67 shows the oil production rate for these realizations. Figures 68 and 69 show the effect of multiple realizations on the cumulative oil recovery and oil production rate for a permeability field with $V_{DP} = 0.9$. Figure 69 shows that the oil rate peaks at different times even for the same statistical properties, similar to the trend observed for the heterogeneous base case with V_{DP} of 0.8.

These unconditioned simulations show a very large variation in oil recovery and project life that can result by simply using different random assignment of permeability to the reservoir gridblocks from a permeability distribution with the same statistical parameters and variogram. By conditioning this reservoir distribution with reservoir data such as core data, well logs, pressure data, or tracers, this variation can be reduced. Conditional simulations are in progress.

Vertical-to-Horizontal Permeability Ratio

The vertical-to-horizontal permeability ratio (k_v/k_h) was varied from 1, 0.1 (base case), 0.01, to 0.001 to examine the effect of crossflow on the recovery. The permeability field was generated as before, but in each simulation only k_v/k_h was changed. These simulations were the similar to the base case. The major changes were that the salinity of the postflush was kept the same as that of the slug and drive (0.611 meq/ml) and the maximum injection rate was constrained to 2,000 B/D.

Figures 70 and 71 show the cumulative oil recovery plotted against pore volumes injected and time, respectively. Figure 70 shows that the ultimate oil recovery is not very sensitive to k_v/k_h ratio, but Fig. 71 shows that the oil recovery is greatly accelerated for higher k_v/k_h ratios. Increased crossflow causes better sweep of the reservoir and thus better recovery. Figure 72 shows the oil rate for different k_v/k_h ratios. This figure shows that oil rate is higher and the peak rate is accelerated for higher k_v/k_h ratios. This emphasizes the need for accurate reservoir description, since the k_v/k_h ratio affects the project economics.

Simulation of Surfactant Floods with Horizontal Wells

A series of surfactant/polymer simulations very similar to the above base case (except the skin was changed from -1 to -3) were made as a preliminary evaluation of the use of a horizontal rather than vertical injector. The areal location of the horizontal injector within the five-spot well pattern symmetry element is shown in Fig. 73. The horizontal injection well is linked to the vertical injection well and placed in the highest-permeability layer (layer 2). The high viscosity of injected polymer solution and the economic incentive for a short project life tend to drive us in the direction of horizontal injectors rather than producers.

The results of the simulations with vertical and horizontal well arrangements are plotted in Figs. 74 through 81. Cumulative oil recovery as a fraction of oil in place at the beginning of surfactant flooding is plotted versus time in Fig. 74 and versus pore volumes injected in Fig. 76. These plots show that the addition of a horizontal injection well reduced the ultimate oil recovery from 57.1% to 52.7%. However, the project life decreased significantly from 22.7 years to 11.3 years because of the greatly improved injectivity. The plot of the oil rate (Fig. 75) shows that the surfactant flood has effectively displaced an oil bank. With the horizontal injection well, the oil rate has increased from about 40 B/D to a peak of 370 B/D. With just the vertical wells, the rate has increased from about 15 B/D to a peak of about 150 B/D. Simulation of the surfactant flood with the horizontal injection well reaches a peak higher and earlier than simulation without the horizontal well. The plot of the injection rate (Fig. 78) and the plot of the pore volumes injected (Fig. 77) show that, as expected, the injectivity is much lower during injection of polymer than during injection of the low-viscosity chase water. It is during injection of polymer that the benefit of a horizontal injection well in reducing the project life is very apparent. Plots of the surfactant concentration and polymer concentration show the expected delays in the peaks. The peaks from simulation with only the vertical wells are slightly lower. The plot of effective salinity indicates that the effective salinity has been within the lower and upper limits for most of the simulation time and therefore near optimum until chase water is injected at a salinity lower than the lower limit.

Well spacing

Simulations were carried out using the same base case data except that the well pattern was reduced from 40 acres to 10 acres. Waterfloods and then surfactant floods with and without the horizontal injection well were made with this reduced pattern to see its effect. As expected, the lower acreage resulted in much shorter project lives. In the case of the vertical wells (Fig. 82), the surfactant-flood project life was reduced from 22.7 years to 6.2 years. With the horizontal injection well (Fig. 83), the project life was reduced from 11.2 years to 3.6 years.

Horizontal wellbore length

To see the effect of the horizontal wellbore length, additional simulations were carried out with the length of the wellbore equal to 3/4, 1/2, and 1/4 of its full length. The results of these simulations are shown in Fig. 84. The results for this specific case show that only half of its length was needed to obtain the full benefit of the horizontal well.

Multiple field realizations

To investigate the effect of multiple permeability-field realizations on surfactant flooding, several realizations were generated with the same log-normal statistics. The characteristics of these permeability field realizations are listed in Table 6. Vertical x-z cross sections of realizations 1 through 4 are plotted in Figs. 85 through 88. Simulations were made with each of these permeability fields with both vertical and horizontal injectors. The results comparing the oil recovery versus time and pore volumes injected are plotted in Figs. 89 through 92 for the vertical injector cases. As seen from Fig. 89, realizations 1, 4, and 5 give results relatively close to each other. Realization 3 gives a lower ultimate oil recovery at a significantly earlier time. This is an indication of poor sweep due to channeling. Realization 2 shows a very low injectivity, although the sweep is relatively good, as seen in Fig. 90. This is due to the injector being completed in a very low-permeability zone. A different situation happens when a horizontal injection well is used in these surfactant flood simulations. As seen in Fig. 91, realization 2 shows an improvement in injectivity. Realization 4 shows a decrease in sweep efficiency. Realization 3 shows poor sweep. Realizations 1 and 5 are still close and give good sweep and injectivity.

Vertical-to-horizontal permeability ratio

Next, the effect of the vertical-to-horizontal permeability ratio was studied. Using the base case data, only the vertical-to-horizontal permeability ratio was varied. The values studied were 1, 0.1, 0.01, 0.001, and 0.0001. Results are shown in Figs. 93 through 96. These results show that there is no major difference in the cumulative oil recovery at a given injected pore volumes (see Figs. 94 and 96). However, the injectivity decreases significantly with decreasing vertical-to-horizontal permeability ratio for both vertical and horizontal injectors (see Figs. 93 and 95). The decrease for the case of a horizontal injector is greater than for a vertical injector. The decrease in injectivity with lower vertical-to-horizontal permeability ratio is a general and very important trend in all cases that we have studied to date, which include waterfloods, polymer floods, miscible floods, and now surfactant floods. Thus, it is very important to have an accurate estimate of vertical permeability of any reservoir that is a candidate for improved oil recovery, yet this is generally a poorly known value, and techniques for measuring it are not well-known or routine to say the least. Some of our related research on the use of interwell tracers for reservoir characterization has addressed this important problem, and the reader is referred to our DOE reports on this subject for additional information.

Summary, Conclusions, and Future Work

Based on our study of surfactant flooding using stochastic reservoir descriptions, we have concluded the following: an increase in correlation length accelerates oil recovery but decreases ultimate oil recovery; the simulation results for a layered reservoir are overly optimistic compared to those of complex and realistic reservoirs that are generated stochastically; an increase in reservoir heterogeneity (as measured in this context by the variance of the permeability field) accelerates oil recovery but decreases ultimate oil recovery. Multiple realizations have shown that the oil recovery is sensitive to the uncertainty in the permeability field distribution, even when statistical properties are kept the same, and crossflow accelerates oil recovery but has little effect on ultimate oil recovery. Since all of these results used just one variogram and kept all other reservoir properties fixed (for example porosity and residual oil saturation), many variables remain to be studied.

For the base case simulation, a horizontal injection wellbore was found to improve the injectivity of a surfactant flood and to reduce the project life. The project life was reduced from 22.7 years to 11.3 years. Well spacing and pattern size directly affect the project life. A smaller well pattern results in a proportionately shorter project life. When well spacing was decreased by a factor of four, project life was reduced from 22.7 years to 6.2 years for the case of vertical wells and from 11.2 years to 3.6 years for the case of the horizontal injection well. A full-length wellbore may not be necessary. Simulation results show that only half of the full length is needed to obtain the full benefit of the horizontal injection wellbore for the case studied. Injectivity decreases with decreasing vertical-to-horizontal permeability ratio. A horizontal well helps remedy the problem of a low-injectivity vertical well that is completed in a low-permeability zone, such as in the case of realization 2 in our study. Obviously, a horizontal injection well may not improve the problem of severe channeling, since most of these cases already have a high injectivity such as in realization 3. A horizontal injection well may even worsen the sweep efficiency and lower the ultimate oil recovery at the economic limit if it enhances channeling and creates a shorter flow path to the production well, such as in the case of realization 4 of our study. The spatial variation of the permeability should be estimated as accurately as possible before initiating any surfactant field project. In case of large heterogeneity, horizontal wells should be drilled and completed in such a way that sections that could reduce sweep because of their high injectivity could be shut off .

At the present time we are studying the effect of various parameters on conditioned reservoirs, as well as the effect of process parameters on the surfactant flooding process using both horizontal and vertical wells.

NOMENCLATURE

a_i = Coefficients in the flux limiter functions

b_i = Coefficients in the flux limiter functions

C_{4a} = Concentration of polymer in aqueous phase

C_f = Pore compressibility, $M^{-1}LT^2$

C_t = Total compressibility, $M^{-1}LT^2$
$\tilde{C}_\kappa$ = Overall concentration of component κ
$\hat{C}_\kappa$ = Adsorbed concentration of component κ
C_κ^0 = Compressibility of component κ, $M^{-1}LT^2$
$C_{\kappa\ell}$ = Concentration of component κ in phase ℓ
C_{vs} = Constant volume heat capacity of rock, $L^2T^{-2}K^{-1}$
$C_{v\ell}$ = Constant volume heat capacity of phase ℓ, $L^2T^{-2}K^{-1}$
$C_{p\ell}$ = Constant pressure heat capacity of phase ℓ, $L^2T^{-2}K^{-1}$
d = Distance between node points, L
$D_{k\ell}$ = Molecular diffusion, L^2T^{-1}
f_ℓ = Fractional flow function of phase ℓ
F_ℓ = Flowing fraction of phase ℓ
$F_{\ell 0}$ = Flowing fraction of phase ℓ at fractional flow of zero
$F_{\ell 1}$ = Flowing fraction of phase ℓ at fractional flow of one
$F_{a\kappa}$ = Overall accumulation of component κ, L^3
$F_{t\kappa}$ = Overall transport of component κ, L^3T^{-1}
$F_{q\kappa}$ = Overall source or sink of component κ, L^3T^{-1}
$\vec{F}_\kappa$ = Overall mass flux of component κ, $ML^{-2}T^{-1}$
J = Jacobian matrix
k = Permeability, L^2
$\vec{\vec{k}}$ = Permeability tensor
k_a = Horizontal permeability, L^2
$k_{r\ell}$ = Relative permeability of phase ℓ
k_s = Permeability deviation coefficient
$k_{r\ell}^0$ = Endpoint relative permeability for phase ℓ
$\overline{K}$ = Dispersion coefficient, L^3T^{-1}
$\vec{\vec{K}}$ = Dispersion tensor
$K_{xx\kappa\ell}$, $K_{yy\kappa\ell}$ = Diagonal elements of the dispersion tensor for
$K_{zz\kappa\ell}$ component κ in phase ℓ, L^2T^{-1}
$K_{xy\kappa\ell}$, $K_{xz\kappa\ell}$ = Off diagonal elements of the dispersion tensor for
$K_{yx\kappa\ell}$, $K_{yz\kappa\ell}$ component κ in phase ℓ, L^2T^{-1}
$K_{zx\kappa\ell}$, $K_{zy\kappa\ell}$
$M_{\kappa\ell}$ = Mass transfer coefficient, T^{-1}
n_c = Total number of components
n_{cv} = Total number of volume occupying components
n_p = Total number of phases
n_{p_c} = Capillary pressure exponent

N_b = Total number of gridblocks
N_i = Number of iterations
N_{Pe} = Peclet number (L/a)
N_{RL} = Rapoport and Leas number
N_x, N_y, N_z = Number of gridblocks in the x, y, and z directions
$P_{c\ell\ell'}$ = Capillary pressure between phases ℓ and ℓ', $ML^{-1}T^{-2}$
P_ℓ = Phase pressure, $ML^{-1}T^{-2}$
P_R = Reference pressure, $ML^{-1}T^{-2}$
P_{wf} = Well flowing pressure, $ML^{-1}T^{-2}$
P_α = Exponent for calculating shear rate dependence of polymer viscosity
P_Δ = Cell Peclet number ($\Delta x/\alpha$)
PI = Productivity index, $M^{-1}L^4T$
q_κ = Unit volumetric source or sink of component κ, T^{-1}
$q_{\kappa f}$ = Unit volumetric injection/production rate of component κ, T^{-1}
$q_{\kappa r}$ = Unit volumetric reaction rate of component κ, T^{-1}
q_H = Unit enthalpy source term, MLT^{-3}
Q = Rate, L^3T^{-1}
r = Ratio of consecutive gradients
r_κ = Unit mass source or sink of component κ, $ML^{-3}T^{-1}$
$r_{\kappa\ell}$ = Reaction rate of component κ in phase ℓ, $L^{-3}T^{-1}$
$r_{\kappa S}$ = Reaction rate of component κ in stationary phase ℓ, $L^{-3}T^{-1}$
R = Expansion ratio
R_k = Permeability reduction factor
R_m = A random number with a normal distribution
S^* = Saturation value at zero capillary pressure
S_ℓ = Phase saturation
$S_{n\ell}$ = Normalized phase saturation
S_p = Exponent for calculating salinity dependence of polymer viscosity
$S_{\ell r}$ = Residual saturation of phase ℓ
S_{wi} = Initial water saturation
Δt = Timestep size, T
T = Transmissibility, L^3, Temperature, K
$\bar{T}$ = Convection coefficient, $M^{-1}L^4T$
$\vec{u}_\ell$ = Flux, LT^{-1}
w_κ = Overall mass concentration of component κ, ML^{-3}
$\Delta x, \Delta y, \Delta z$ = Gridblock sizes in the x, y, and z directions, L

Greek Symbols

α, β, γ = Coefficient for nonuniform grids

$\alpha_{L\ell}$ = Longitudinal dispersivity of phase ℓ, L
$\alpha_{T\ell}$ = Transverse dispersivity of phase ℓ, L
β_P = Effective salinity parameter for polymer viscosity
$\dot{\gamma}_{1/2}$ = Shear rate at which polymer viscosity is one-half the polymer viscosity at zero shear rate, T^{-1}
$\dot{\gamma}_c$ = Coefficient in equivalent shear rate equation
γ_ℓ = Specific weight of phase ℓ, $ML^{-2}T^{-2}$
ε = Error between numerical solution and analytical solution
ε_p = Relative changes in primary variables
λ = Courant number
λ_a = Relative mobility of the aqueous phase, $M^{-1}LT$
λ_o = Relative mobility of the oleic phase, $M^{-1}LT$
$\lambda_{r\ell}$ = Relative mobility of phase ℓ, $M^{-1}LT$
λ_T = Constant thermal conductivity, $MLT^{-3}K^{-1}$
μ_ℓ = Phase viscosity, $ML^{-1}T^{-1}$
$[\mu]$ = Intrinsic polymer viscosity
μ_w = Water viscosity, $ML^{-1}T^{-1}$
ρ_κ = Density of component κ, ML^{-3}
$\rho_{\kappa\ell}$ = Density of component κ in phase ℓ, ML^{-3}
$\rho_{\kappa R}$ = Reference density of component κ, ML^{-3}
ρ_ℓ = Density of phase ℓ, ML^{-3}
ρ_s = Density of rock, ML^{-3}
ϕ = Porosity
ϕ_R = Porosity at reference pressure
φ = Flux limiter function
φ_b = Upper bound of TVD flux limiter function
Φ = Potential, $ML^{-1}T^{-2}$

Subscripts and Superscripts

a = Accumulation term index
a, w = Aqueous phase index
avg = Arithmetic mean
d = Dendritic fraction
f = Flowing fraction
i, j, k = Spatial indexes in the x, y, and z directions
k = Component index
ℓ = Phase index
L = Longitudinal
n = Timestep index

o = Oleic phase
q = Source or sink term index
r = Residual, or relative property
t = Transport term index
T = Transverse

REFERENCES

Abbaszadeh-Denghani, M. and W.E. Brigham: "Analysis of Well-to-Well Tracer Flow To Determine Reservoir Layering," *J. Pet. Tech.* (Oct. 1984) **36**, 1753-1762.

Amyx, J.W., D.M. Bass, and R. L. Whiting: *Petroleum Reservoir Engineering: Physical Properties*, McGraw-Hill Book Company, New York, 1960.

Bhuyan, D., L.W. Lake, and G.A. Pope: "Mathematical Modeling of High-pH Chemical Flooding," paper SPE/DOE 17398 presented at the 1988 SPE/DOE Symposium on Enhanced Oil Recovery, Tulsa, OK, April 17-20.

Brantferger, K.M.: "Development of a Thermodynamically Consistent, Fully Implicit, Compositional, Equation-of-State, Steamflood Simulator," Ph.D. dissertation, U. of Texas, Austin (May 1991).

Camilleri, D., A. Fil, G.A. Pope, B. Rouse, and K. Sepehrnoori: "Improvements in Physical Property Models Used in Micellar/Polymer Flooding," *SPE Reser. Eng.* (1987) **2**, No. 4, 433-440.

Chang, Y.: "Development of a Three-Dimensional, Equation-of-State Compositional Reservoir Simulator for Miscible Gas Flooding," Ph.D. dissertation, U. of Texas, Austin (Aug. 1990).

Coats, K.H. and B.D. Smith: "Dead-End Pore Volume and Dispersion in Porous Media," *Soc. Pet. Eng. J.* (Mar. 1964) **4**, 73-84; Trans., AIME **231**.

Datta Gupta, A., G.A. Pope, K. Sepehrnoori, and R.L. Thrasher: "A Symmetric, Positive Definite Formulation of a Three-Dimensional Micellar/Polymer Simulator," *SPE Reser. Eng.* (Nov. 1986) **1**, 622-632.

Datta Gupta, A., L.W. Lake, G.A. Pope, K. Sepehrnoori, and M.J. King: "High Resolution Monotonic Schemes for Reservoir Fluid Flow Simulation," *In Situ* (1991) **15**, No. 3, 289-317.

Delshad, M., G.A. Pope, and K. Sepehrnoori: "A Compositional Simulator for Modeling Surfactant Enhanced Aquifer Remediation," in progress, 1994.

Dykstra, H. and R.L. Parsons: "The Prediction of Oil Recovery by Water Floods," *Secondary Recovery of Oil in the United States*, API (1950), 160-174.

Ferreira, L.E.A.: "Reservoir Characterization Using Single-Well Tracer Tests," Ph.D. dissertation, U. of Texas, Austin (Aug. 1992).

Holing, K., J. Alvestad, and J. Trangenstein: "The Use of Second-Order Godunov-type Methods for Simulating EOR Processes in Realistic Reservoir Models," *Proc.*, 2nd European Conference on the Mathematics of Oil Recovery, Paris (Nov. 1990), 101-111.

Kerbs, L.: "The variogram," *Computer Oriented Geological Society Computer Contributions (* Aug. 1986) **2**, No. 2, 54-59.

Liu, J., M. Delshad, G.A. Pope, and K. Sepehrnoori: "Application of Higher-Order Flux-Limited Methods in Compositional Simulation," accepted for publication by *Transport in Porous Media*, Aug. 1993.

Mehra, R.K., R.A. Heidemann, and K. Aziz: "An Accelerated Successive Substitution Algorithm," *Can. J. Chem. Eng.* (1983) **61**, No. 4, 590-596.

Oppe, T.C., W. D. Joubert, and D.R. Kincaid: "*NSPCG User's Guide Version 1.0,* A Package for Solving Large Sparse Linear Systems by Various Iterative Methods," Center for Numerical Analysis, U. of Texas, Austin (April 1988).

Rubin, B. and W.L. Buchanan: "A General Purpose Thermal Model," *Soc. Pet. Eng. J.* (Apr. 1985) **25**, 202-214.

Pope, G.A. and R.C. Nelson: "A Chemical Flooding Compositional Simulator," *Soc. Pet. Eng. J.* (Oct. 1978) **18**, 339-354.

Pope, G.A.: "The Application of Fractional Flow Theory to Enhanced Oil Recovery," *Soc. Pet. Eng. J.* (1980) **20**, No. 3, 191-205.

Richardson, J.G., J.K. Kerver, J.A. Hafford, and J.S. Osoba: "Laboratory Determination of Relative Permeability," *Trans.*, AIME (1952) **195**, 187-196.

Saad, N.: "Field Scale Simulation of Chemical Flooding," Ph.D. dissertation, U. of Texas, Austin (Aug. 1989).

Saad, N., G.A. Pope, and K. Sepehrnoori: "Application of Higher-Order Methods in Compositional Simulation," *SPE Reser. Eng.* (Nov. 1990) **5**, 623-630.

Smith, J.C., M. Delshad, G.A. Pope, W.G. Anderson, and D. Marcel: "An Analysis of Unsteady-State Displacements Using a Capacitance-Dispersion Model," *In Situ* (1988) **12**, Nos. 1 and 2, 41-78.

Vinsome, P.K.W., and J. Westerveld: "A Simple Method for Predicting Cap and Base Rock Heat Losses in Thermal Reservoir Simulators," *J. Can. Pet. Tech.* (July 1980), 87-90.

Yang, A. P.: "Stochastic Heterogeneity and Dispersion," Ph.D. dissertation, U. of Texas, Austin (Dec. 1990).

Table 1. TVD flux and its derivatives

TVD Flux

$$\left\{ \begin{array}{l} f_{i+1/2} = f_i + \varphi_i(r_i)\delta_x f_{i+1} \\ \varphi_i(r_i) = a_i r_i + b_i \\ r_i = \delta_x f_i / \delta_x f_{i+1} \end{array} \right.$$

Derivatives of TVD Flux

$$\left\{ \begin{array}{l} \dfrac{\partial f_{i+1/2}}{\partial f_{i-1}} = -(\varphi_r)_i \\ \dfrac{\partial f_{i+1/2}}{\partial f_i} = 1 - \varphi_i + (1 + r_i)(\varphi_r)_i \\ \dfrac{\partial f_{i+1/2}}{\partial f_{i+1}} = \varphi_i - r_i(\varphi_r)_i \end{array} \right.$$

Flux-Limiter Functions and Their Derivatives

Scheme	r_i	φ_i	$(\varphi_r)_i$
Without TVD	$(-\infty, +\infty)$	$a_i r_i + b_i$	a_i
With TVD	$(-\infty, 0)$	0	0
	$(0, b_i/(1-a_i))$	r_i	1
	$(b_i/(1-a_i), (1-b_i)/a_i)$	$a_i r_i + b_i$	a_i
	$((1-b_i)/a_i, +\infty)$	1	0
Van Leer	$(-\infty, +\infty)$	$2r_i/(a_i r_i + b_i)$	$2b_i/(a_i r_i + b_i)^2$

Table 1. TVD flux and its derivatives (cont'd.)

Coefficients in the Flux Limiter Functions and Their Derivatives

Scheme	a_i	b_i
One-Point Upstream	0	0
Two-Point Upstream	$\frac{\Delta x_i}{\Delta x_{i-1}+\Delta x_i}$	0
Leonard	$1/6$	$1/3$
Saad	$\frac{\Delta x_i}{3(\Delta x_{i-1}+\Delta x_i)}$	$\frac{2\Delta x_i}{3(\Delta x_i+\Delta x_{i+1})}$
High-Order	$\frac{\Delta x_i \Delta x_{i+1}}{(\Delta x_i+\Delta x_{i-1})(2\Delta x_i+\Delta x_{i-1}+\Delta x_{i+1})}$	$\frac{\Delta x_i(2\Delta x_i+\Delta x_{i-1})}{(\Delta x_i+\Delta x_{i+1})(2\Delta x_i+\Delta x_{i-1}+\Delta x_{i+1})}$
Van Leer	$1+\frac{\Delta x_{i+1}}{\Delta x_i}$	$1+\frac{\Delta x_{i-1}}{\Delta x_i}$

Table 2. Comparison of CPU time using direct and iterative solvers

	Iterative Solver OMIN		Direct Solver LU Decomposition
CPU Time (sec)			
Solver	1961.2		3569.6
Total	2071.6		3653.6
Solver/Total (%)	94.6		97.7
Iterative Solver/Direct Solver		0.567	

Ideal tracer flow in five-spot pattern
Peclet number: 500
Number of gridblocks: 30x30
Courant number: 3.0
Pore volumes injected: 1.3

Table 3. Comparison of timestepping algorithms

		Algorithm		
	Constant Timestep	1	2	3
CPU (sec)	2.5	17.2	2.2	1.9
Number of Successful Iterations	493	934	401	389
Number of Failed Iterations	0	2552	36	0
Total Number of Iterations	493	3486	437	389
Number of Timesteps	50	85	26	29
Average Number of Iterations Per Timestep	9.9	41.0	15.4	13.4
Average Courant Numbers	0.5	0.29	0.96	0.86

Polymerflood in homogeneous five-spot pattern
Number of gridblocks: 5x5
Maximum Courant number: 3.0
Minimum Courant number: 0.01
Pore volumes injected: 1.0

Table 4. Base case input data for surfactant simulations

Dimensions of reservoir simulated	660 ft x 660 ft x 140 ft
Number of gridblocks in the x, y, and z directions	11 x 11 x 5
Uniform gridblock sizes	60 ft x 60 ft x 28 ft
Porosity	0.136
Arithmetic average of the permeability	148.1 md
Reservoir depth	3,500 ft
Initial reservoir pressure	900 psia
Average initial water saturation	0.709
Initial salinity expressed in total equivalent anions	0.611 meq/ml
Initial divalent ions concentration	0.1275 meq/ml
Residual water saturation	0.14
Residual oil saturation	0.25
Endpoint relative permeability of water	0.106
Endpoint relative permeability of oil	0.8
Exponent of the water relative permeability curve	2.1
Exponent of the oil relative permeability curve	1.7
Water viscosity	0.74 cp
Oil viscosity	7.78 cp
Water specific weight	0.433 psi/ft
Oil specific weight	0.3882 psi/ft
Surfactant specific weight	0.42 psi/ft
Longitudinal dispersivity	0.16 ft
Transverse dispersivity	0.04 ft
Wellbore radius	0.2 ft
Skin factor of injection well	-1
Injection pressure	1,250 psia
Production pressure	250 psia

Table 5. Base case injection scheme

Initial conditions	
End of waterflood criterion	98% water cut
Anion concentration	0.611 meq/ml
Divalent ion concentration	0.1275 meq/ml
Surfactant/polymer slug	
Slug size	0.25 PV
Surfactant concentration	0.025 volume fraction
Polymer concentration	0.10 wt%
Anion concentration	0.611 meq/ml
Divalent ion concentration	0.1275 meq/ml
Polymer drive slug	
Slug size	0.5 PV
Polymer concentration	0.10 wt%
Anion concentration	0.611 meq/ml
Divalent ion concentration	0.1275 meq/ml
Chase water drive	
Anion concentration	0.2 meq/ml
Divalent ion concentration	0.1275 meq/ml
Economic limit of surfactant flood	99% water cut

Table 6. Statistical data for permeability field realizations

	Realization #1 (Base case)	Realization #2	Realization #3	Realization #4	Realization #5
Dykstra-Parsons coefficient	0.8	0.8	0.8	0.8	0.8
Geometric average (md)	50.55	50.55	50.55	50.55	50.55
Arithmetic average (md)	181.8	156	211.8	155.7	167.5
Minimum (md)	0.289	0.289	0.272	0.816	0.136
Maximum (md)	4,358	2,444	13,923	3,107	6,218
X correlation length (ft)	660	660	660	660	660
Y correlation length (ft)	660	660	660	660	660
Z correlation length (ft)	28	28	28	28	28

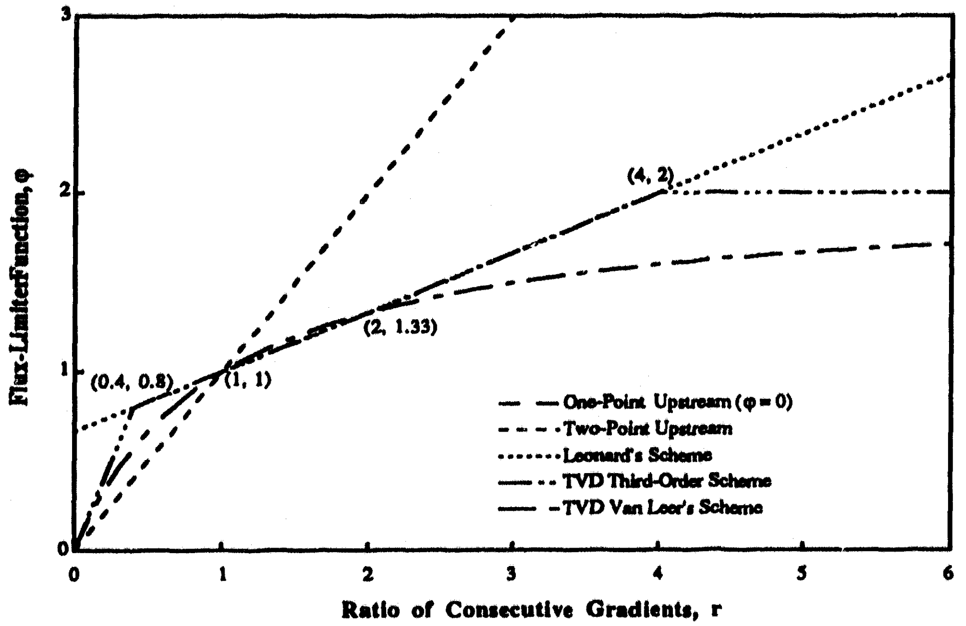

Fig. 1 Flux-limiter functions corresponding to different schemes.

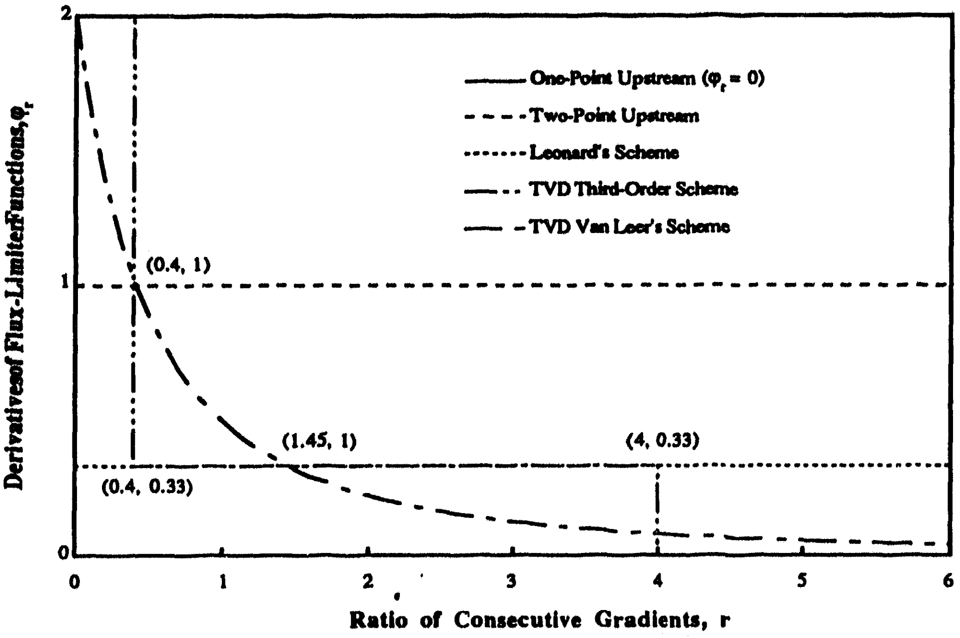

Fig. 2 Derivatives of flux-limiter functions corresponding to different schemes.

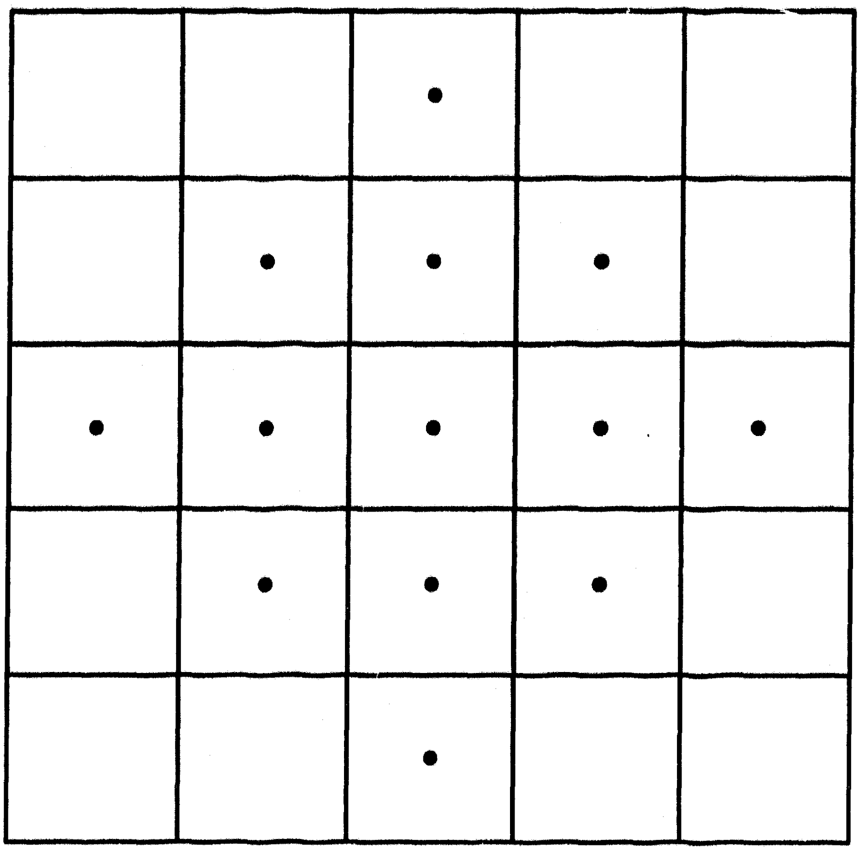

Fig. 3 Gridpoints involved in the high-order finite-difference scheme.

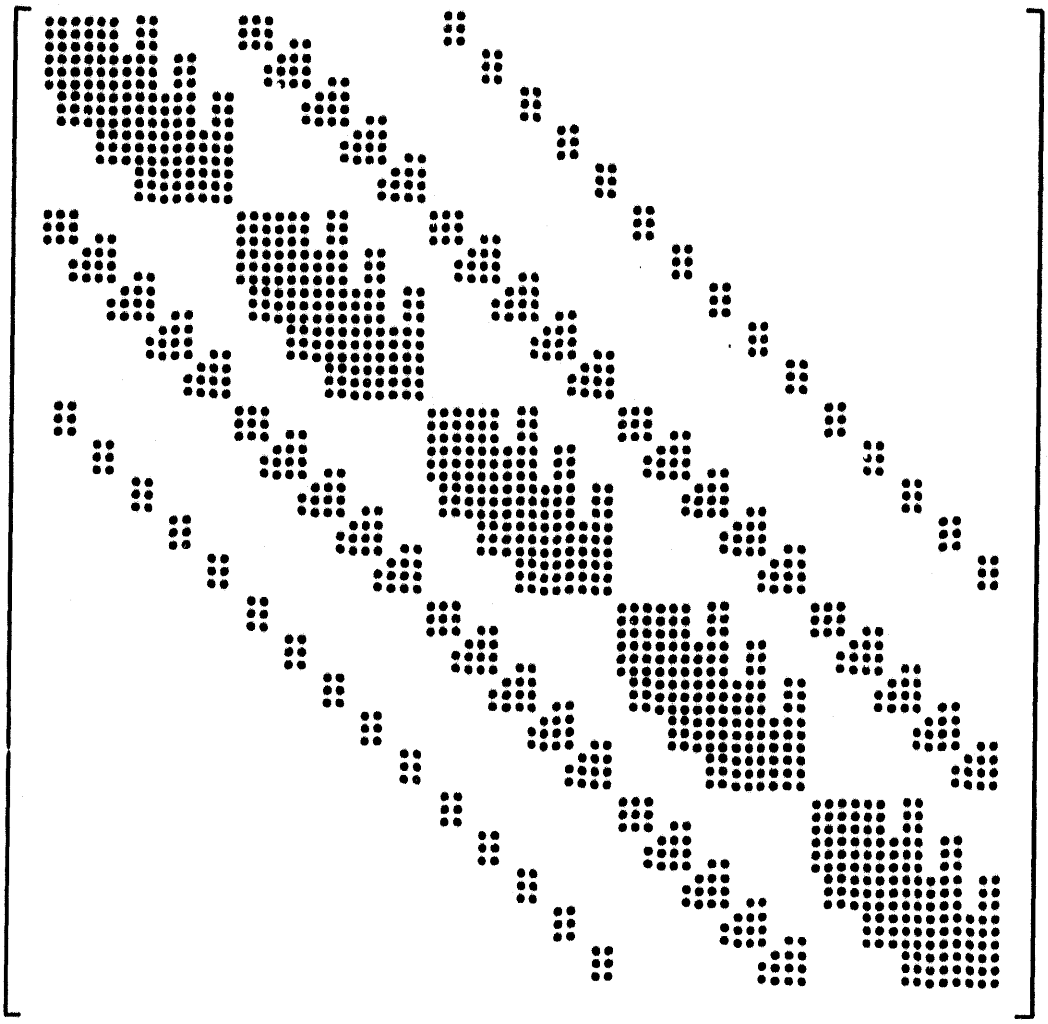

Fig. 4 Matrix structure of simulating a two-dimensional, two-component problem using the fully implicit formulation and the high-order method with 5x5 gridblocks.

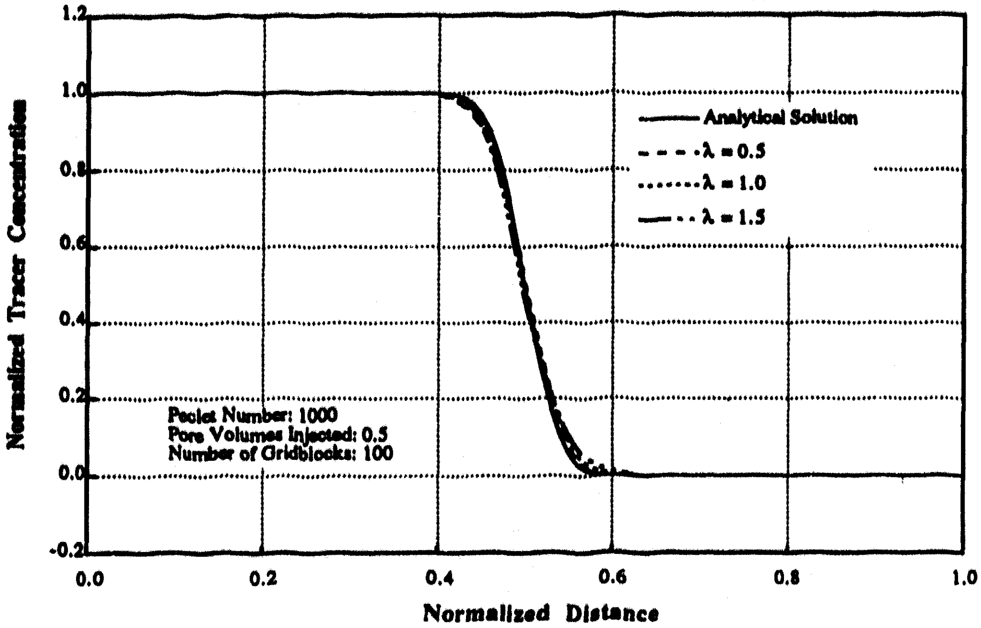

Fig. 5 Simulation of one-dimensional miscible water/tracer flow using the fully implicit formulation and the TVD high-order scheme with different Courant numbers.

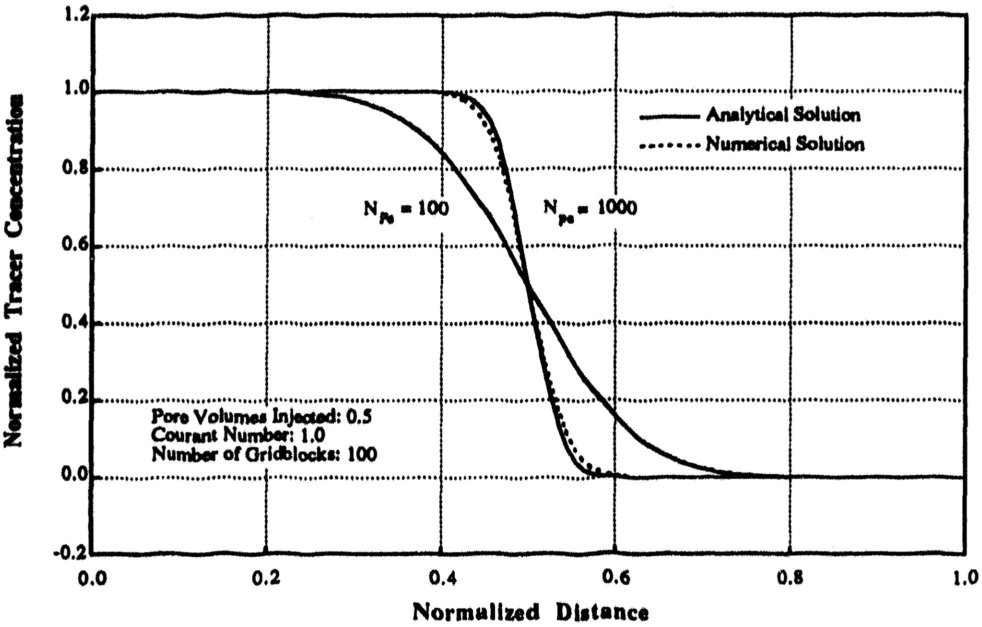

Fig. 6 Simulation of one-dimensional miscible water/tracer flow of different Peclet numbers using the fully implicit formulation with the TVD high-order scheme.

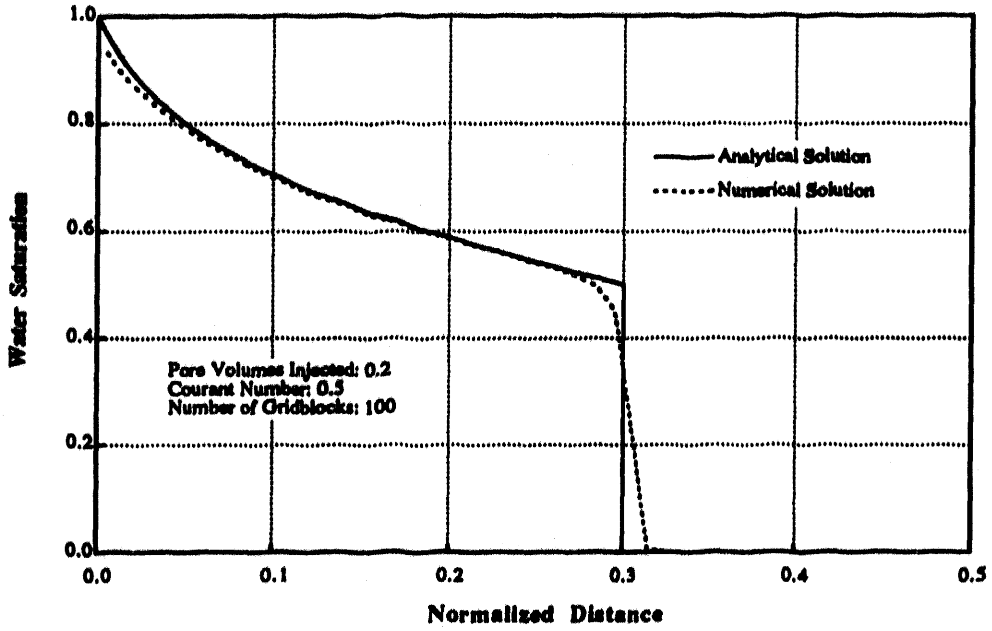

Fig. 7 Simulation results of one-dimensional waterflood using the fully implicit formulation with the TVD high-order scheme.

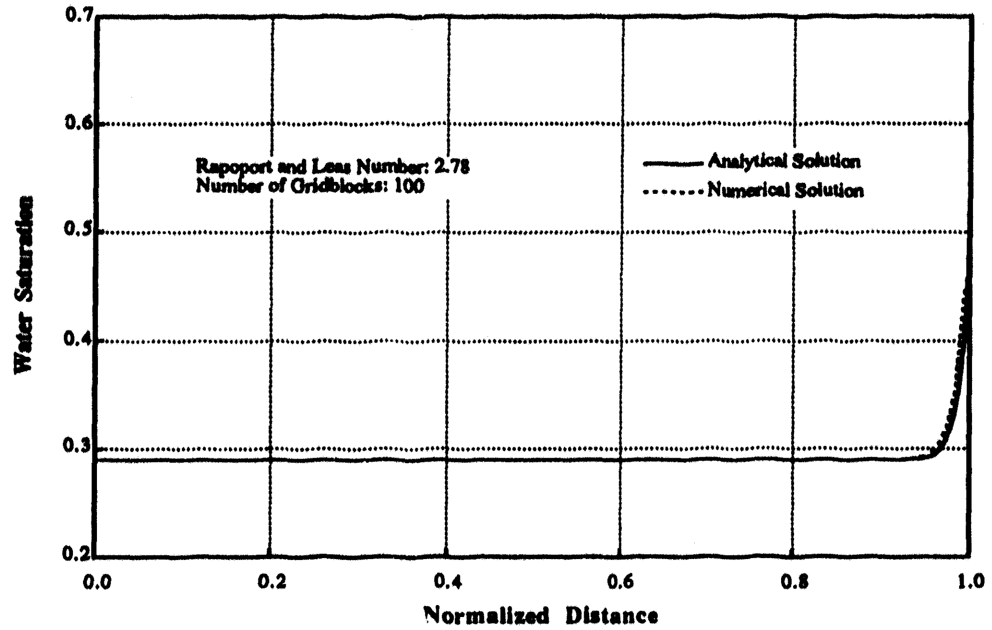

Fig. 8 Simulation results illustrating the capillary end effect ($S^*=0.65$) using the fully implicit formulation with the TVD high-order scheme.

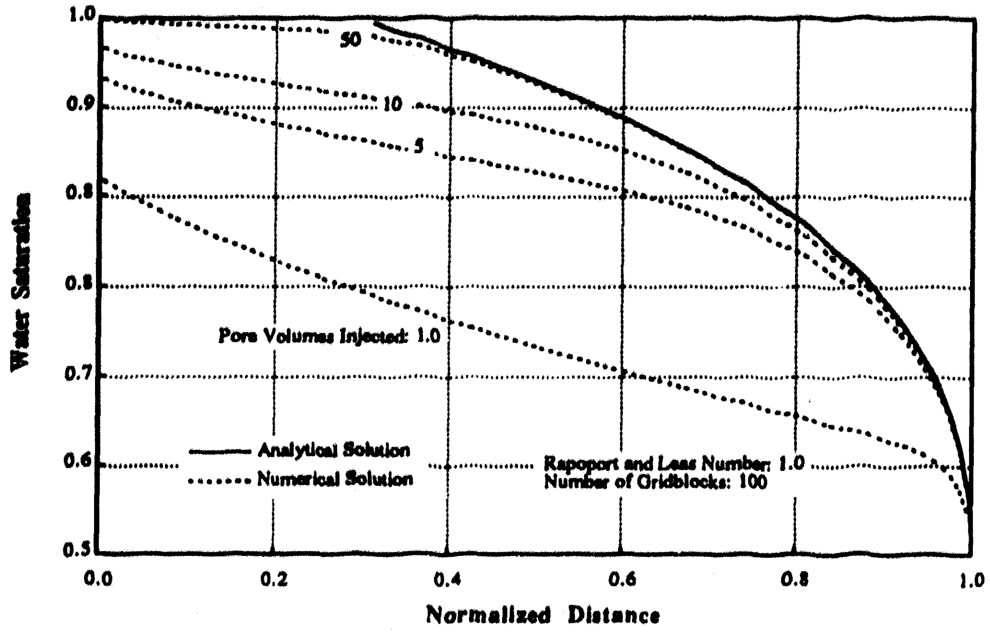

Fig. 9 Simulation results illustrating the capillary end effect (S^*=0.5) using the fully implicit formulation with the TVD high-order scheme.

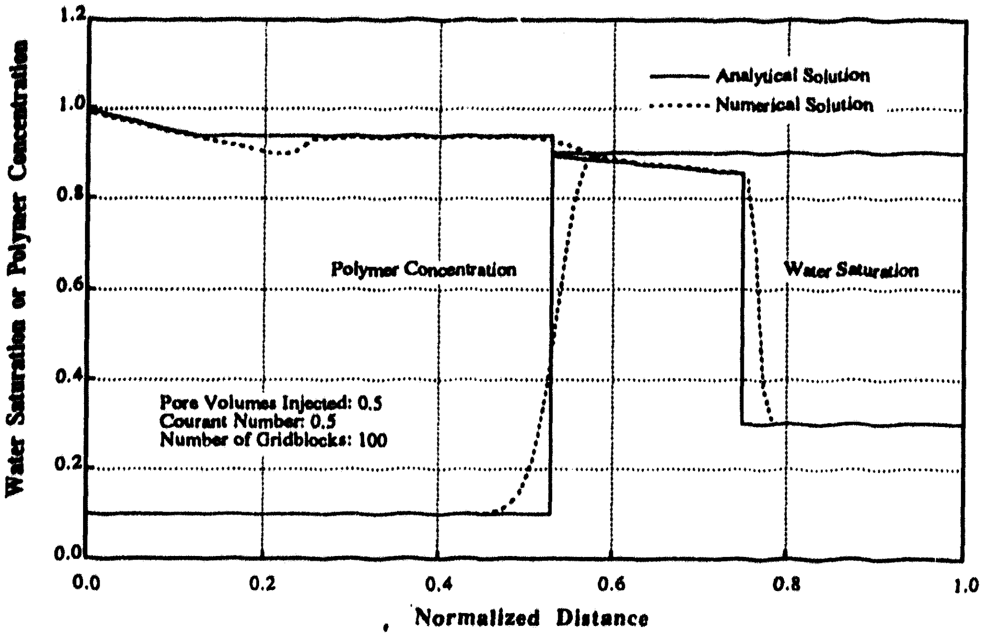

Fig. 10 Profiles obtained simulating Holing's one-dimensional polymerflood problem using the fully implicit formulation with the TVD high-order scheme.

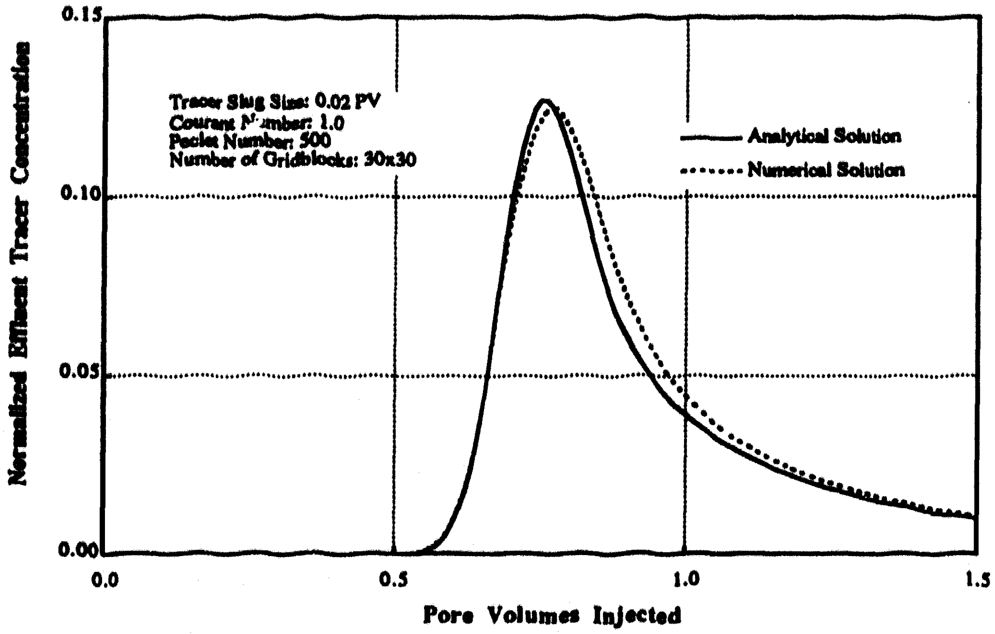

Fig. 11 Simulation results of ideal tracer flow in a homogeneous five-spot pattern using the fully implicit formulation with the TVD high-order scheme.

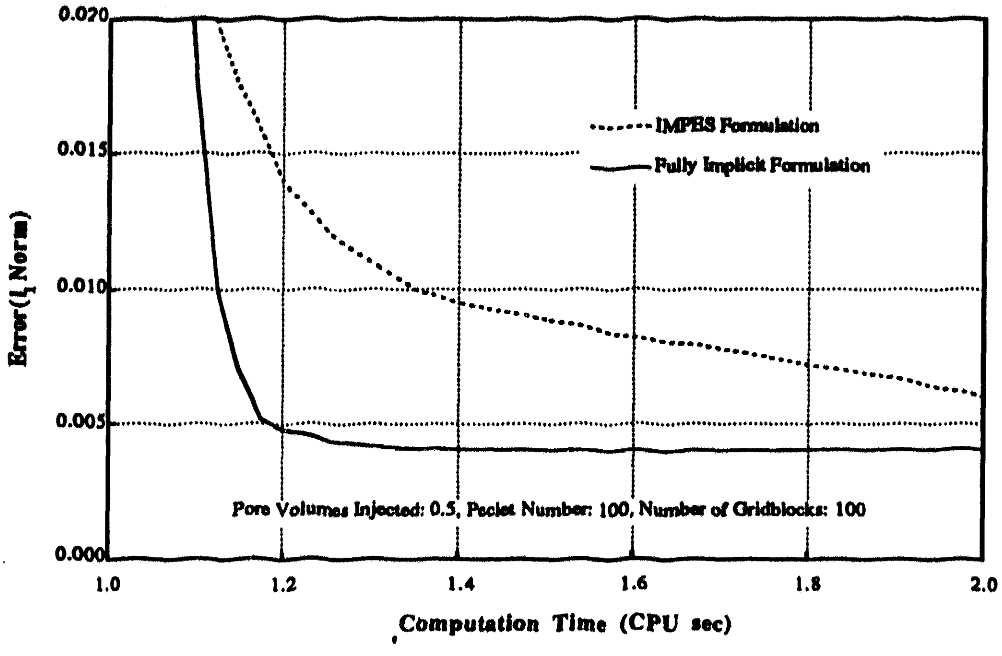

Fig. 12 Computational efficiency of simulating one-dimensional miscible water/tracer flow using the TVD high-order scheme.

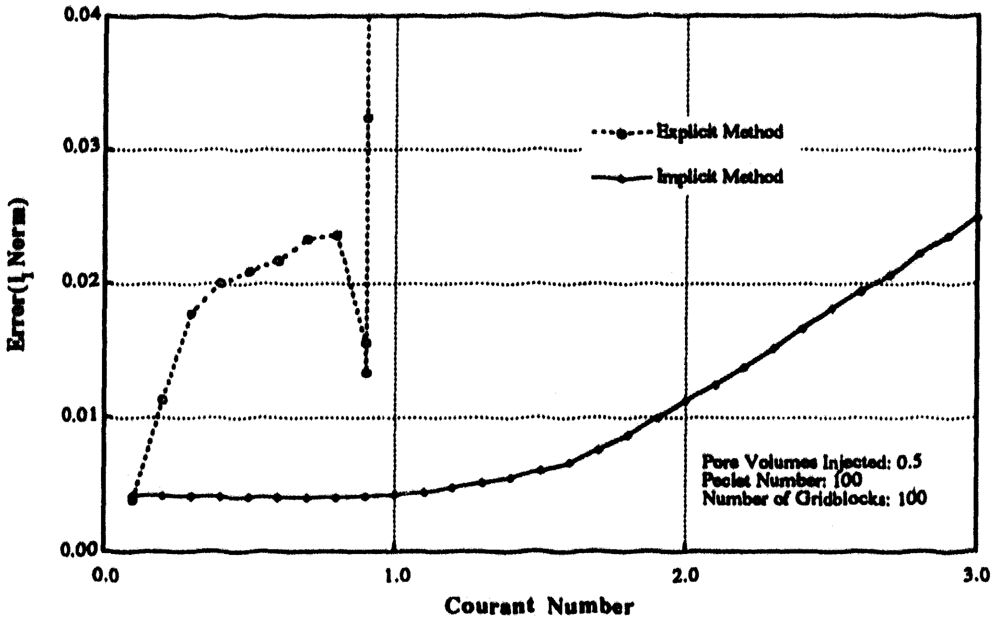

Fig. 13 Error of simulating one-dimensional miscible water/tracer flow using the TVD high-order scheme at different Courant numbers.

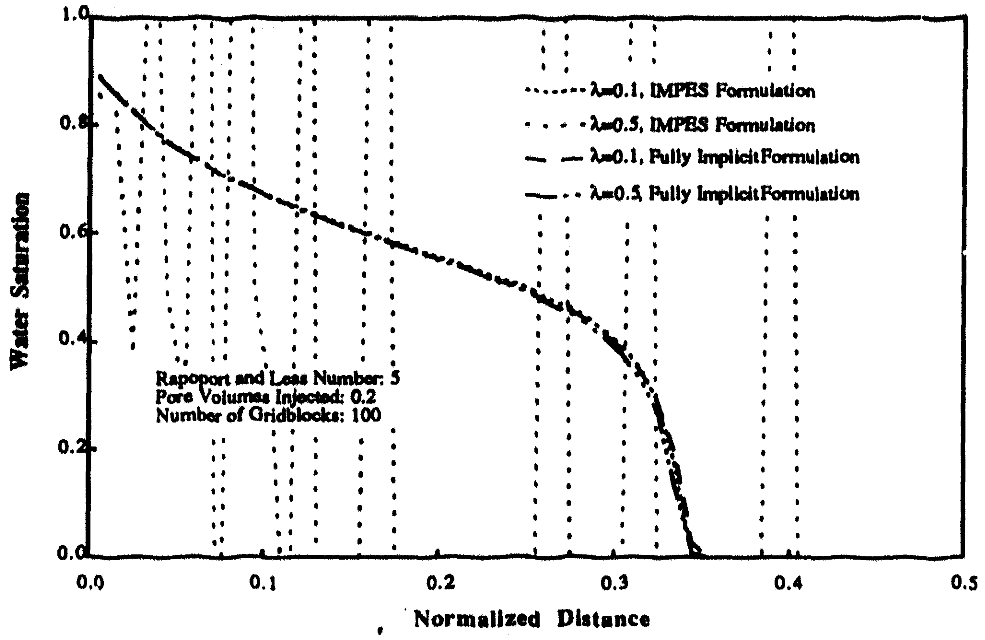

Fig. 14 Effect of Courant number on simulating a one-dimensional waterflood using the TVD high-order scheme.

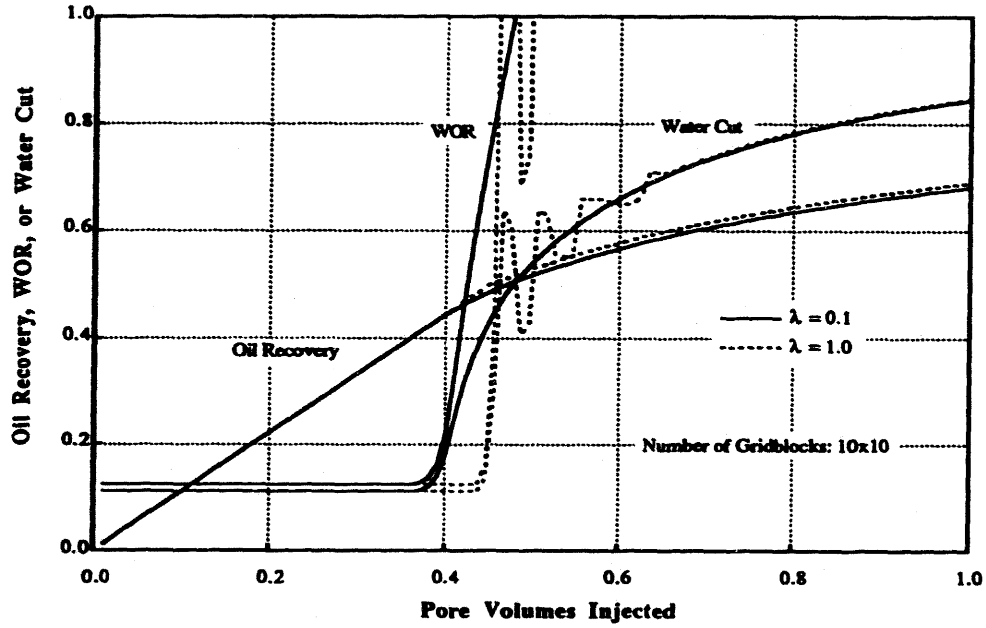

Fig. 15 Effect of Courant number on simulating a two-dimensional waterflood using the IMPES formulation with the TVD high-order scheme.

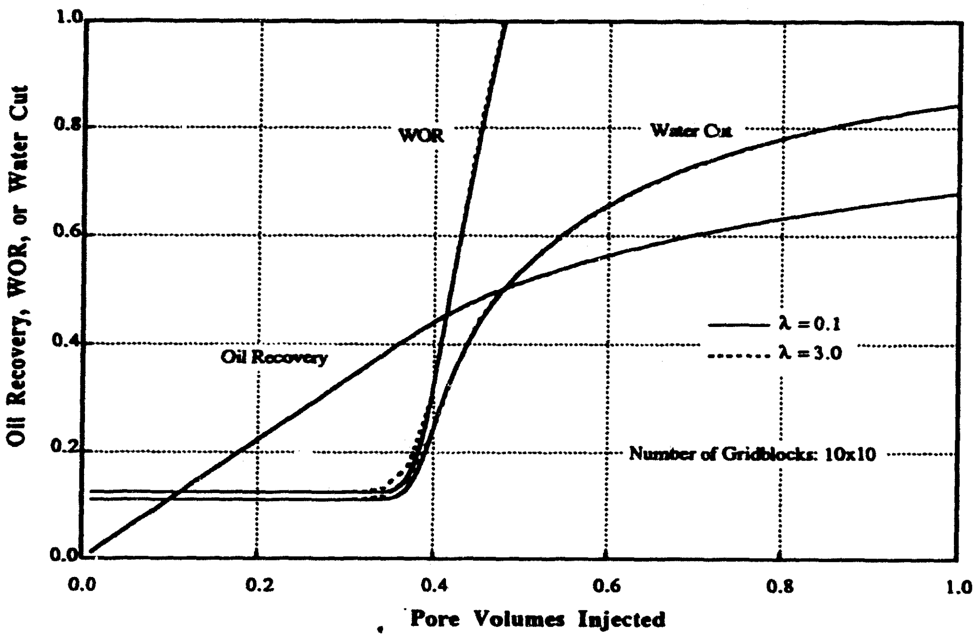

Fig. 16 Effect of Courant number on simulating a two-dimensional waterflood using the fully implicit formulation with the TVD high-order scheme.

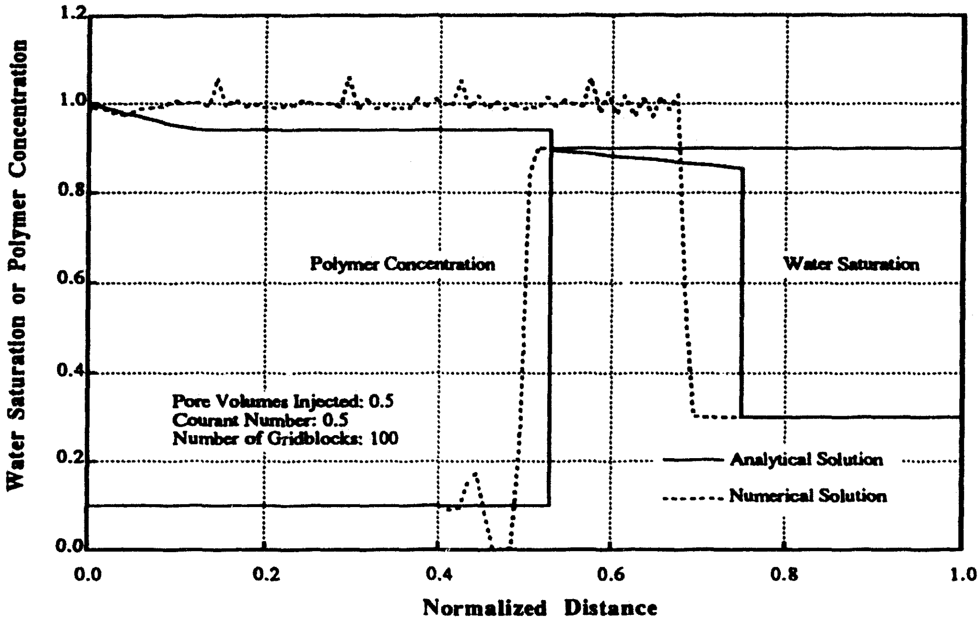

Fig. 17 Profiles of simulating Holing's one-dimensional polymerflood problem using the IMPES formulation with the TVD high-order scheme.

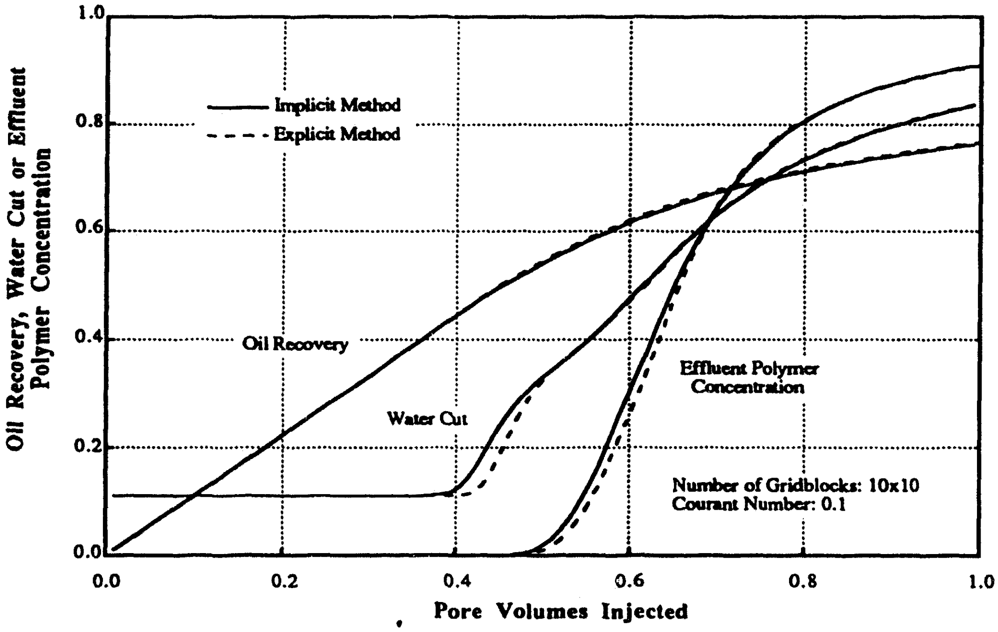

Fig. 18 Simulation results of a two-dimensional polymerflood in a homogeneous five-spot pattern using the TVD high-order scheme.

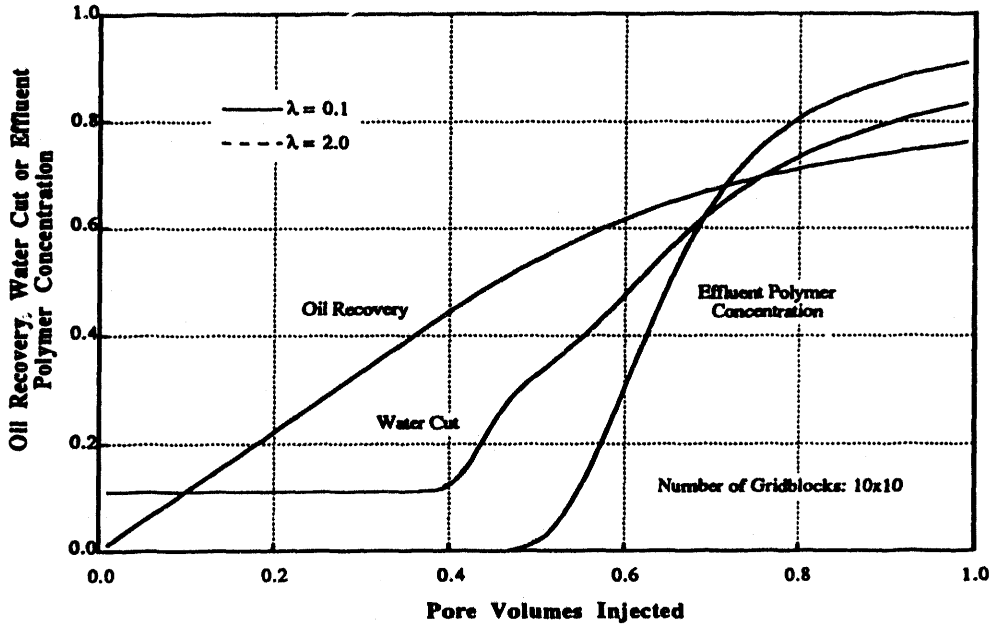

Fig. 19 Simulation results of a two-dimensional polymerflood in a homogeneous five-spot pattern using the fully implicit formulation with the TVD high-order scheme.

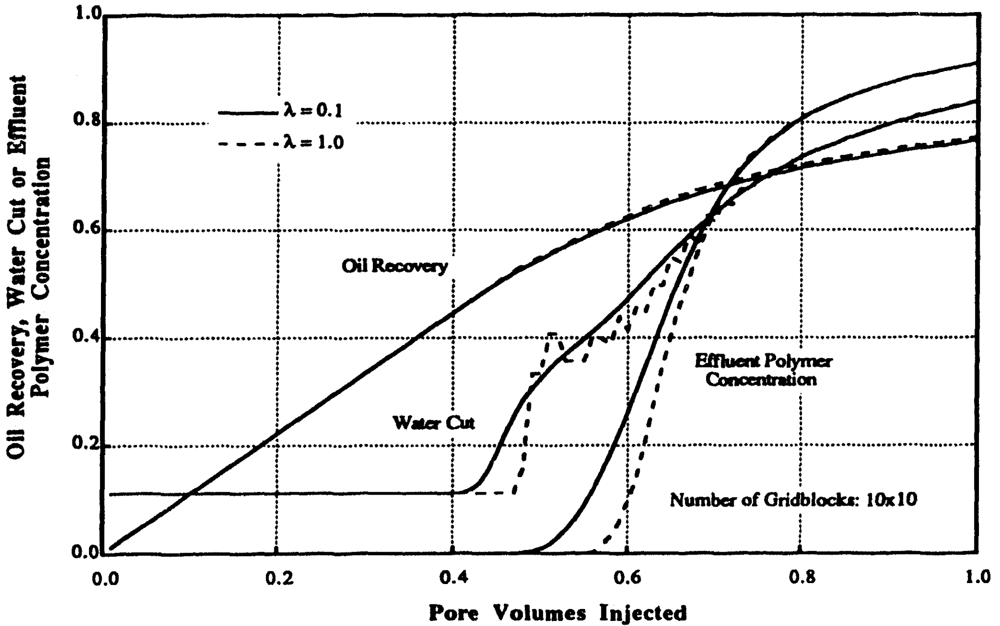

Fig. 20 Simulation results of a two-dimensional polymerflood in a homogeneous five-spot pattern using the IMPES formulation with the TVD high-order scheme.

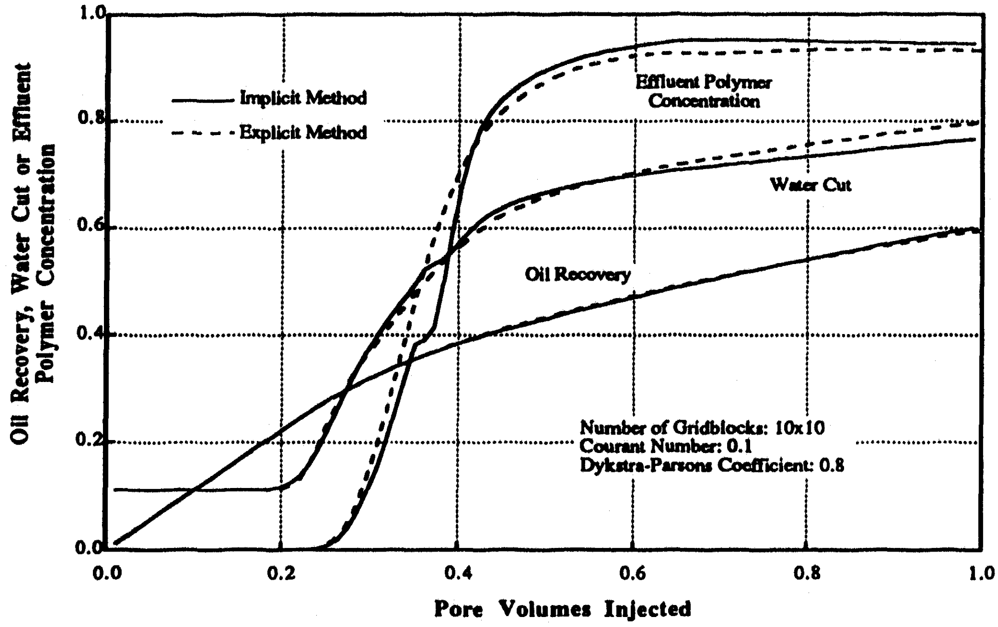

Fig. 21 Simulation results of a two-dimensional polymerflood in a heterogeneous five-spot pattern using the TVD high-order scheme.

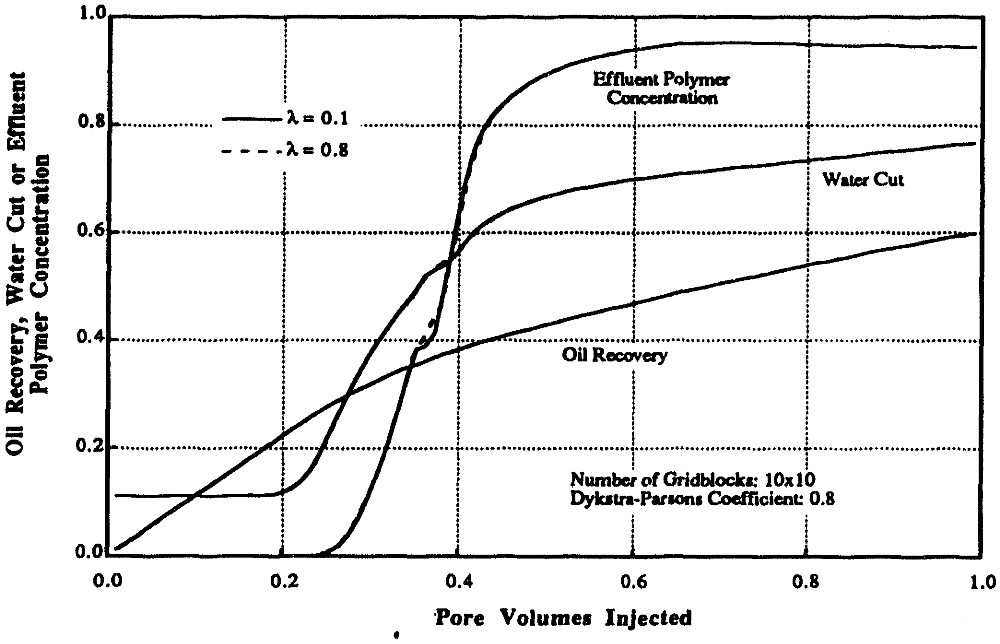

Fig. 22 Simulation results of a two-dimensional polymerflood in a heterogeneous five-spot pattern using the fully implicit formulation with the TVD high-order scheme.

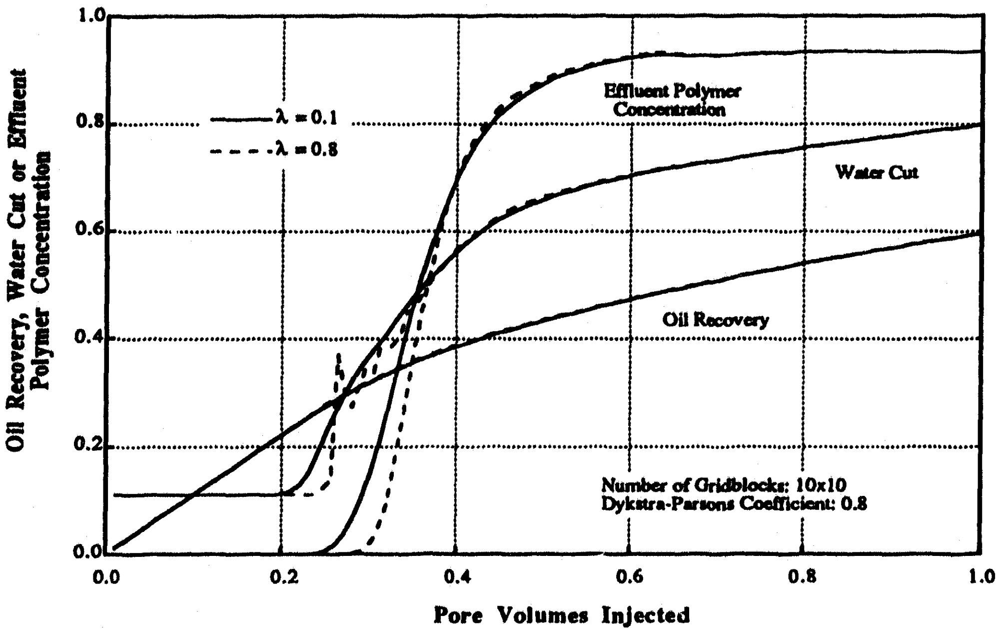

Fig. 23 Simulation results of a two-dimensional polymerflood in a heterogeneous five-spot pattern using the IMPES formulation with the TVD high-order scheme.

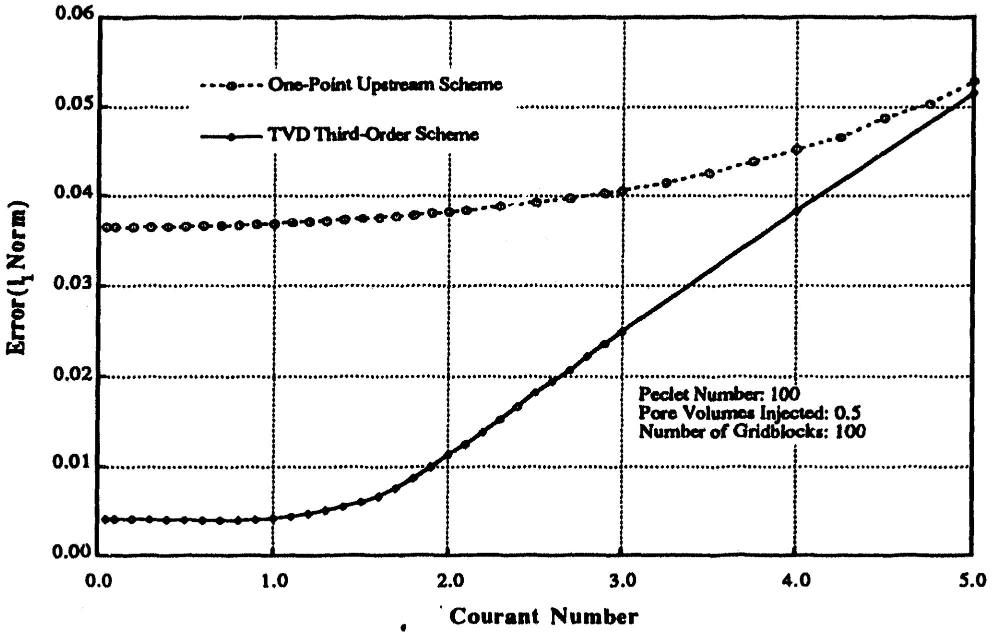

Fig. 24 Error of simulating one-dimensional miscible water/tracer flow using the fully implicit formulation at different Courant numbers.

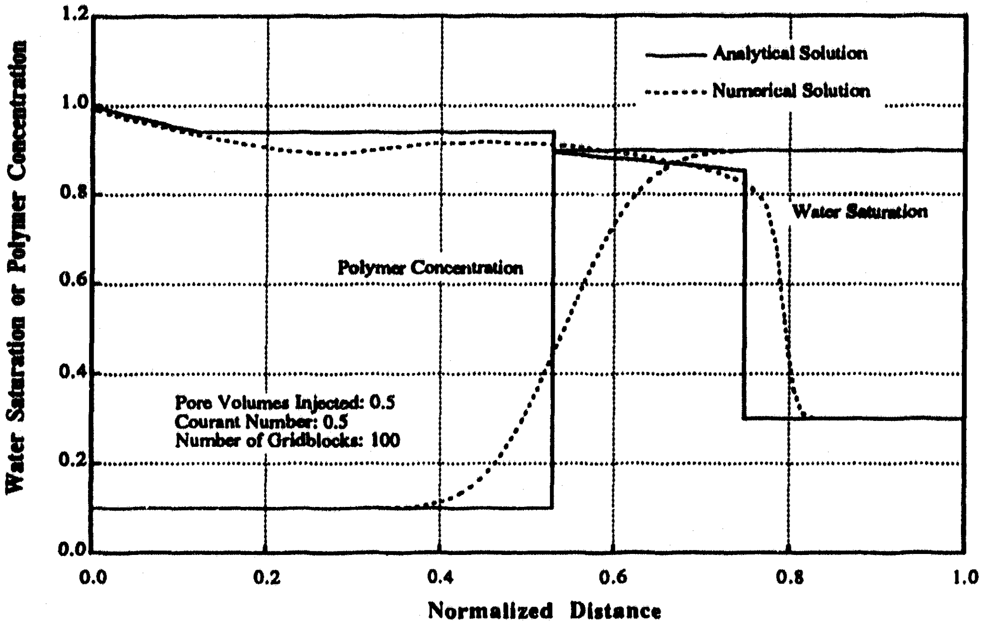

Fig. 25 Profiles of simulating Holing's one-dimensional polymerflood problem using the fully implicit formulation with one-point upstream scheme.

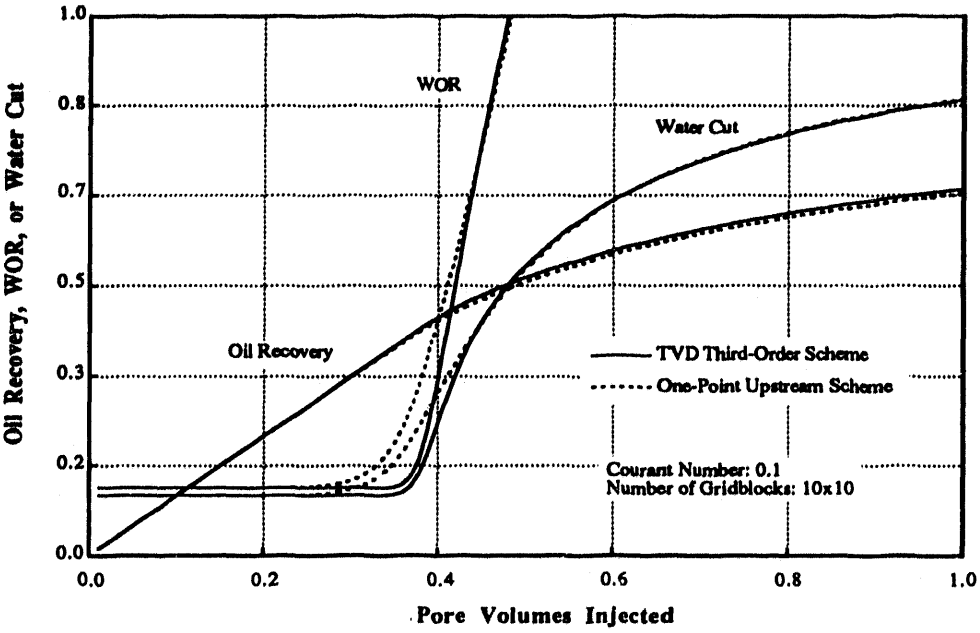

Fig. 26 Simulation results of a two-dimensional waterflood using the fully implicit formulation with the TVD high-order scheme or one-point.

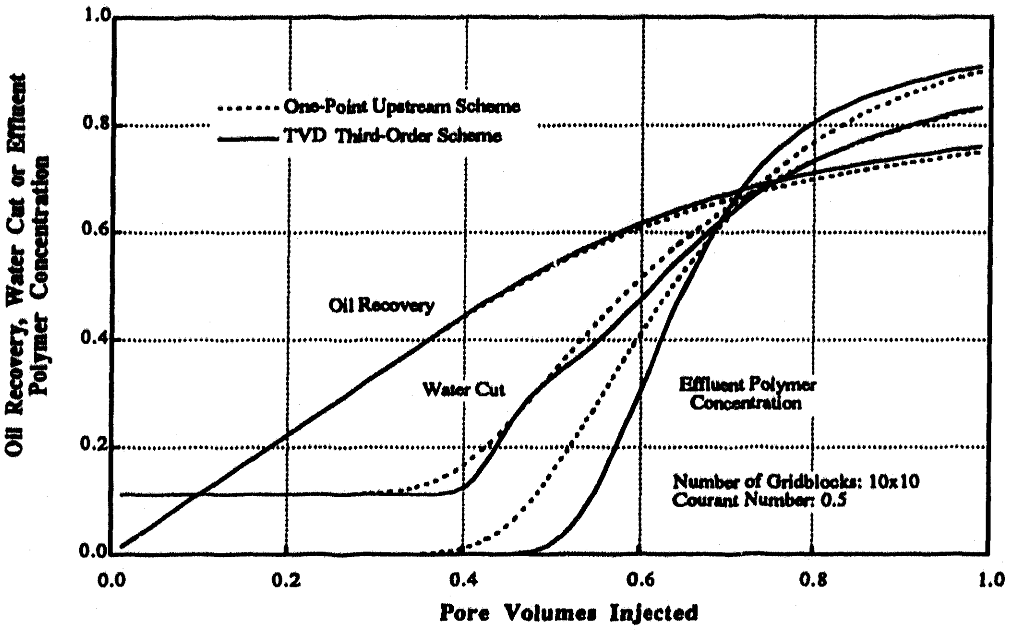

Fig. 27 Simulation results of a two-dimensional polymerflood in a homogeneous five-spot pattern using the fully implicit formulation.

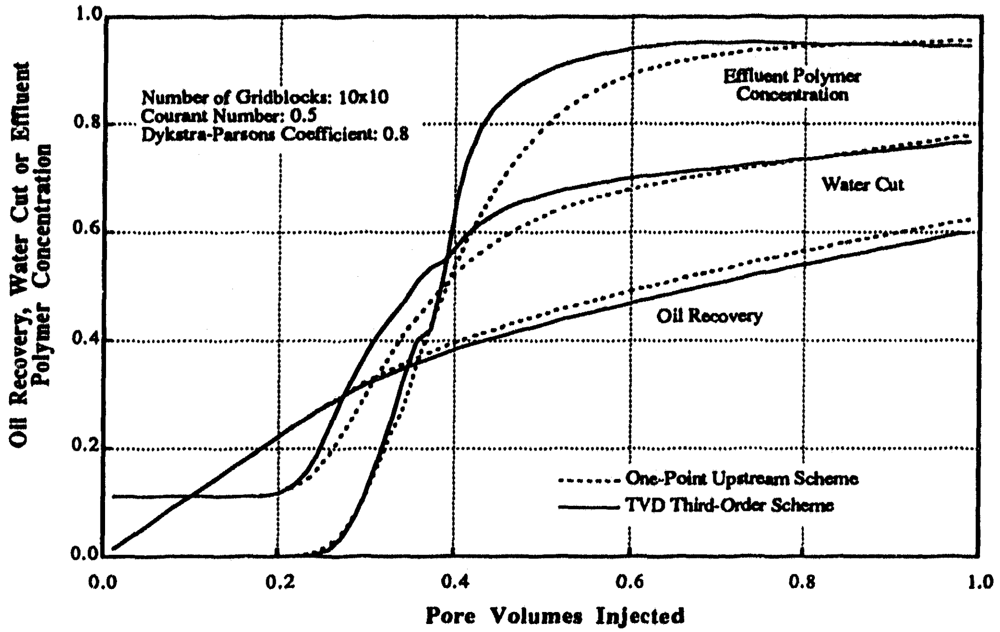

Fig. 28 Simulation results of a two-dimensional polymerflood in a heterogeneous five-spot pattern using the fully implicit formulation.

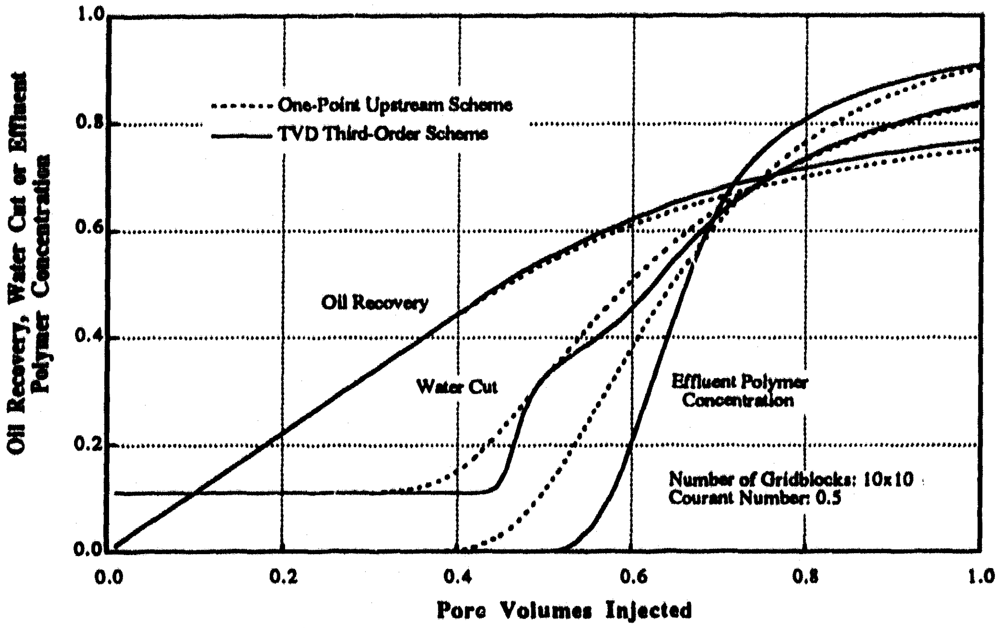

Fig. 29 Simulation results of a two-dimensional polymerflood in a homogeneous five-spot pattern using the IMPES formulation.

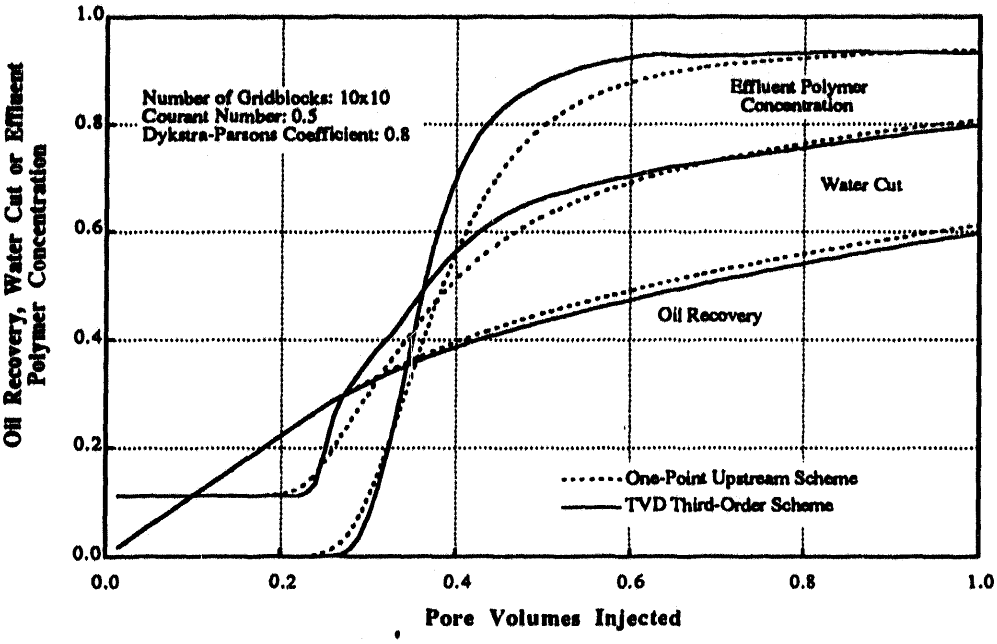

Fig. 30 Simulation results of a two-dimensional polymerflood in a heterogeneous five-spot pattern using the IMPES formulation.

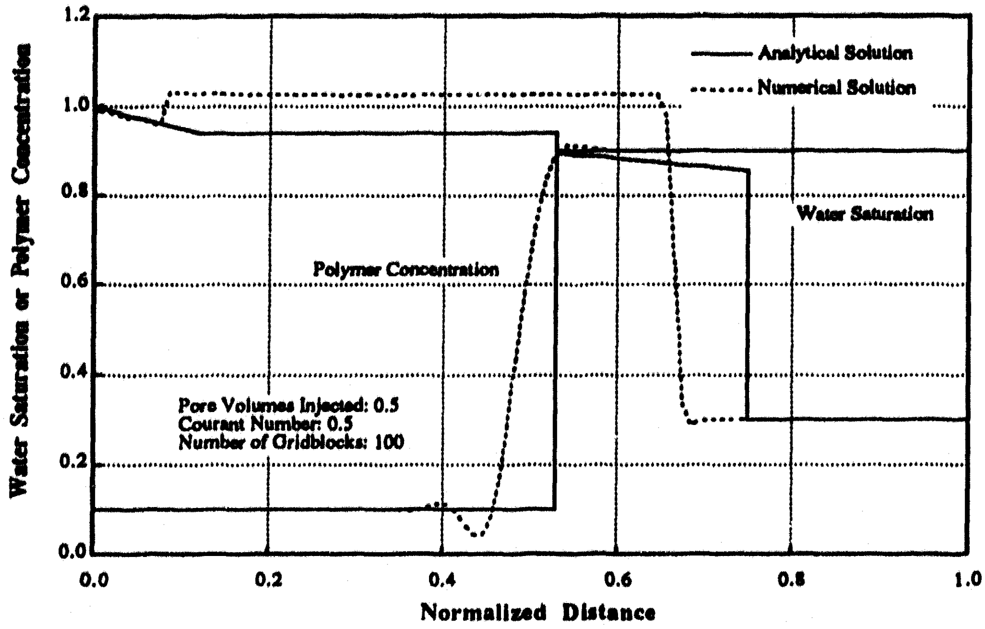

Fig. 31 Profiles of simulating Holing's one-dimensional polymerflood problem using the fully implicit formulation with the high-order scheme without TVD flux-limiting.

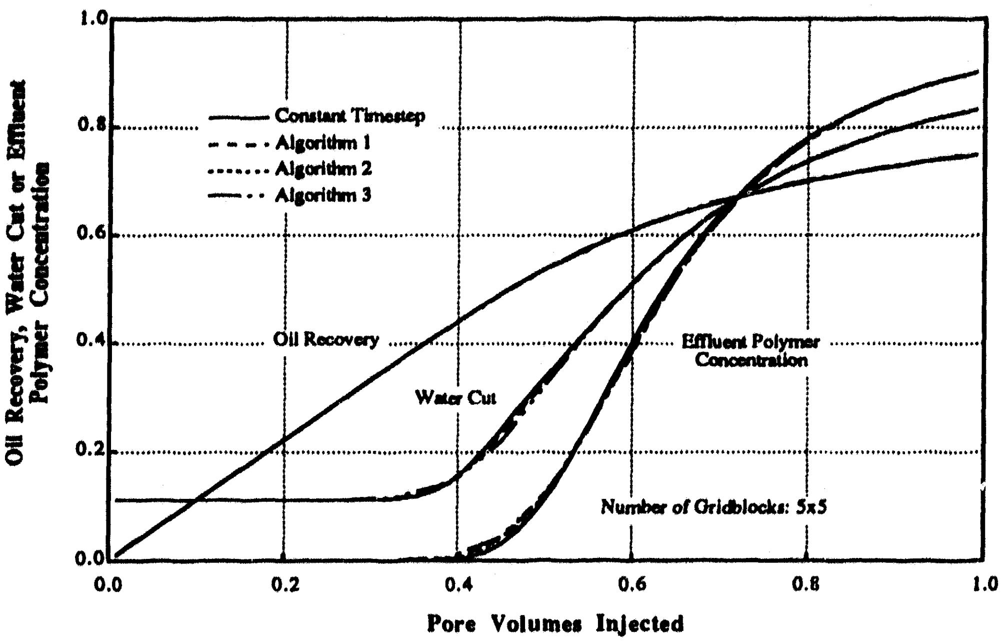

Fig. 32 Simulation results of a two-dimensional polymerflood using the fully implicit formulation with the TVD high-order scheme and different timestepping algorithms.

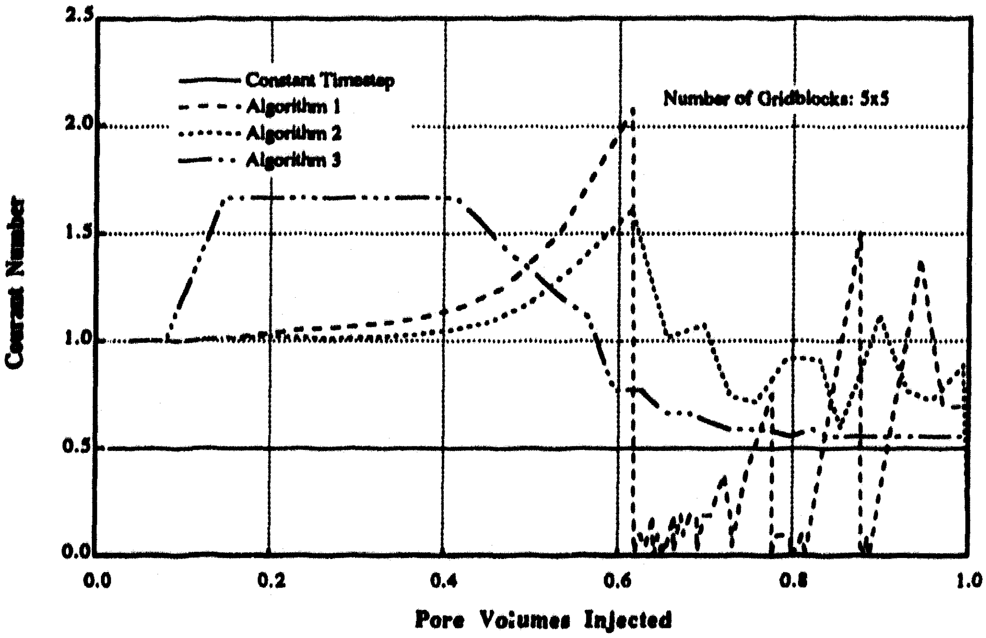

Fig. 33 Courant numbers for simulating a two-dimensional polymerflood using the fully implicit formulation with the TVD high-order scheme and different timestepping algorithms.

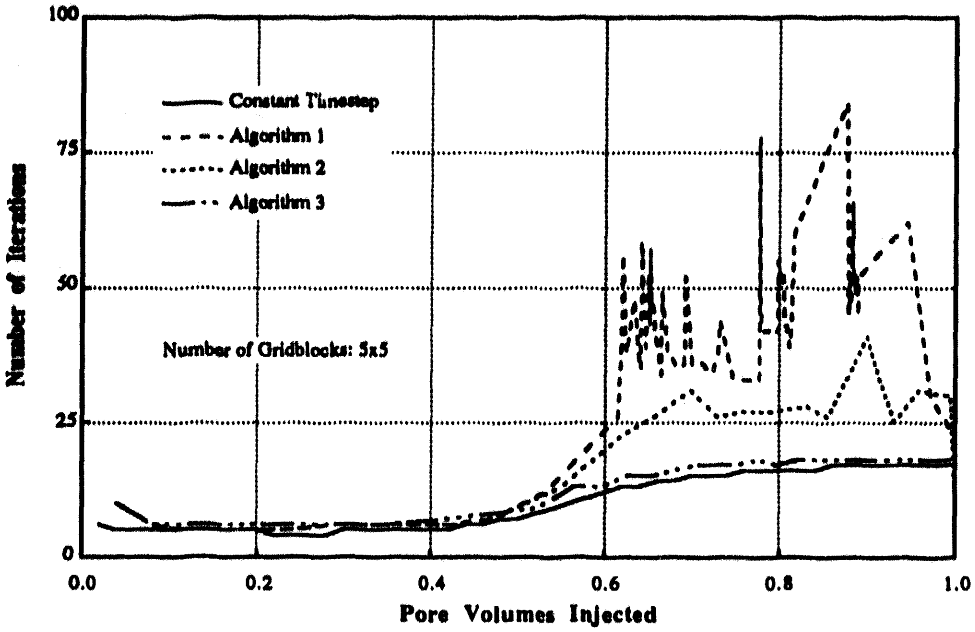

Fig. 34 Number of iterations for simulating a two-dimensional polymerflood using the fully implicit formulation with the TVD high-order scheme and different timestepping algorithms.

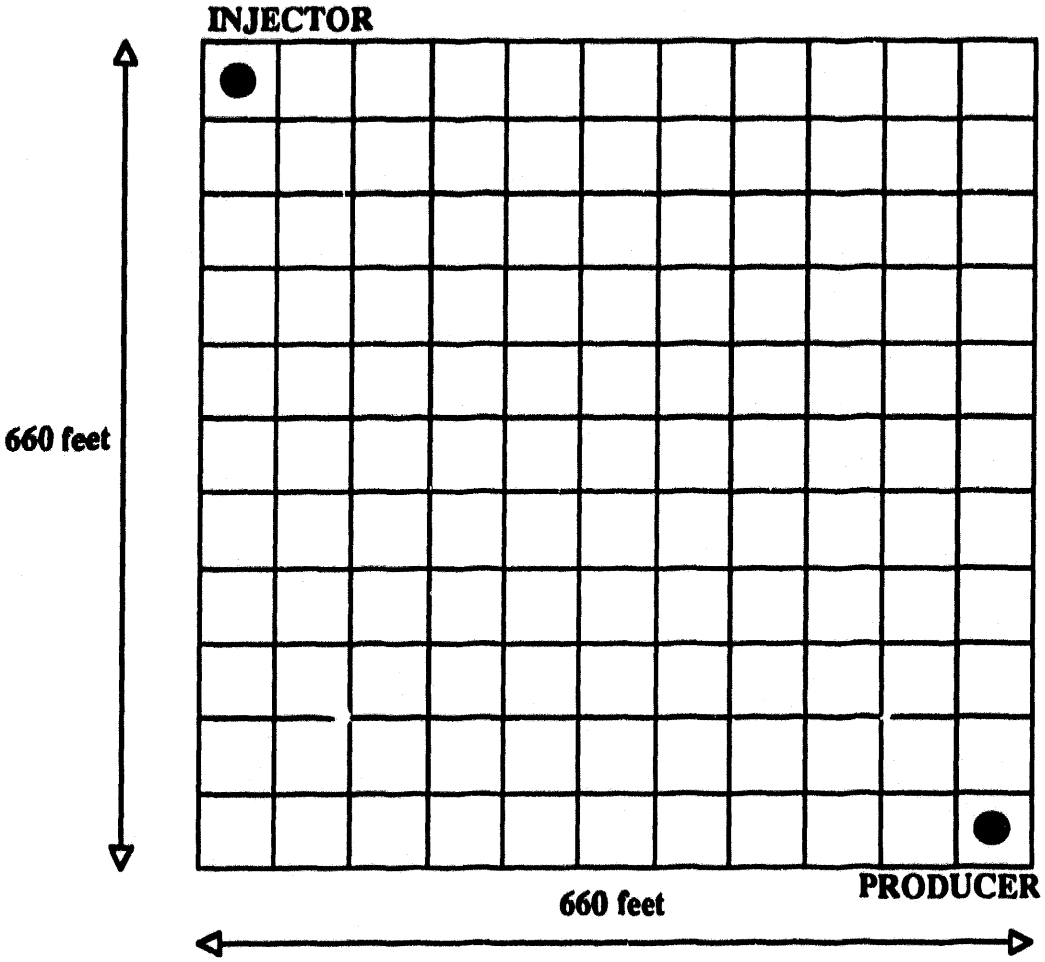

Fig. 35 Aerial view of the quarter five-spot grid and well location

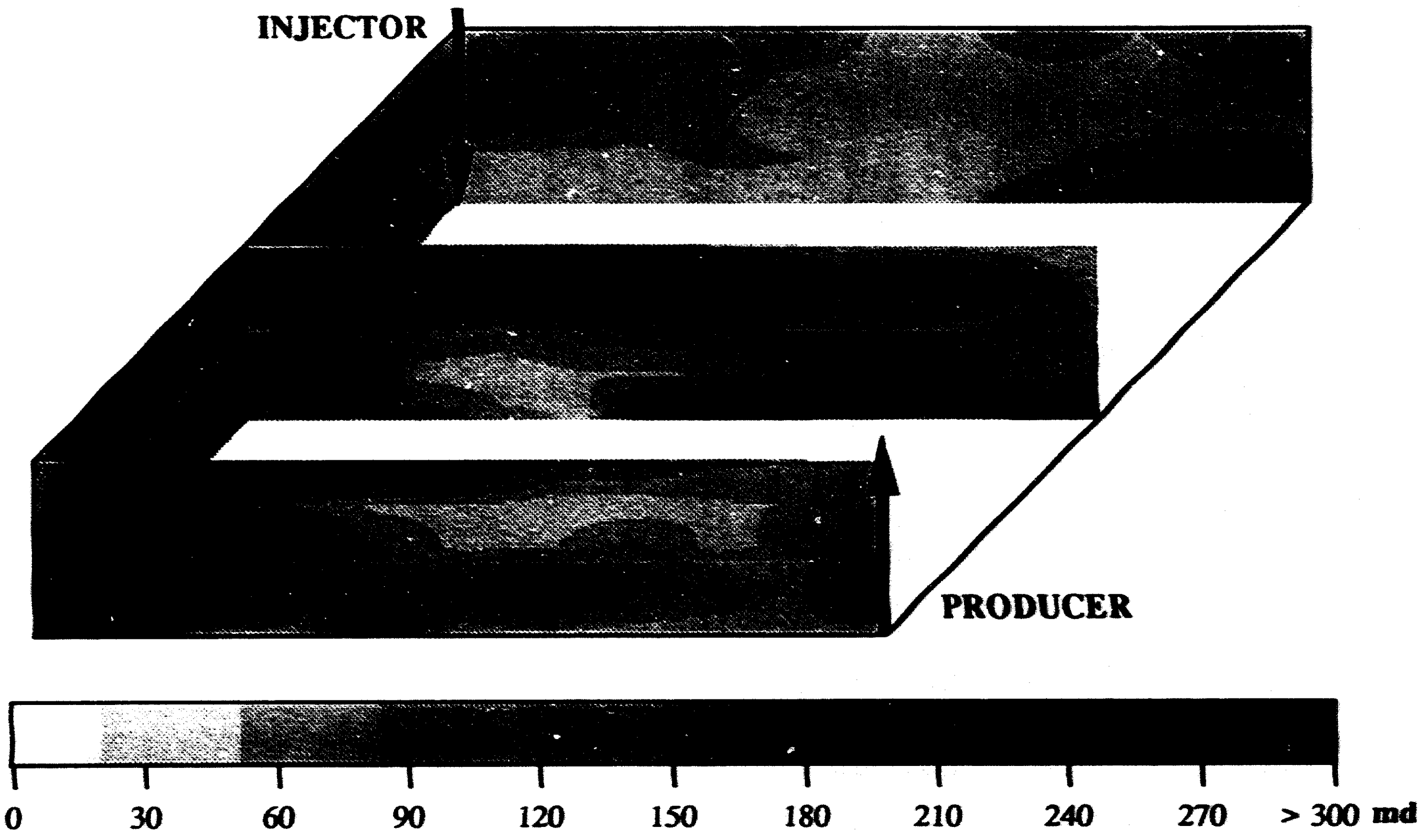

Fig. 36 Permeability field for the case of correlation length of 660 feet in x and y direction, 28 feet in the z direction, and V_{DP} of 0.8 (Base Case)

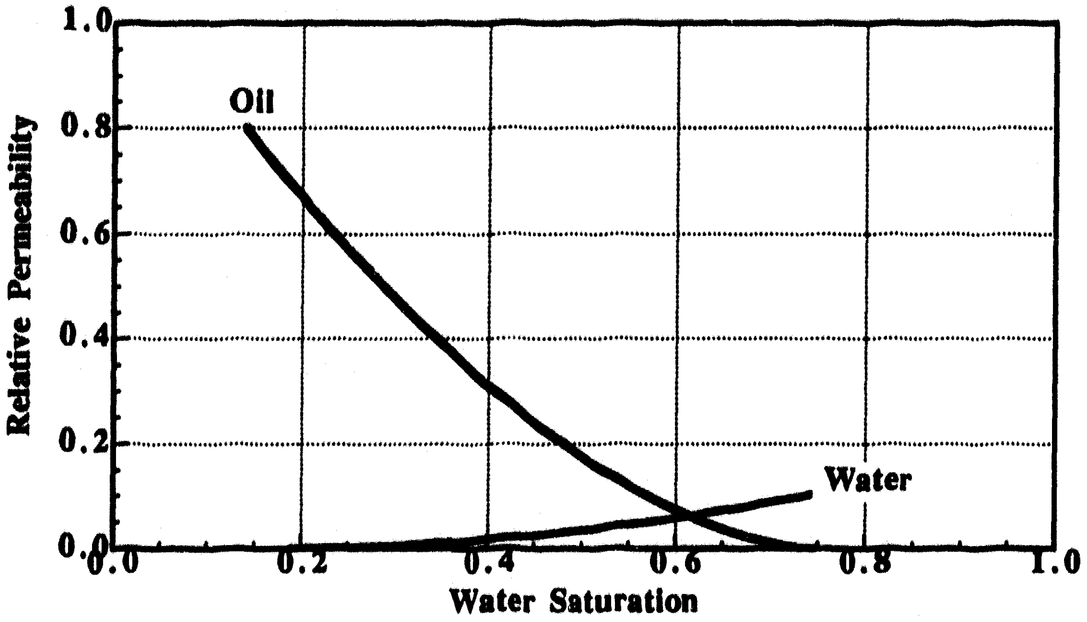

Fig. 37 Oil and water relative permeability curves for low capillary number

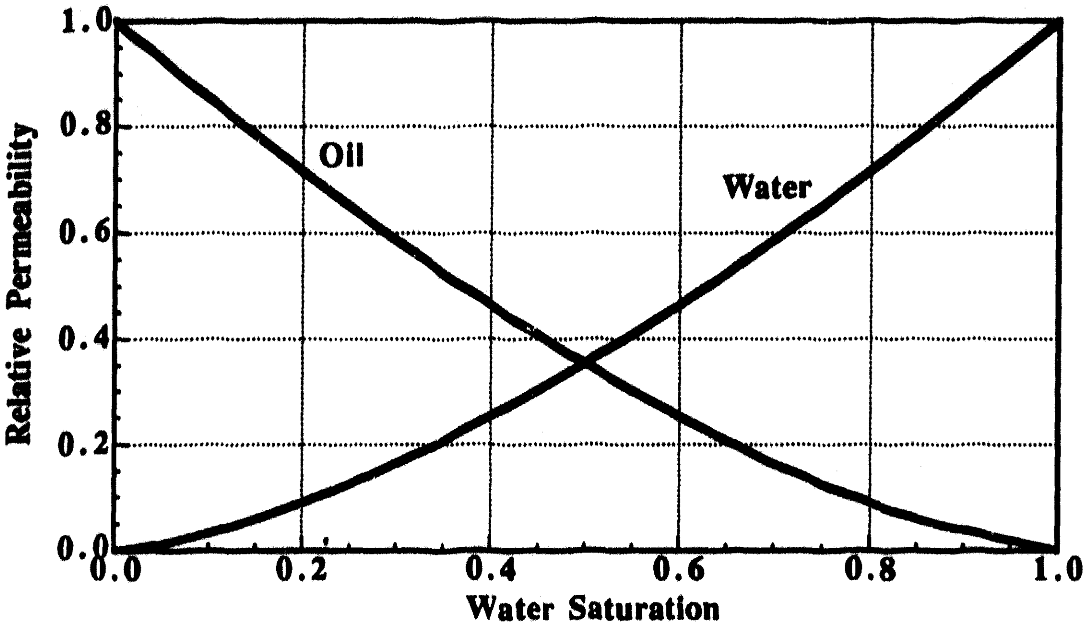

Fig. 38 Oil and water relative permeability curves at high capillary number

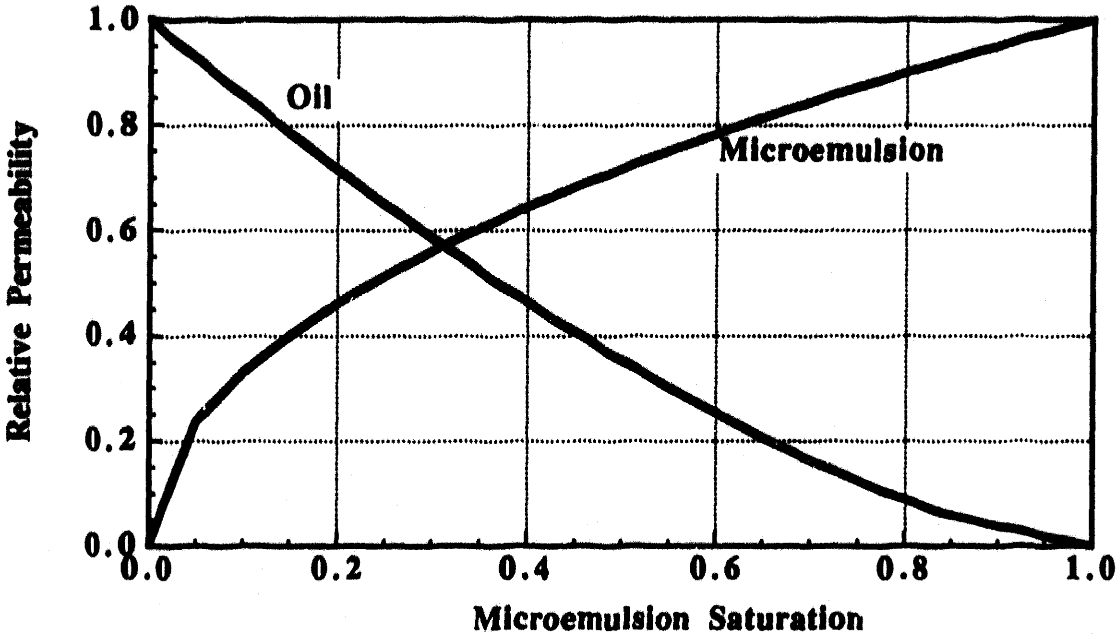

Fig. 39 Oil and micro emulsion relative permeability curves at high capillary number

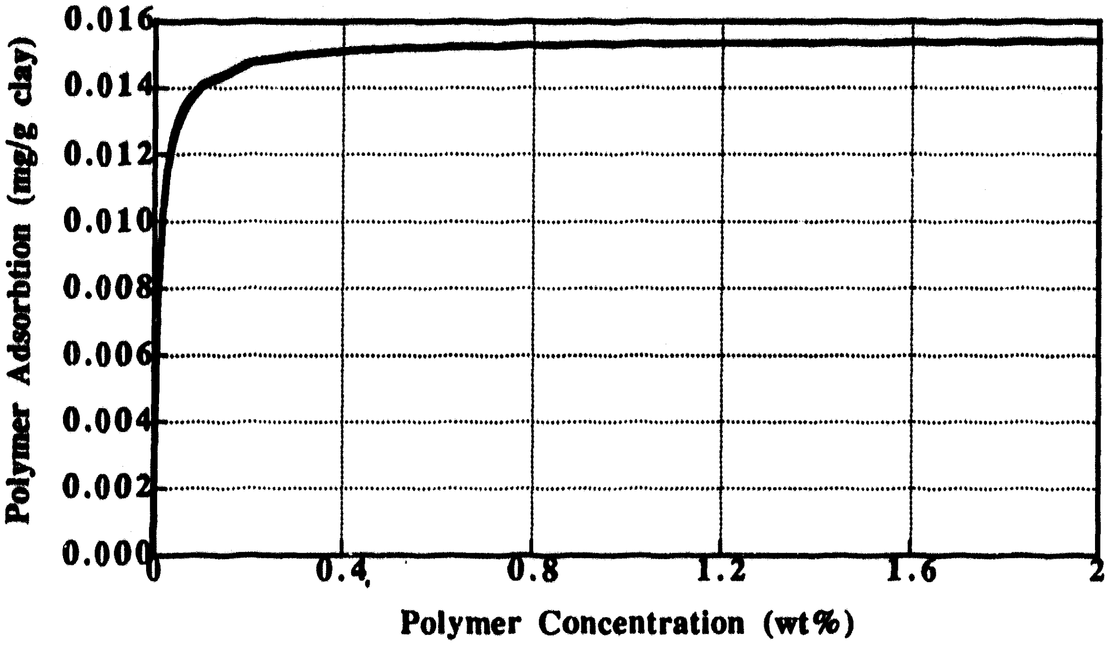

Fig. 40 Polymer adsorption as a function of polymer concentration

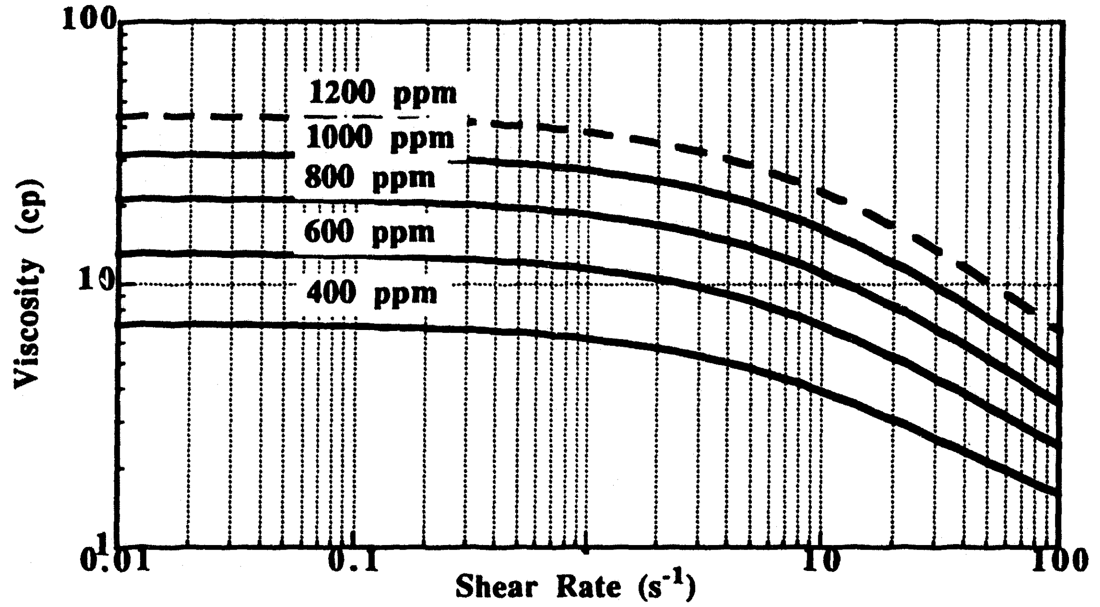

Fig. 41 Polymer viscosity as a function of polymer concentration and shear rate

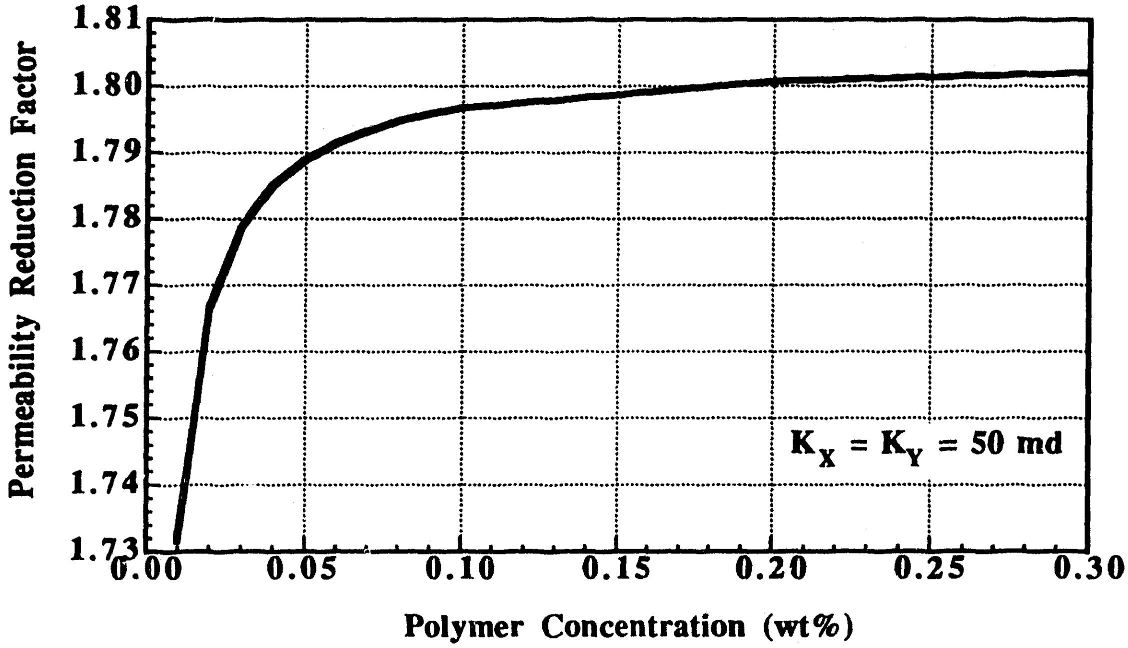

Fig. 42 Polymer permeability reduction factor

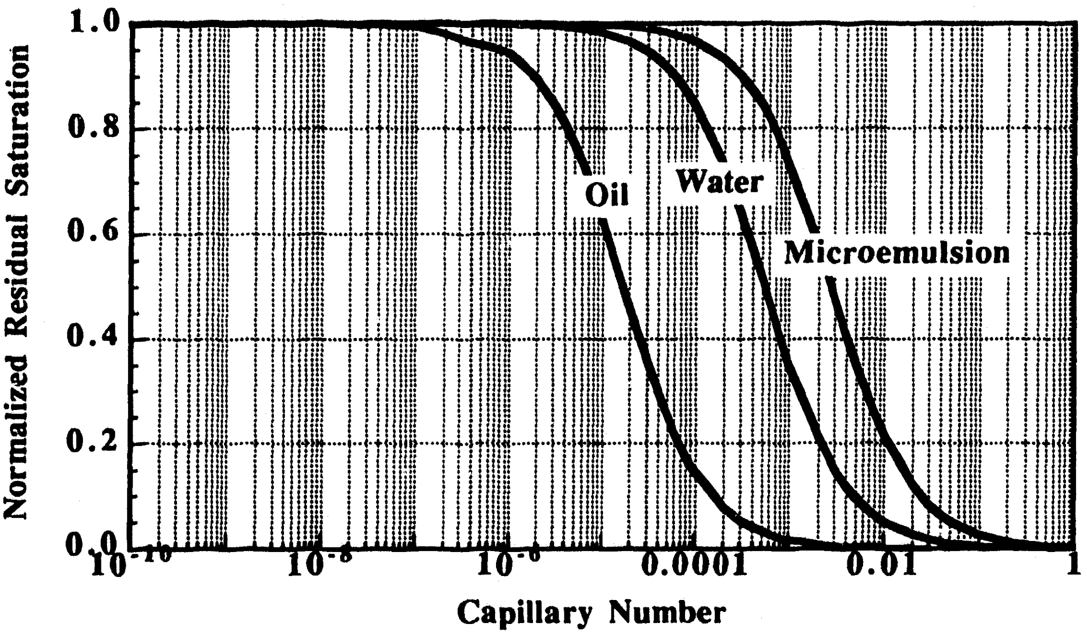

Fig. 43 Capillary desaturation curves for oil, water, and micro emulsion phases

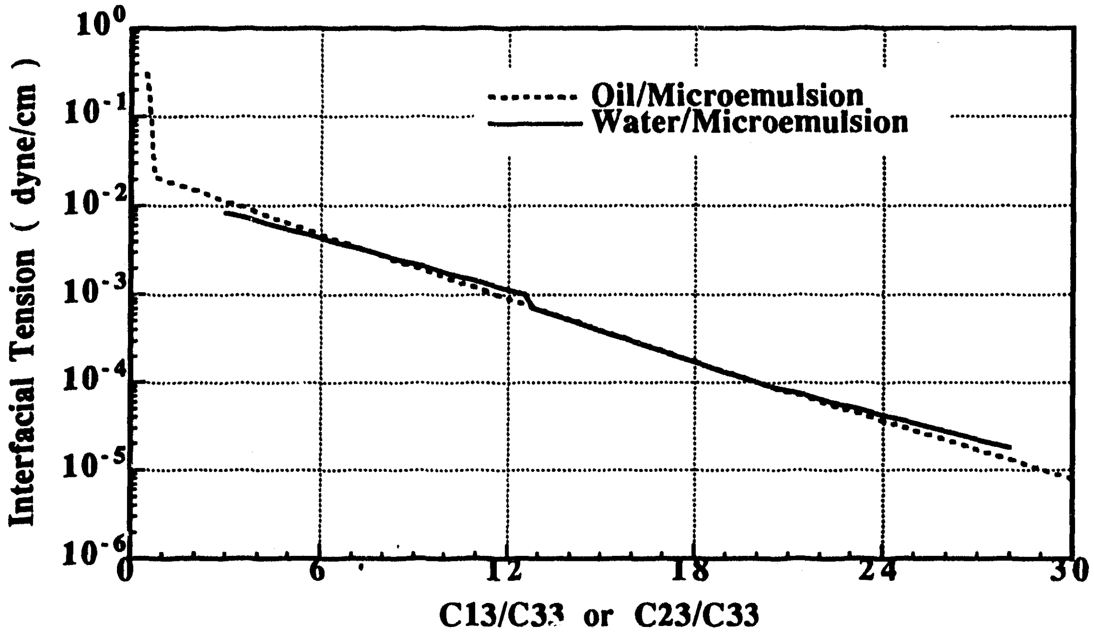

Fig. 44 Interfacial tension as a function of solubilization ratios

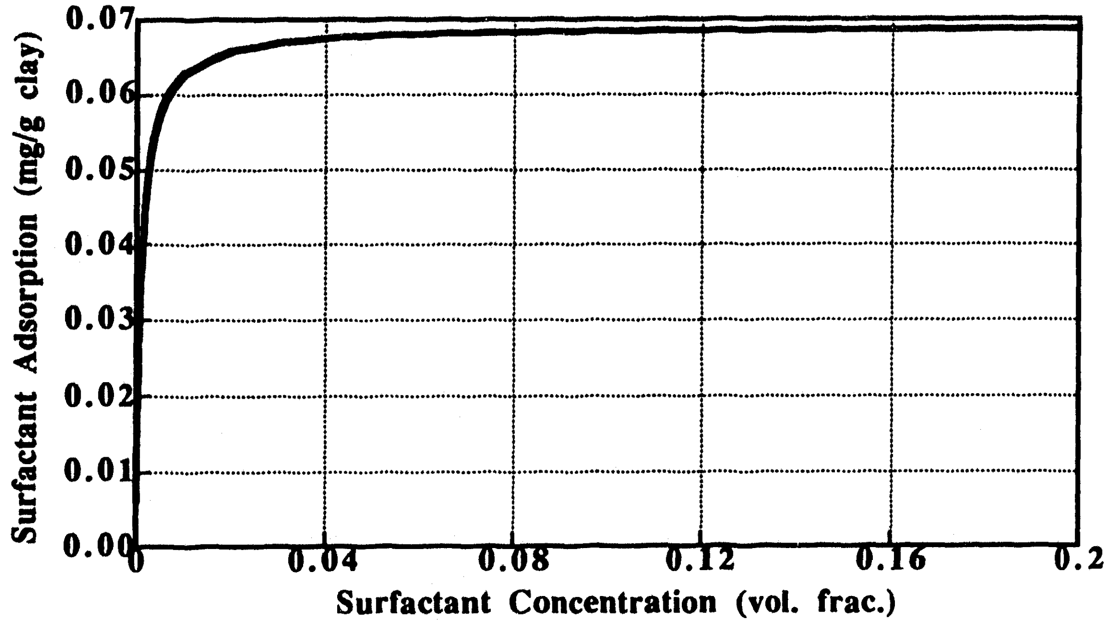

Fig. 45 Adsorbed surfactant concentration as a function of surfactant concentration

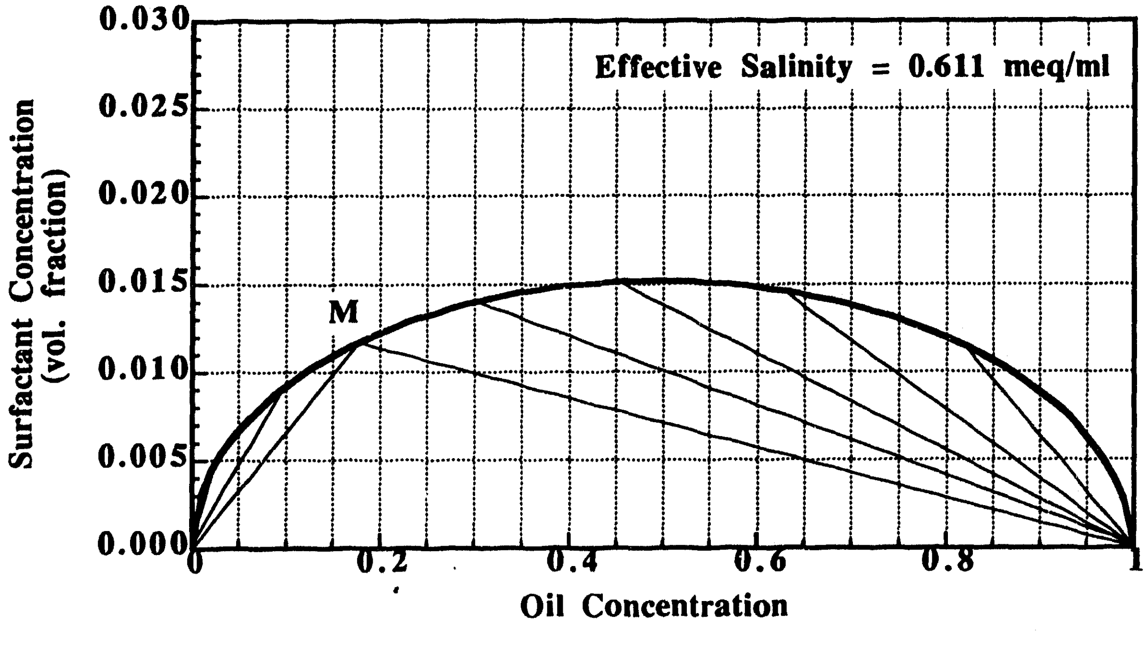

Fig. 46 Phase behavior for the type III region

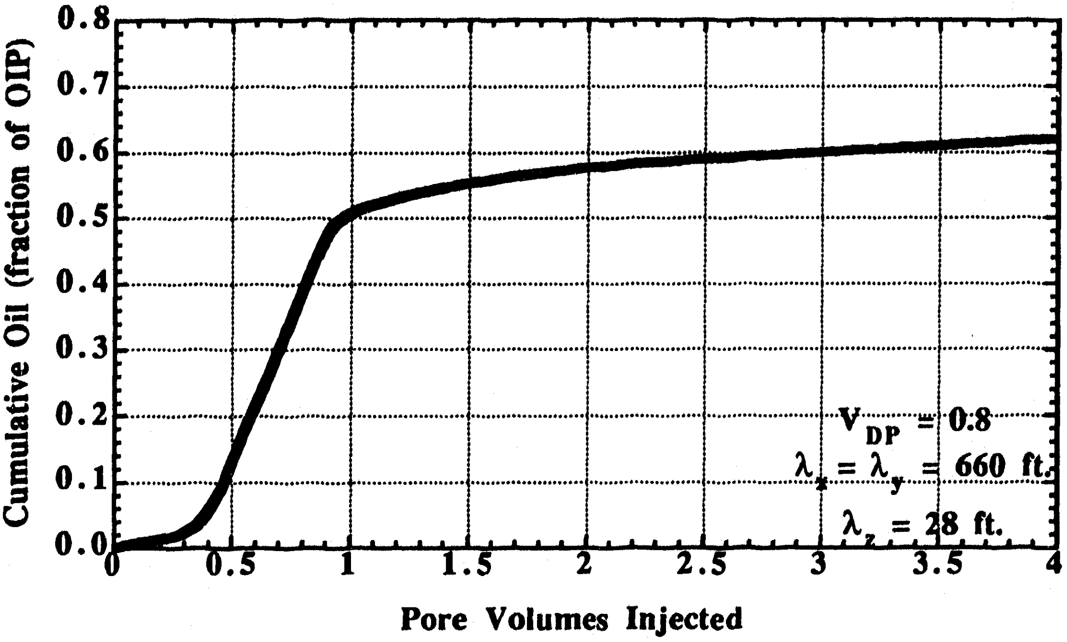

Fig. 47 Cumulative oil recovered as a function of pore volumes injected (base case)

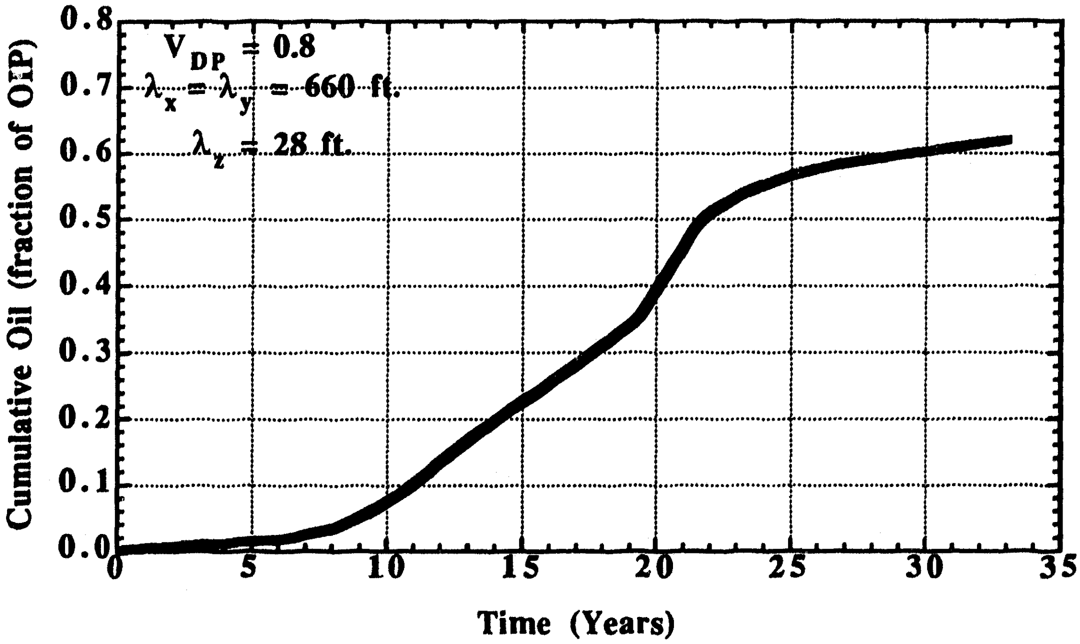

Fig. 48 Cumulative oil recovered as a function of time (base case)

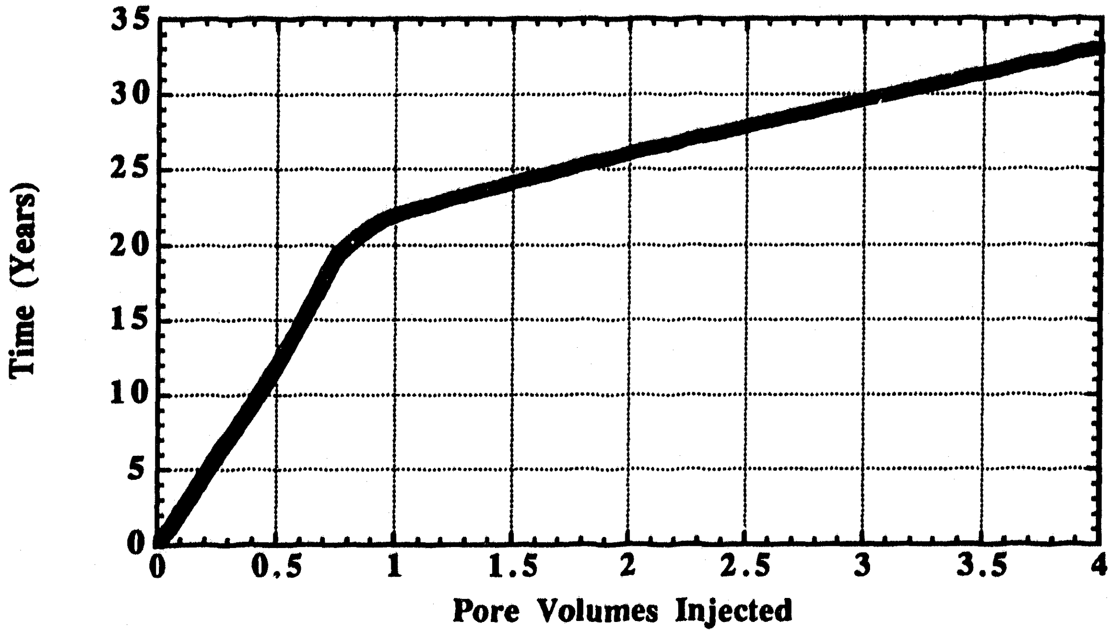

Fig. 49 Time versus pore volumes injected

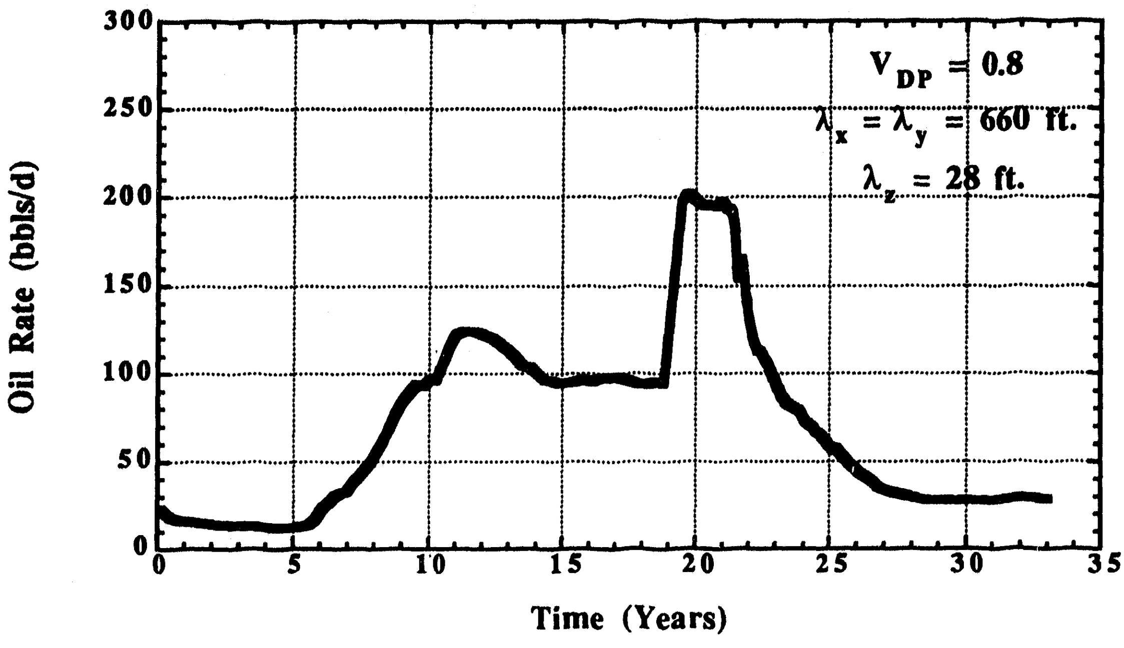

Fig. 50 Oil production rate versus time (base case)

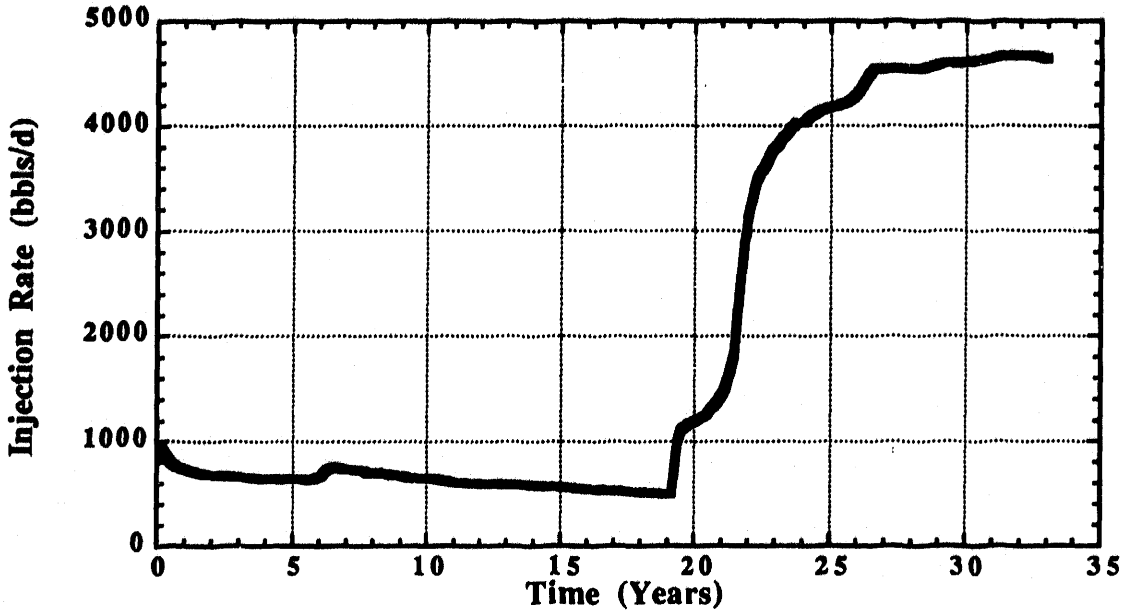

Fig. 51 Total injection rate as a function of time (base case)

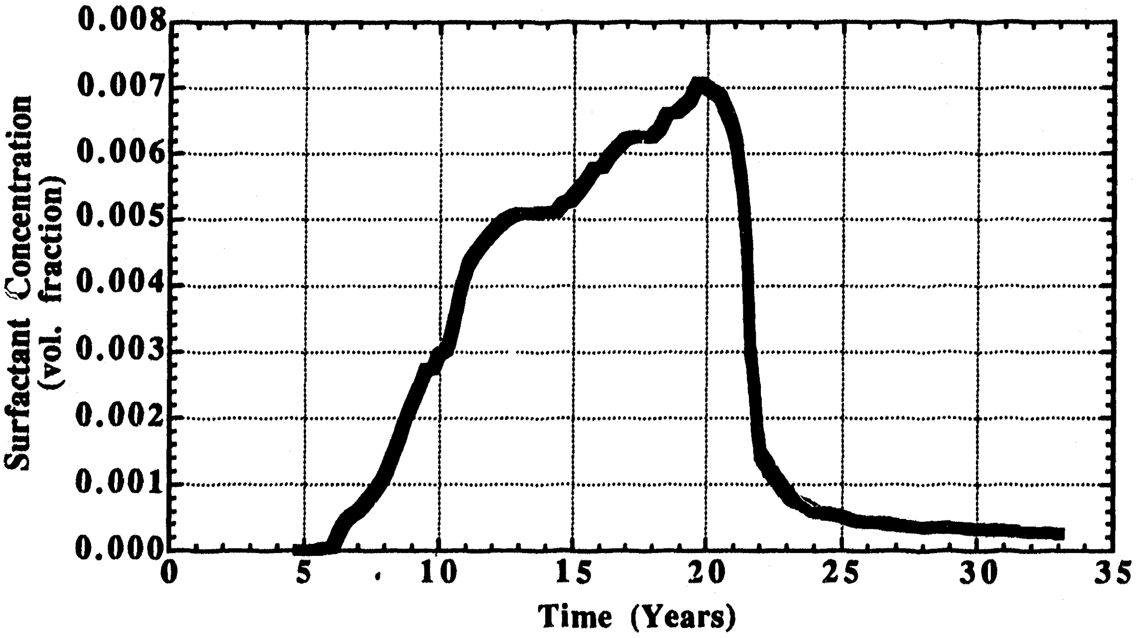

Fig. 52 History of effluent surfactant concentration (base case)

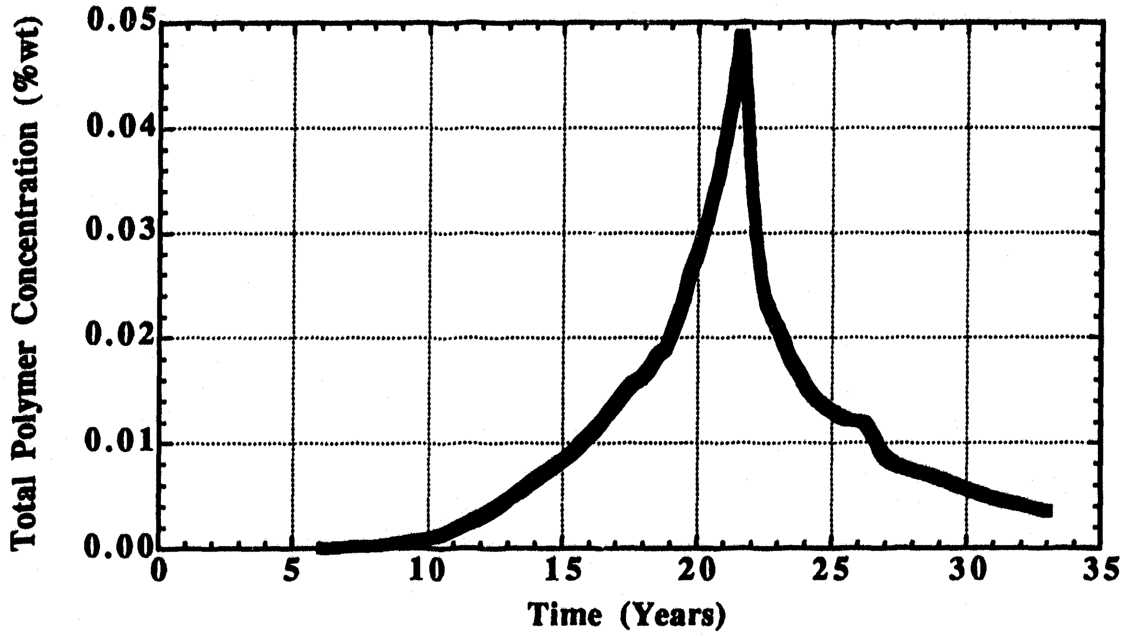

Fig. 53 History of effluent polymer concentration (base case)

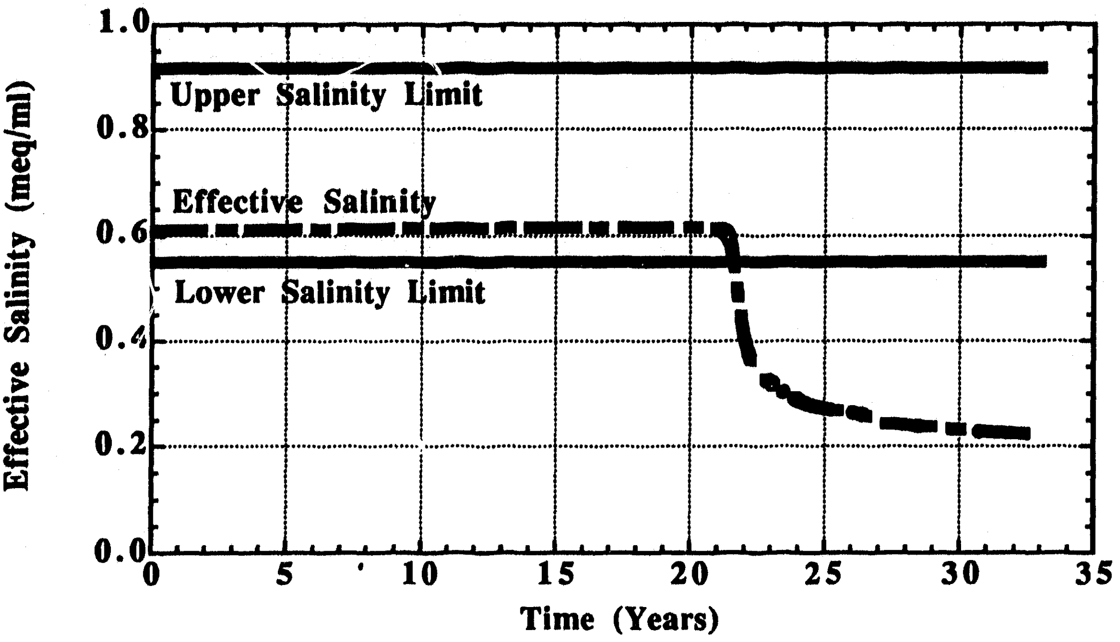

Fig. 54 History of effective salinity for the base case

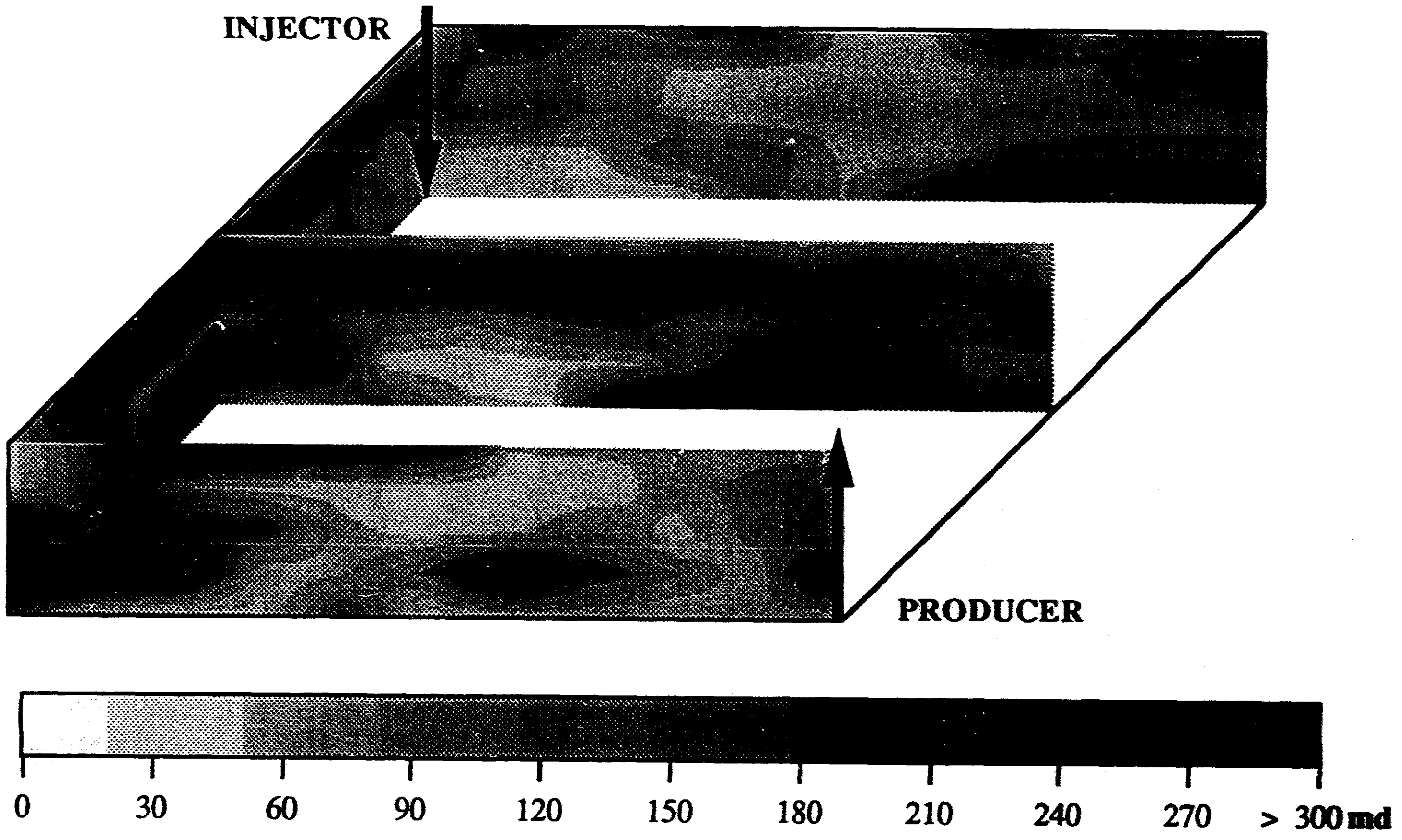

Fig. 55 Permeability field for the case of correlation length of 330 feet in the x and y direction, and 28 feet in the z direction (Realization #1)

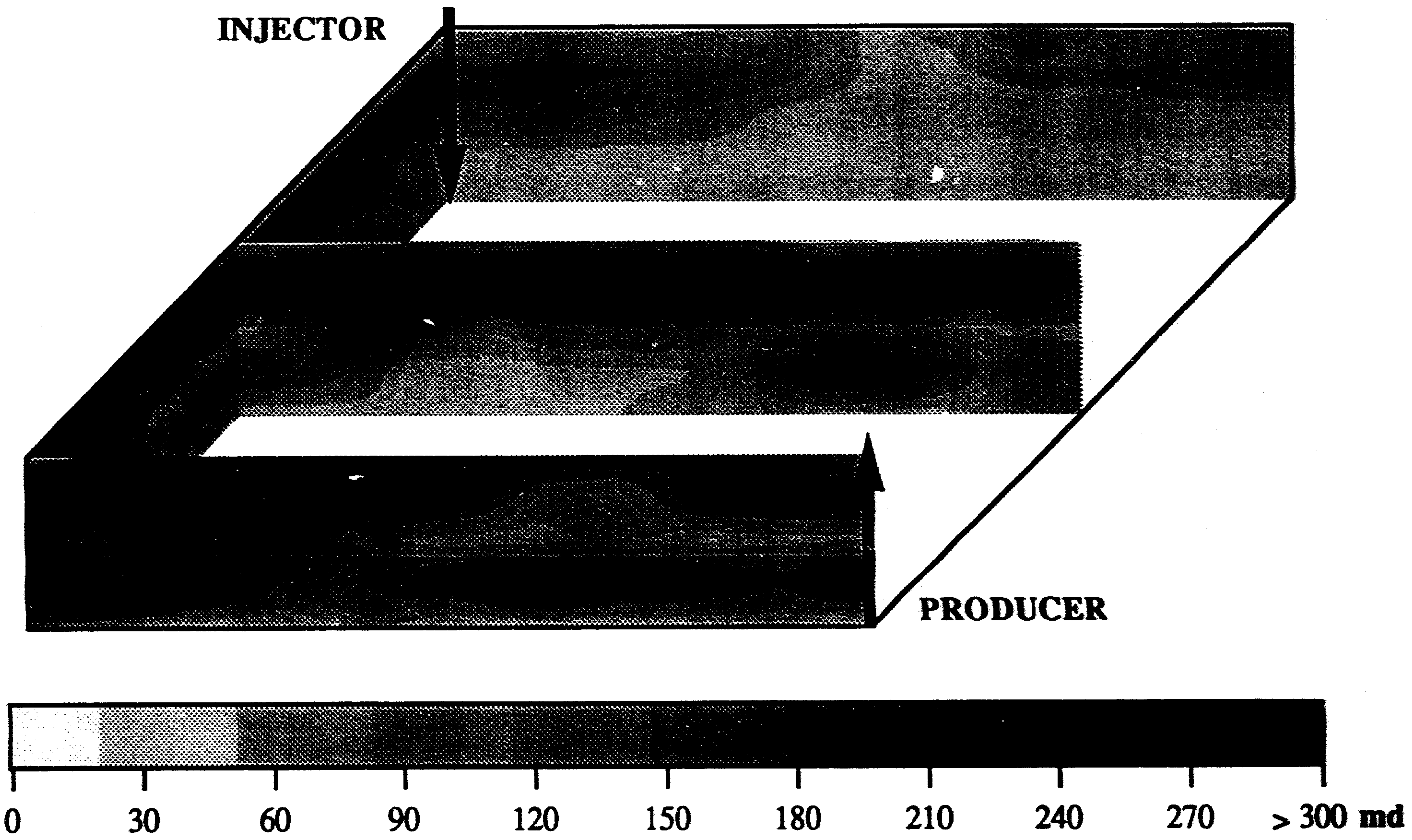

Fig. 56 Permeability field for the case of correlation length of 2,640 feet in the x and y direction, and 28 feet in the z direction (Realization #1)

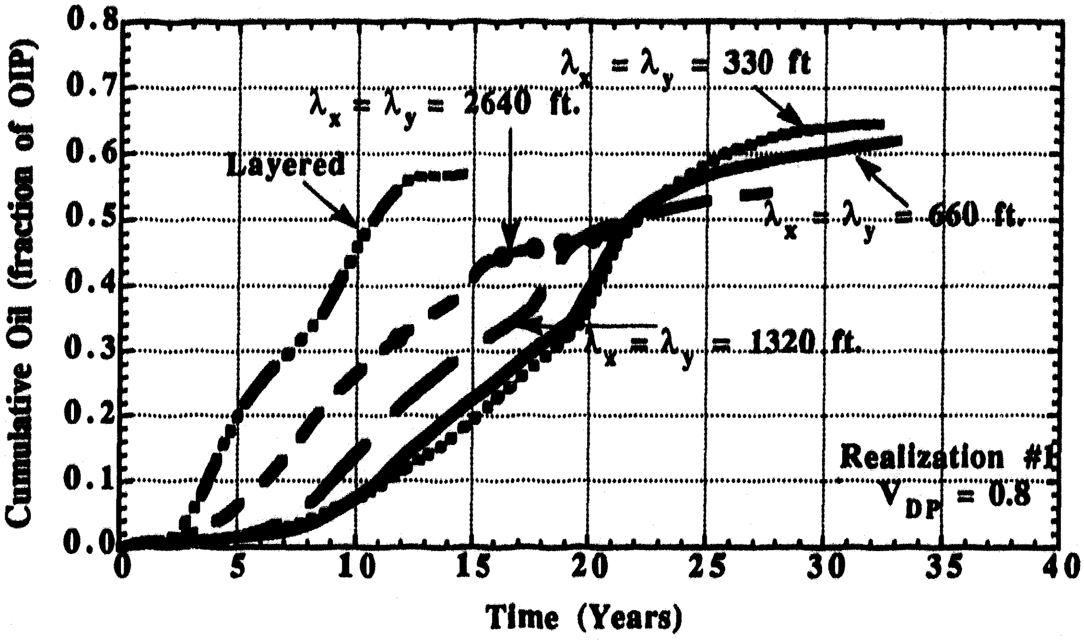

Fig. 57 Comparison between oil recovery for layered and stochastic reservoir descriptions

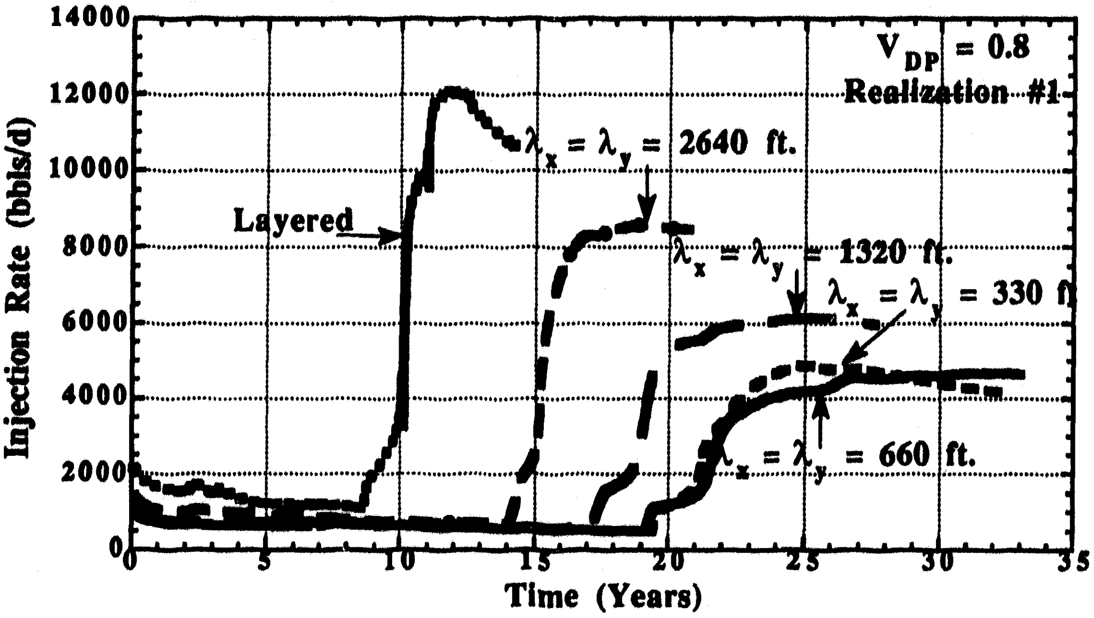

Fig. 58 Comparison of injection rate between different correlation lengths (Realization #1)

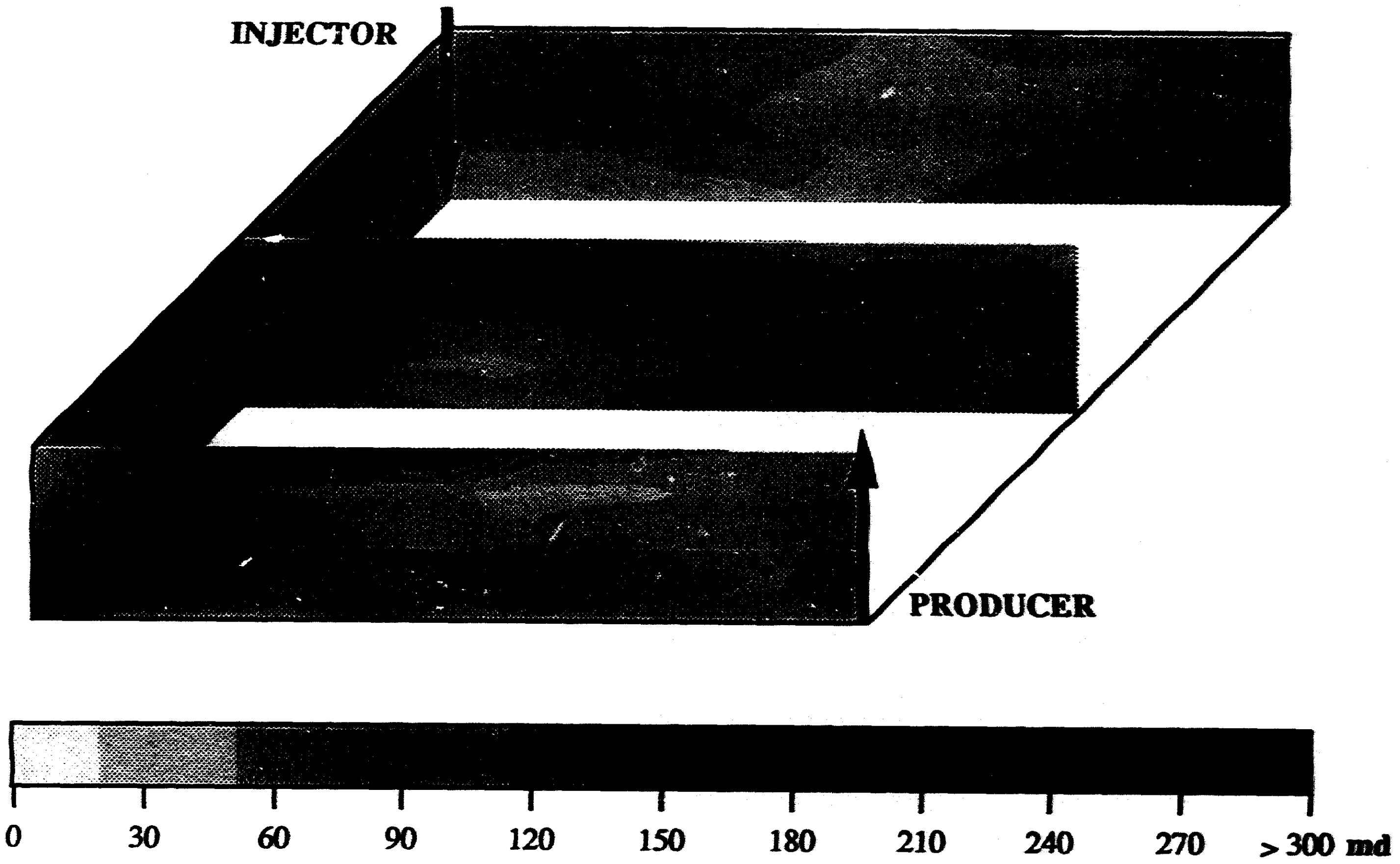

Fig. 59 Permeability field for the case of Dykstra-Parsons coefficient of 0.6 (Realization #1)

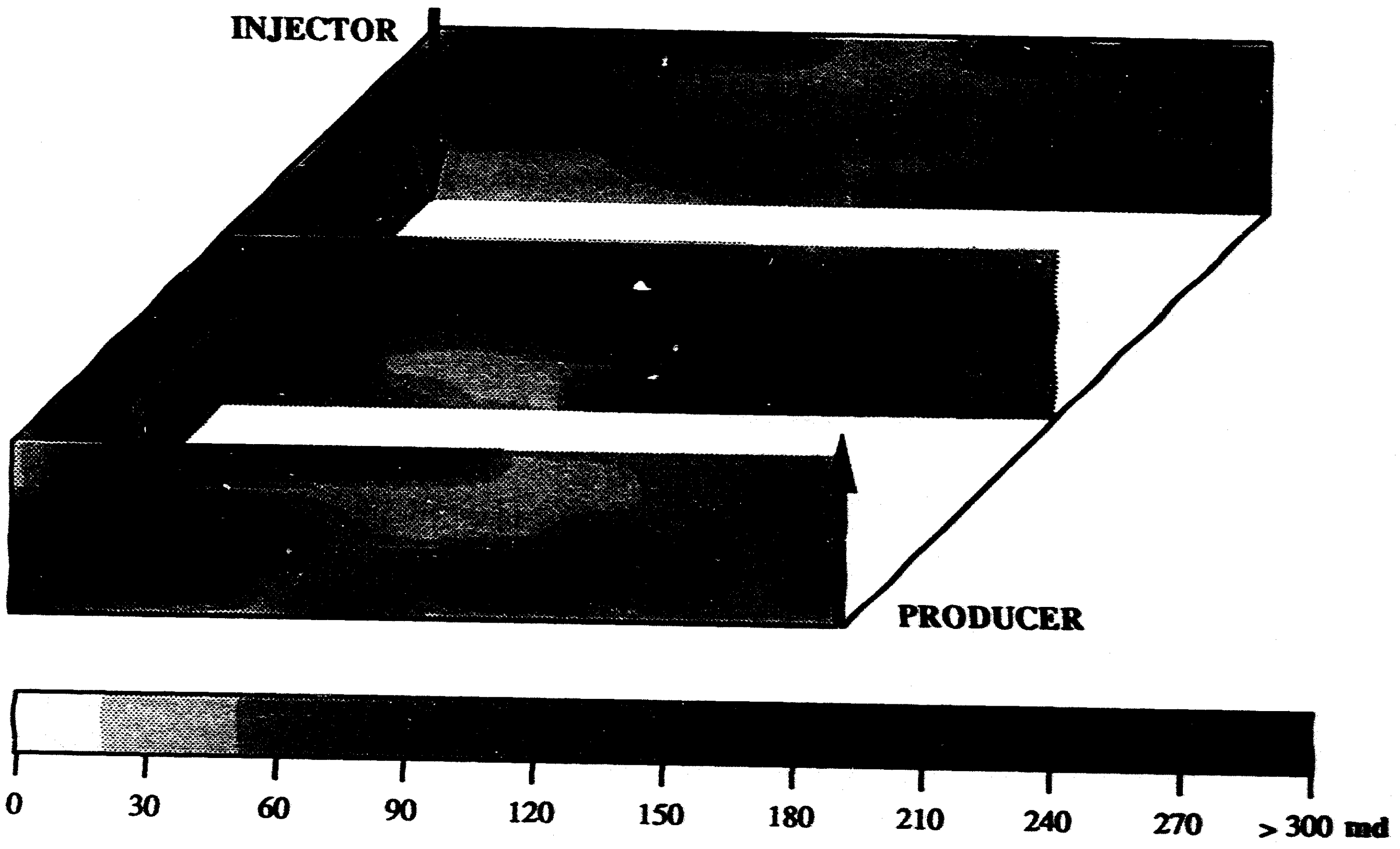

Fig. 60 Permeability field for the case of Dykstra-Parsons coefficient of 0.9 (Realization #1)

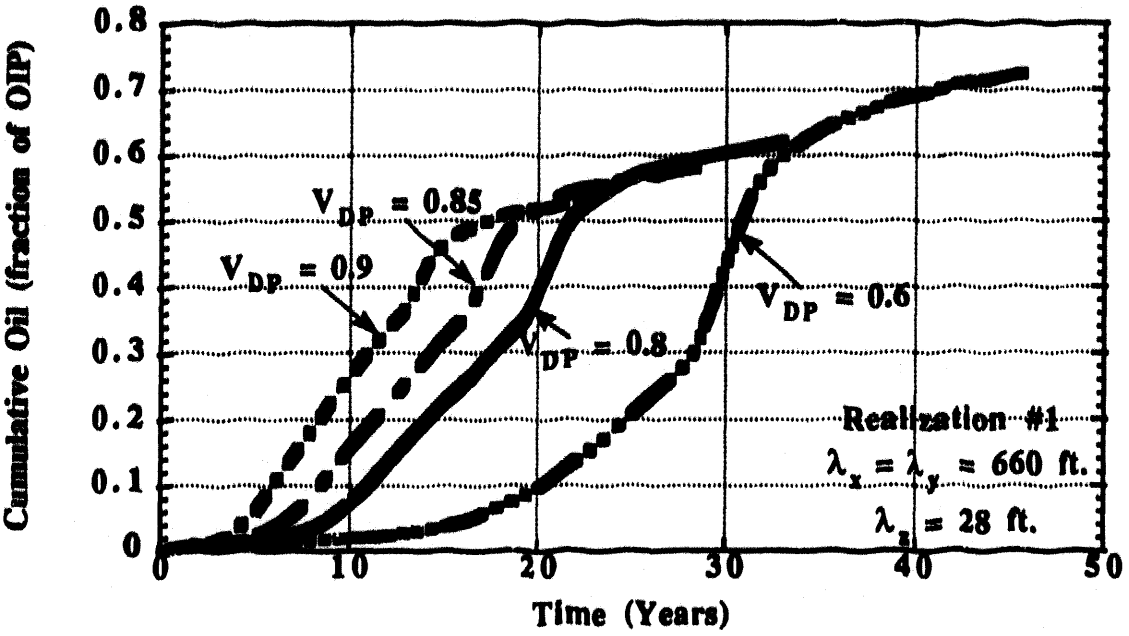

Fig. 61 Comparison between oil recovery for different degree of reservoir heterogeneity

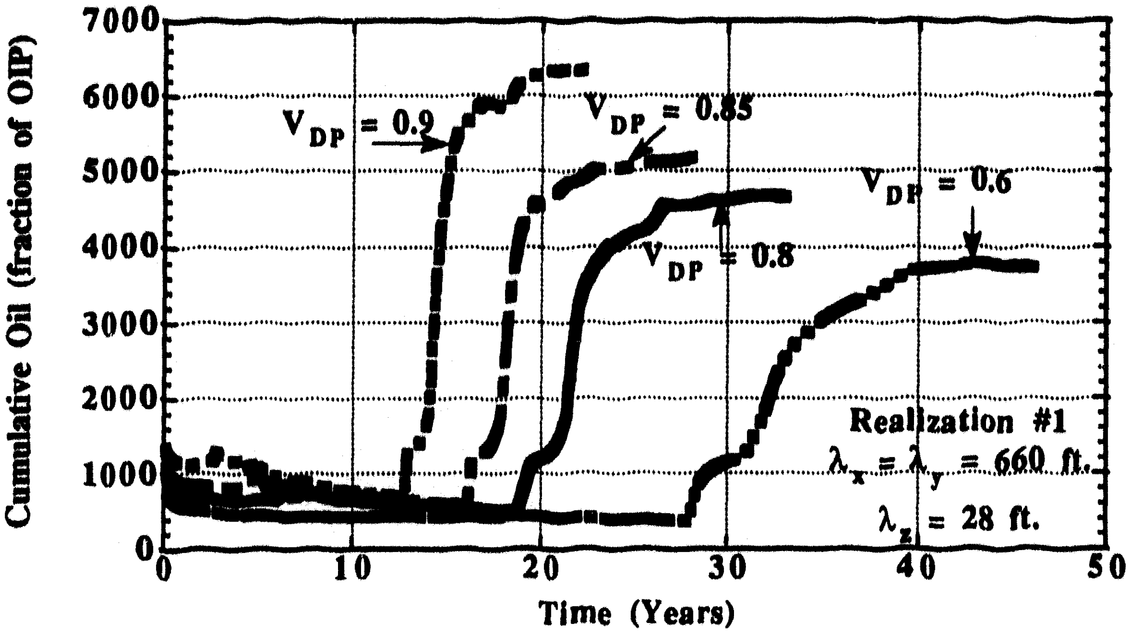

Fig. 62 Comparison of injection rate for different Dykstra-Parsons coefficient

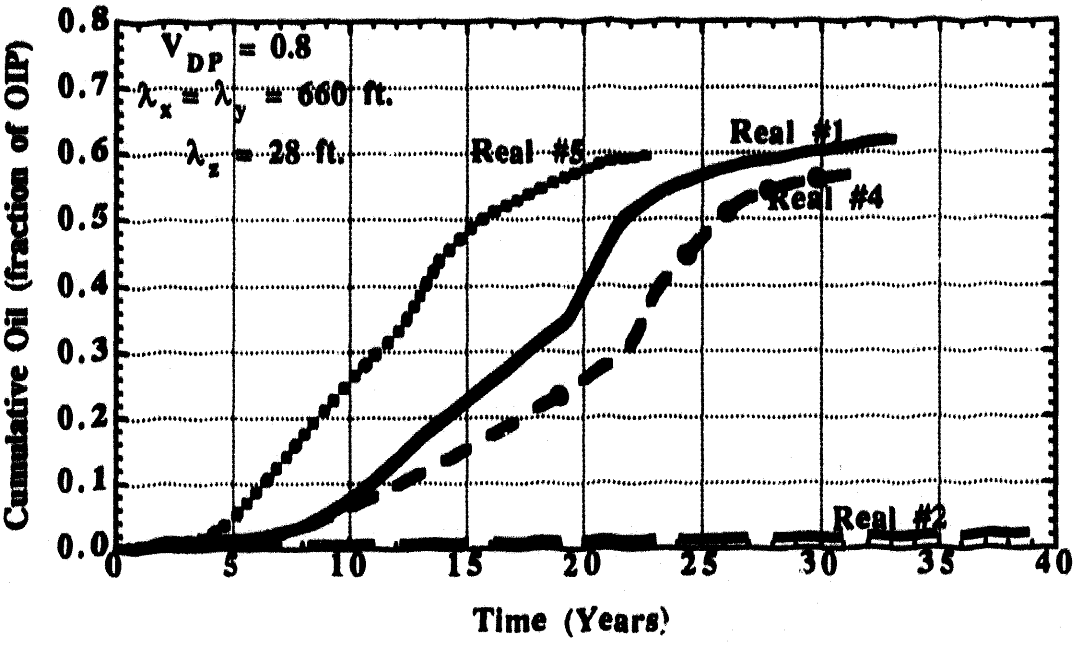

Fig. 63 Comparison between oil recovery for different realizations of the same permeability field

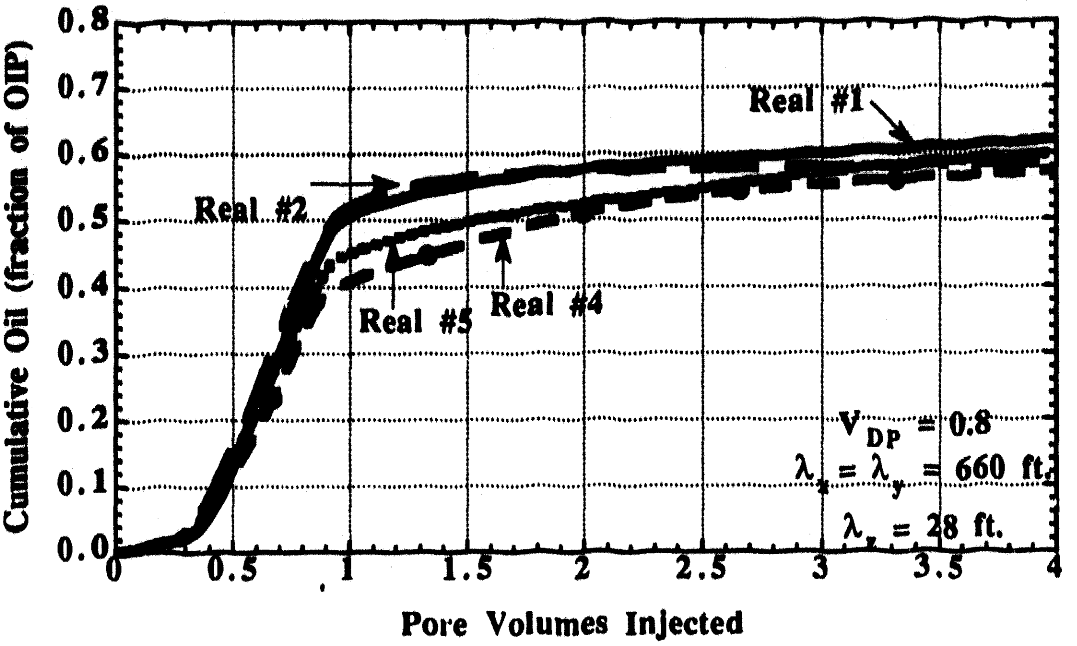

Fig. 64 Comparison between oil recovery for different realization of the same permeability field

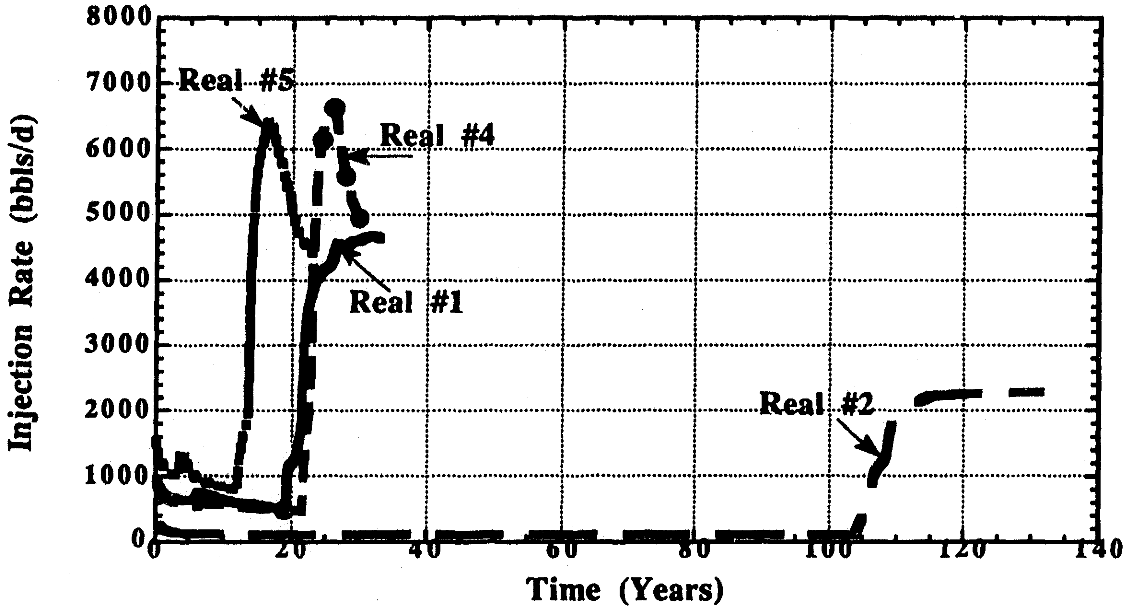

Fig. 65 Comparison of injection rate for different realizations of the base case permeability field

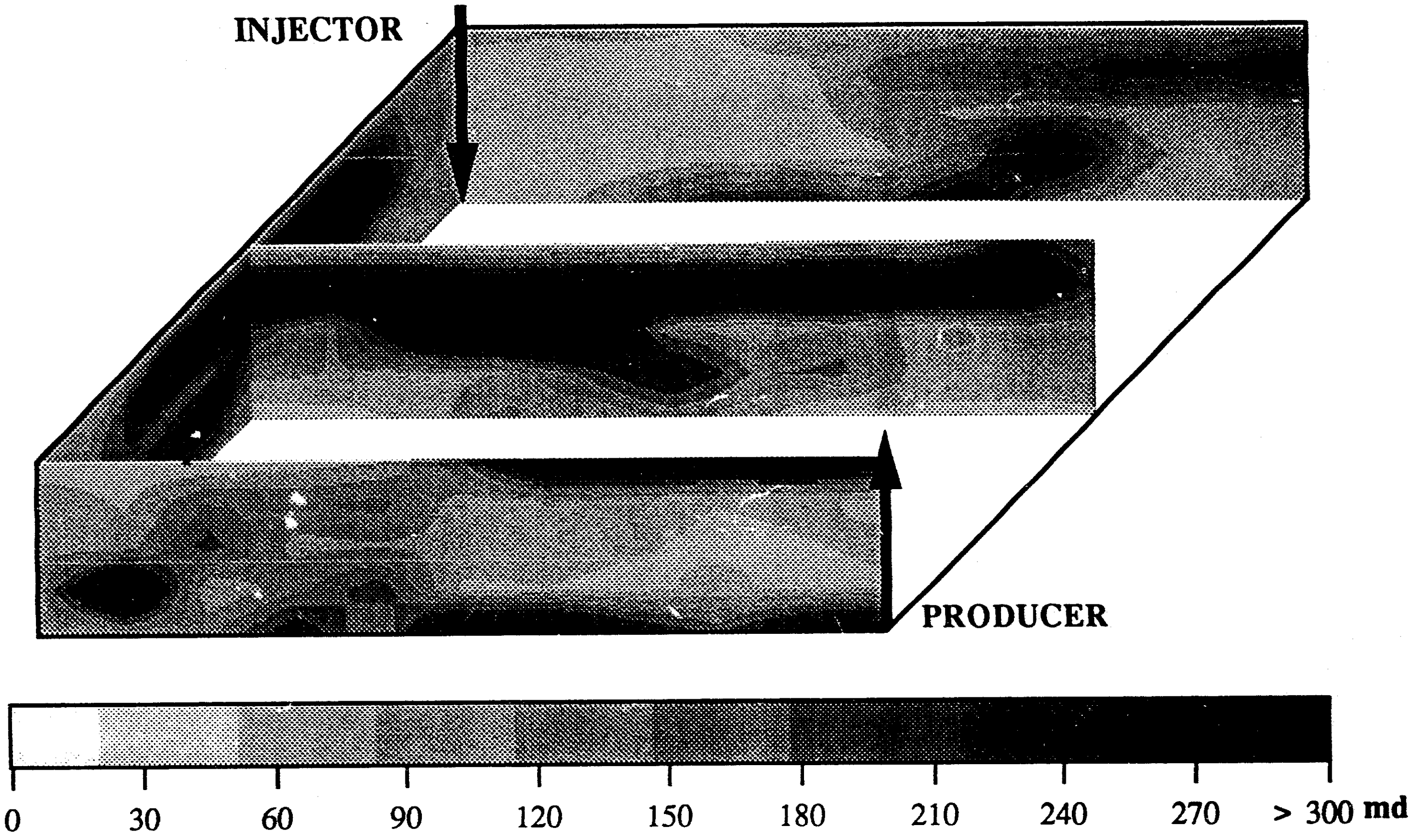

Fig. 66 Permeability field for the case of correlation length of 660 feet in x and y direction, 28 feet in z direction, and V_{DP} of 0.8 (Realization #2)

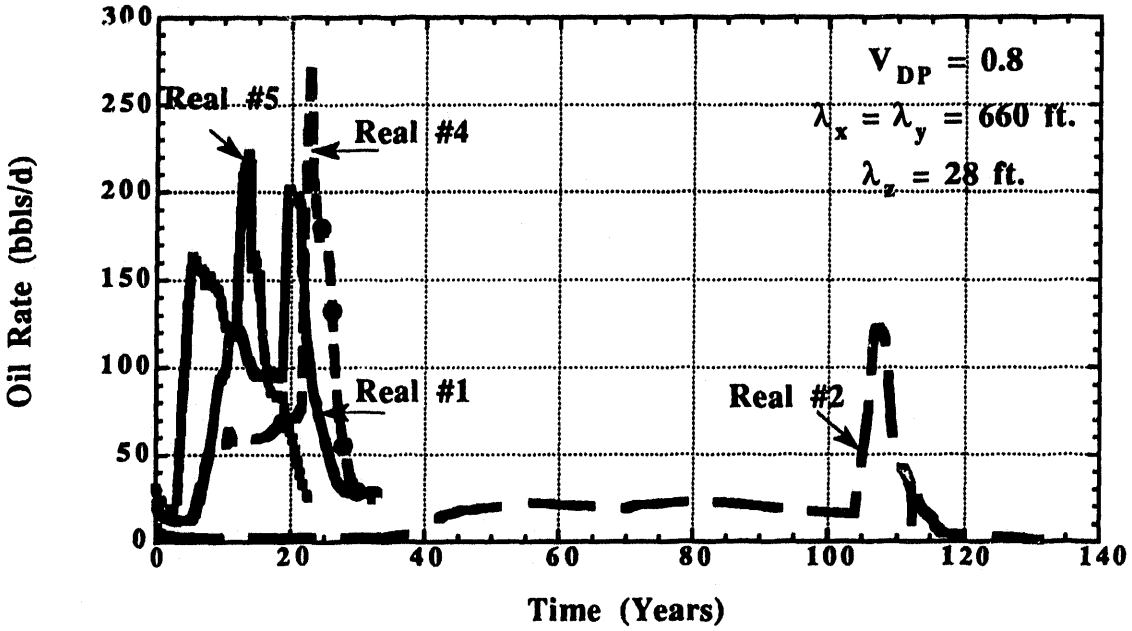

Fig. 67 Comparison of oil production rate between different realizations of the base case permeability field

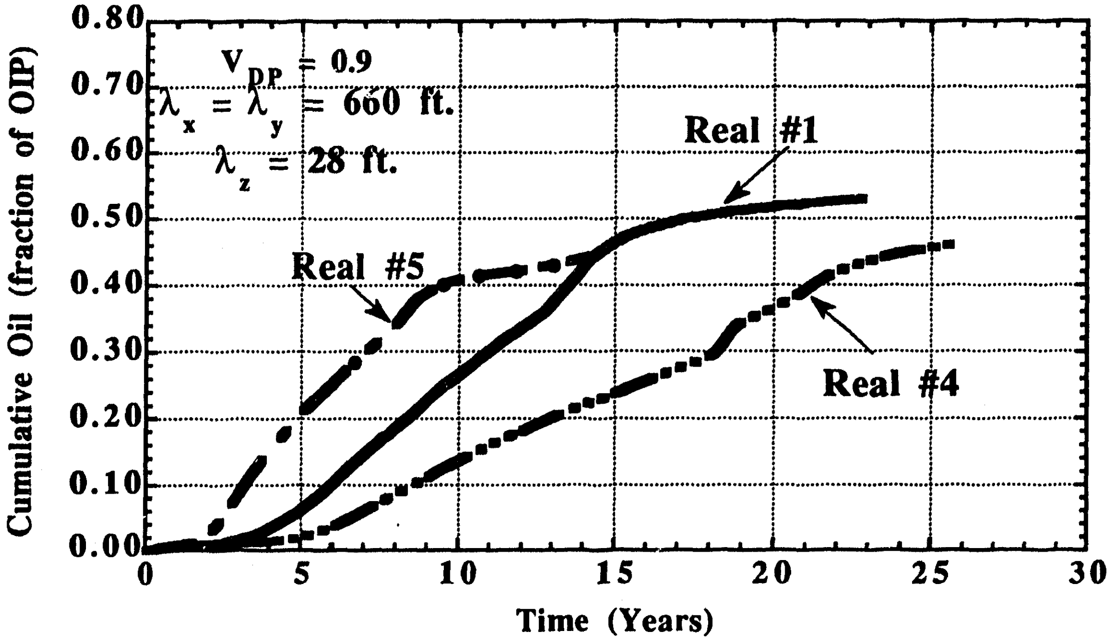

Fig. 68 Comparison between oil recovery for different realizations of the same permeability field

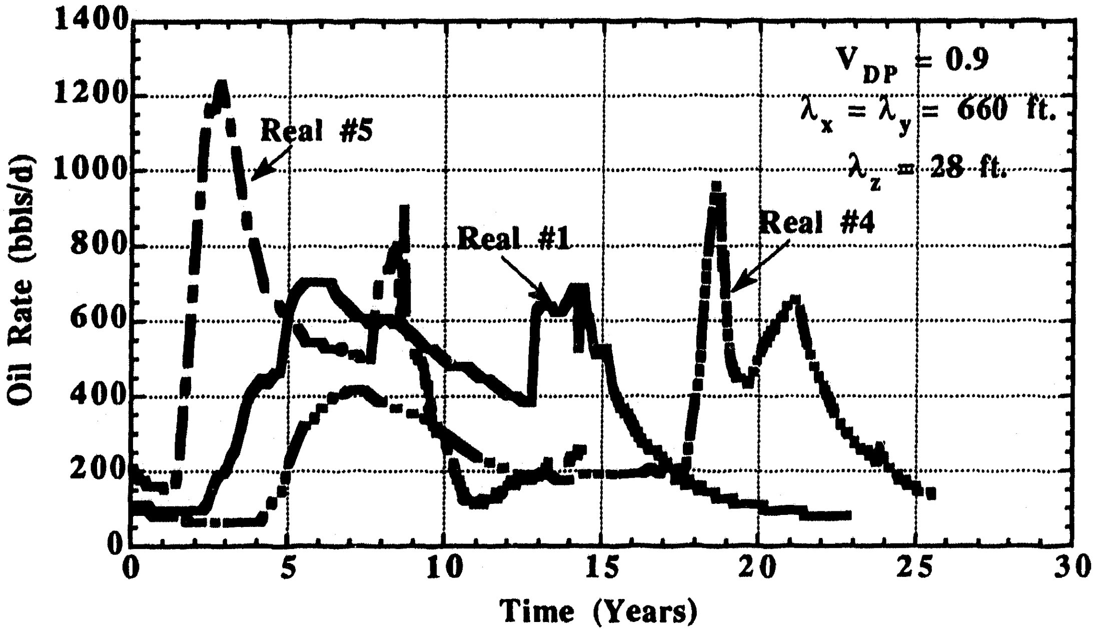

Fig. 69 Comparison between oil rate for different realizations of the same permeability field

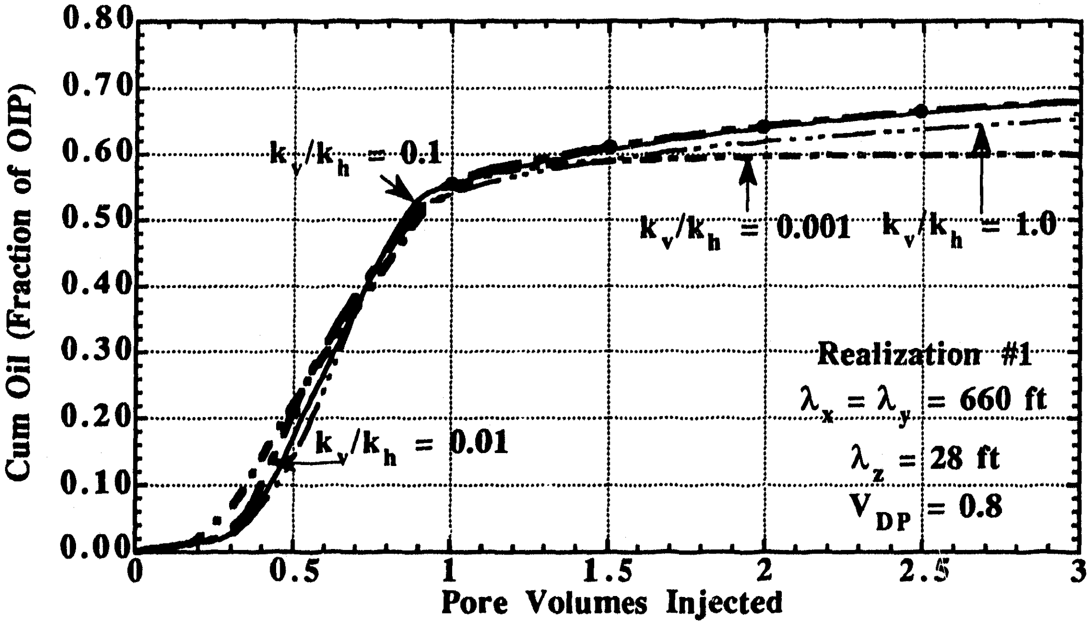

Fig. 70 Comparison between oil recovery for different k_v/k_h ratios

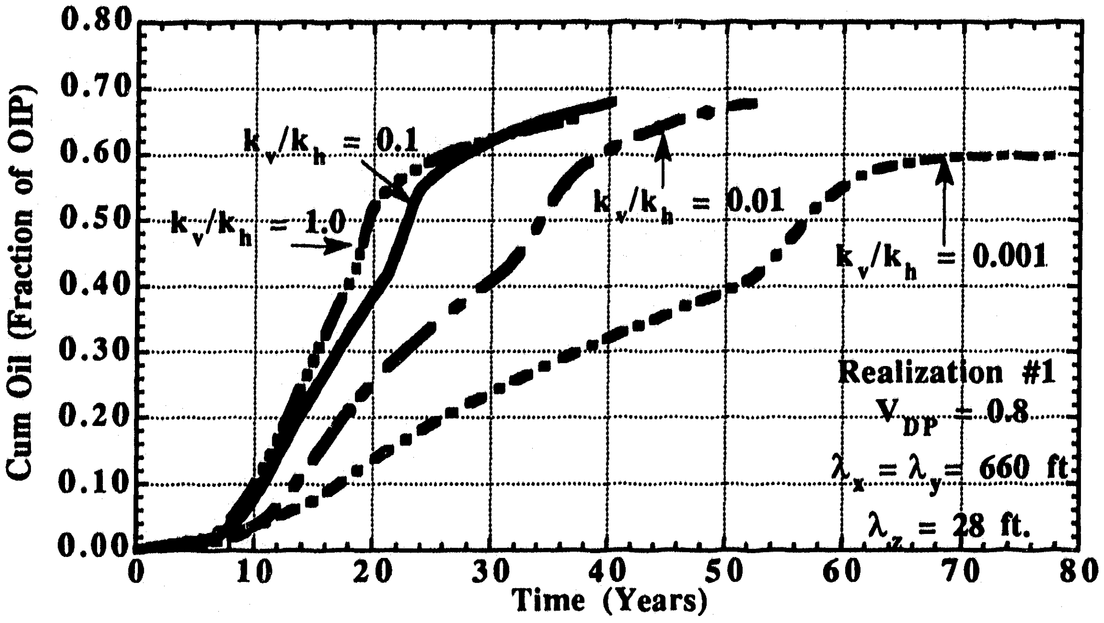

Fig. 71 Comparison between oil recovery for different k_v/k_h ratios

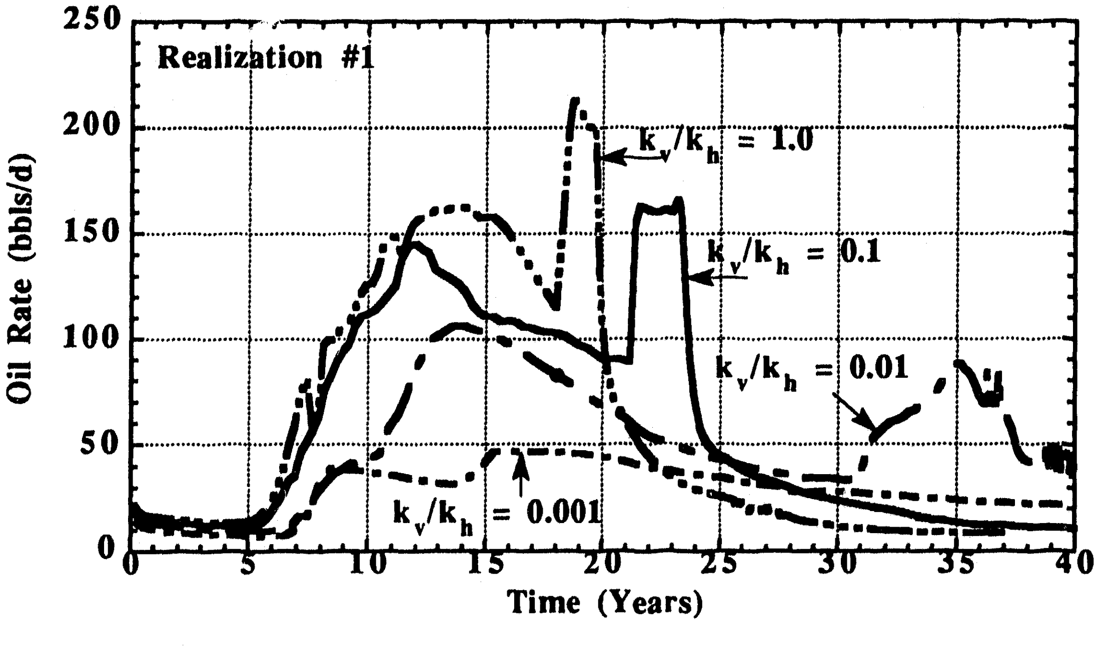

Fig. 72 Comparison between oil rate for different k_v/k_h ratios

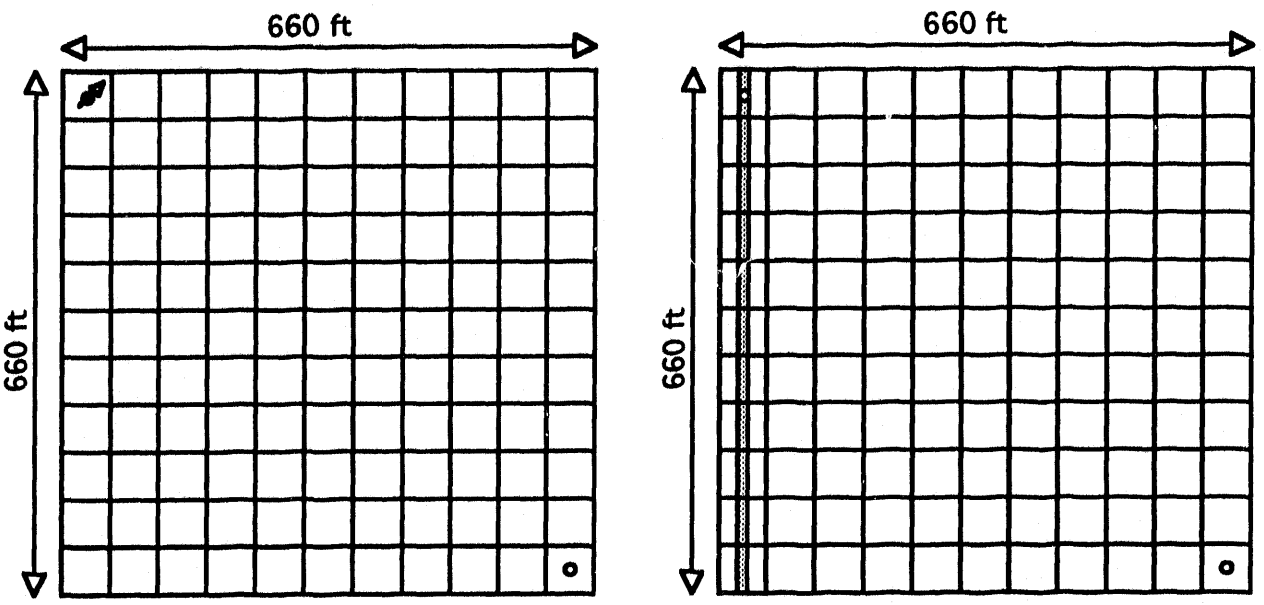

Fig. 73. Areal view of the quarter five-spot grid with a vertical injector and a vertical producer or with a horizontal injector and a vertical producer.

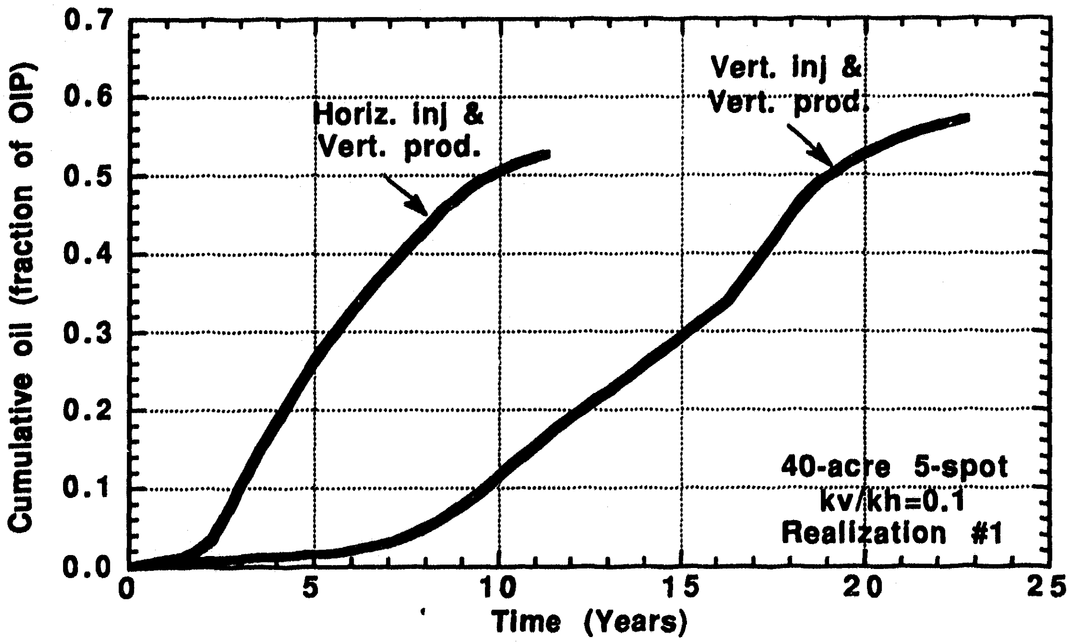

Fig. 74 Comparison of cumulative oil recovery for vertical and horizontal injectors

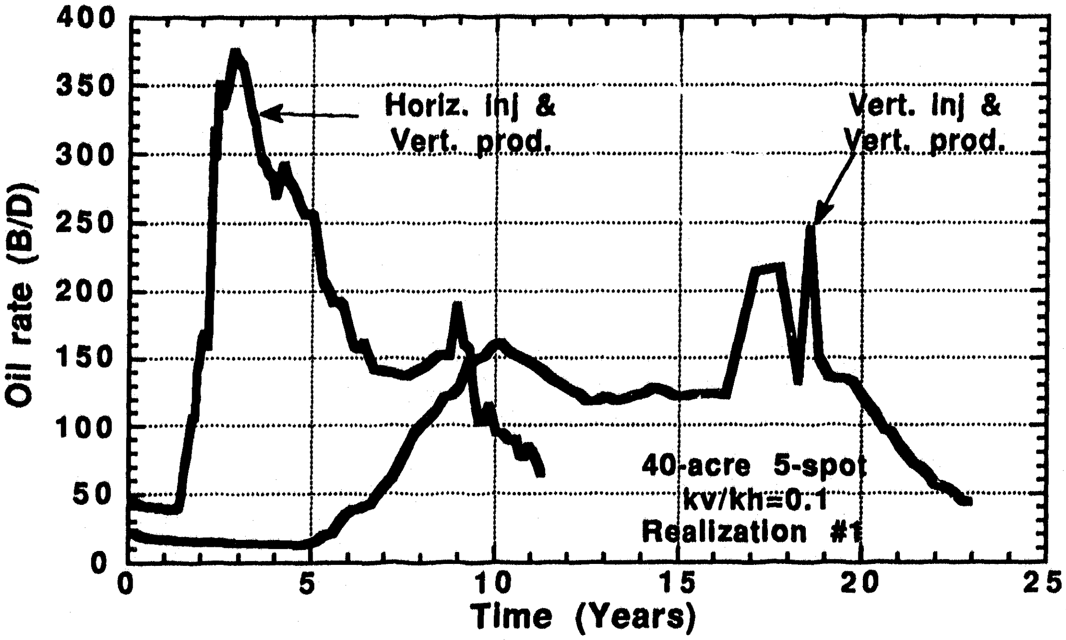

Fig. 75 Comparison of simulated oil rates between vertical and horizontal injectors

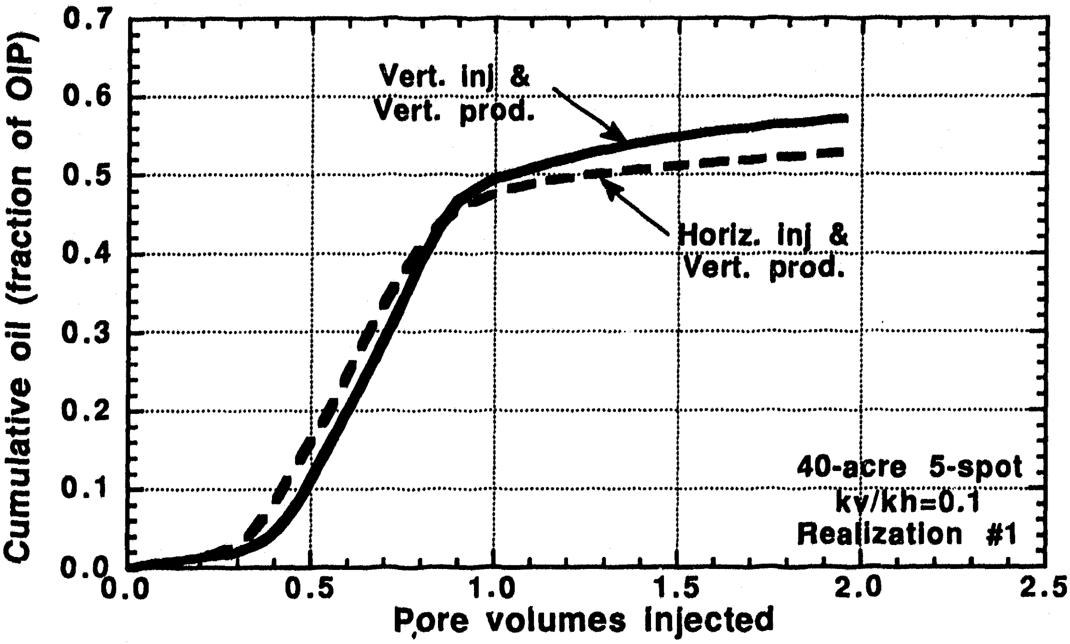

Fig. 76 Comparison of cumulative oil recovery as a function of pore volumes for vertical and horizontal injectors

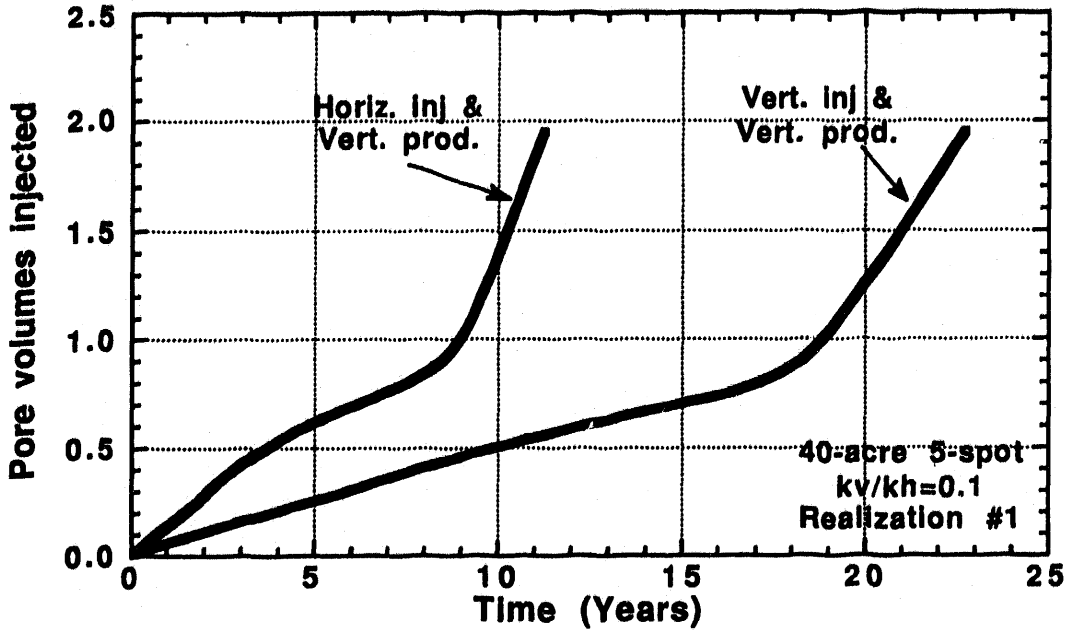

Fig.77 Pore volumes injected versus time from simulations with and without a horizontal injection well

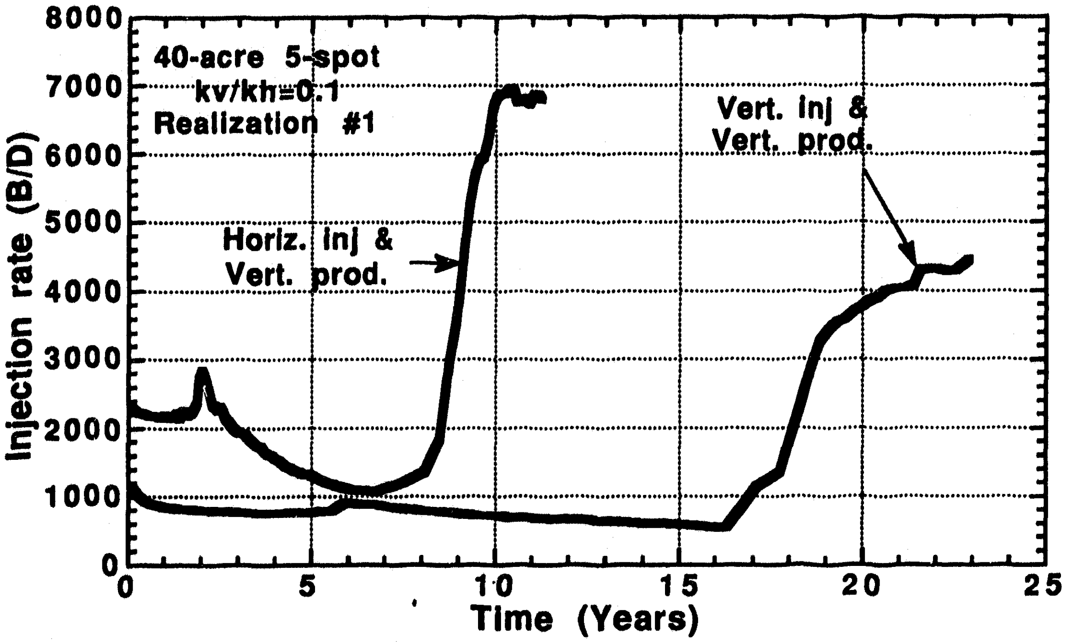

Fig. 78 Injection rates from simulation with and without a horizontal injection well

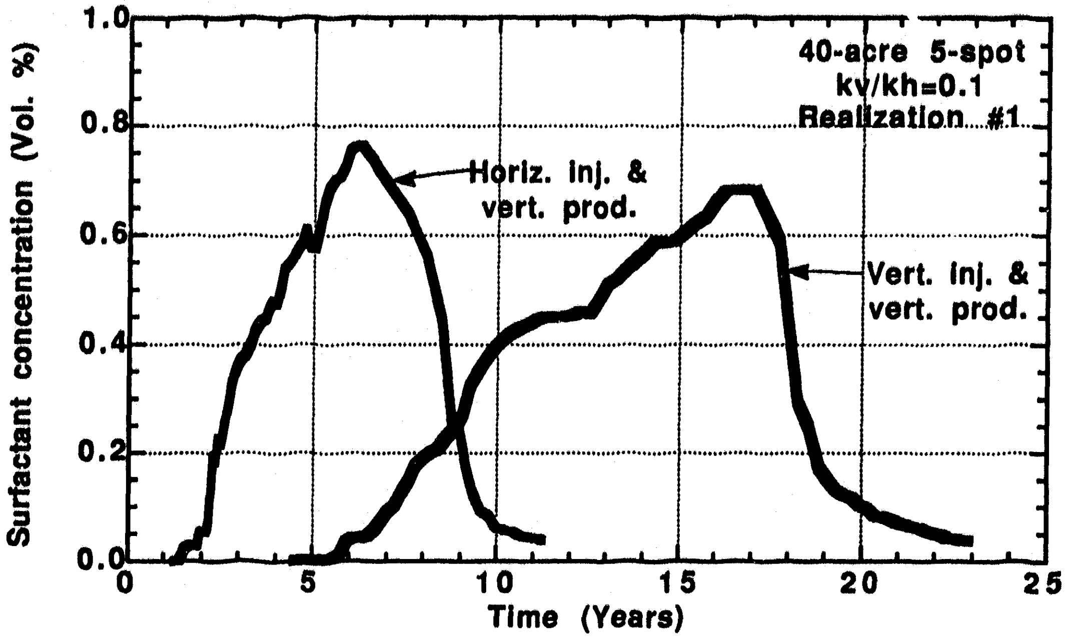

Fig. 79 Surfactant concentration with and without a horizontal injection well

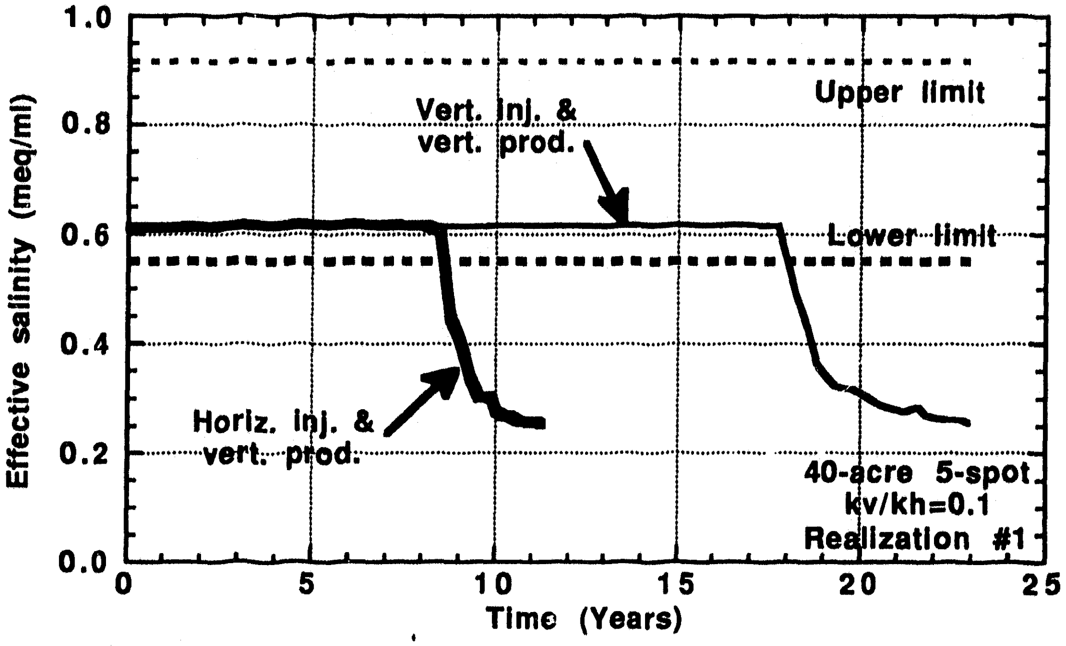

Fig. 80 Effective salinity from simulation with and without a horizontal injection well

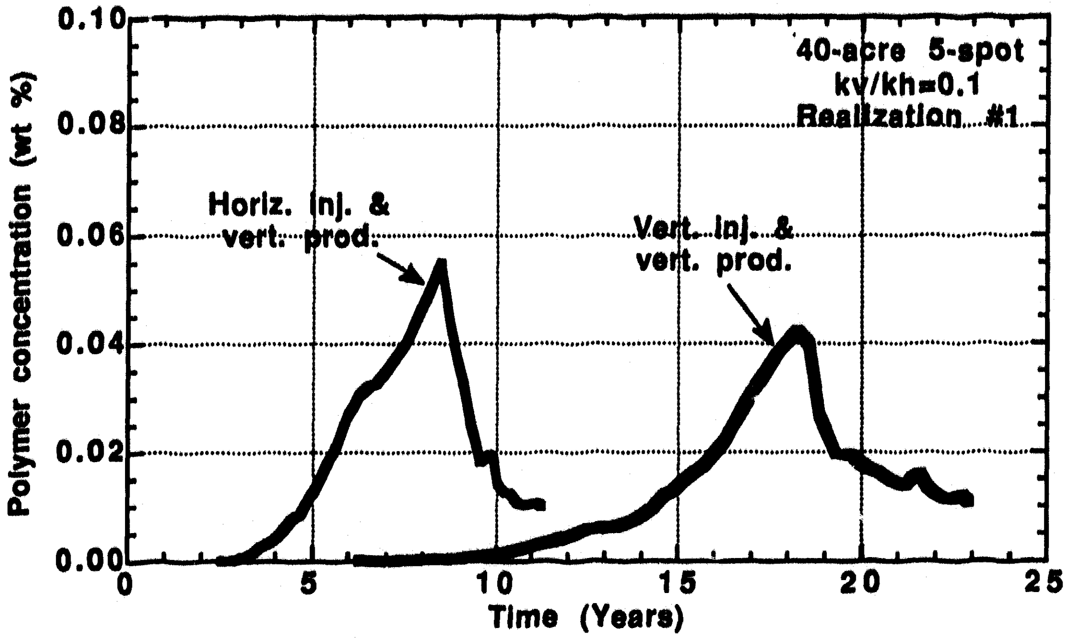

Fig. 81 Polymer concentration with and without a horizontal injection well

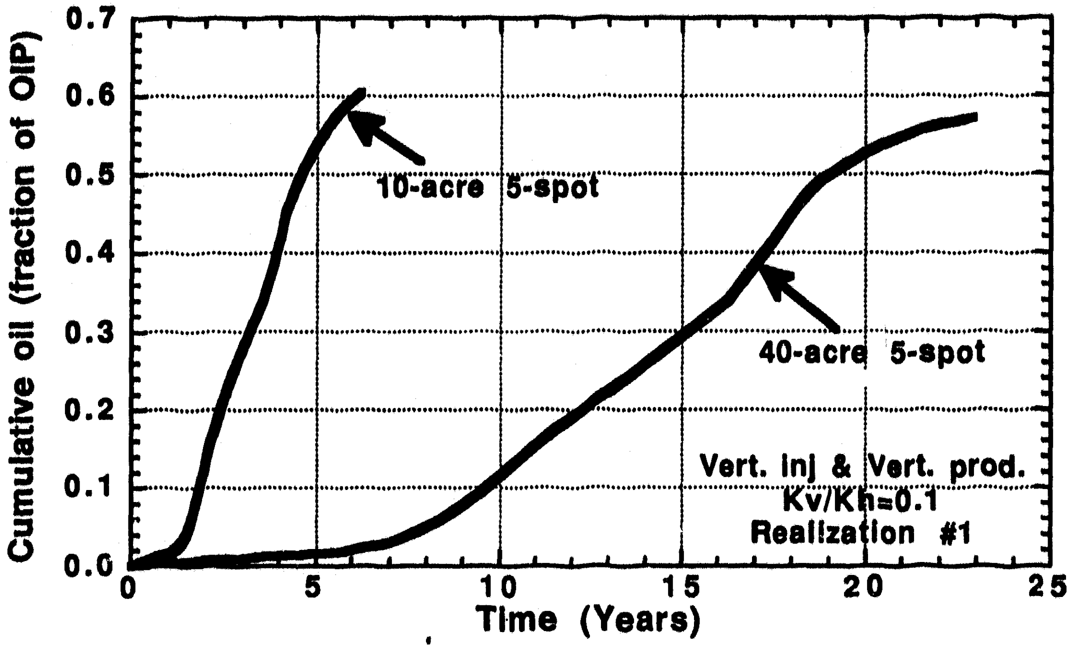

Fig. 82 Effect of well spacing on oil recovery from simulations with vertical wells

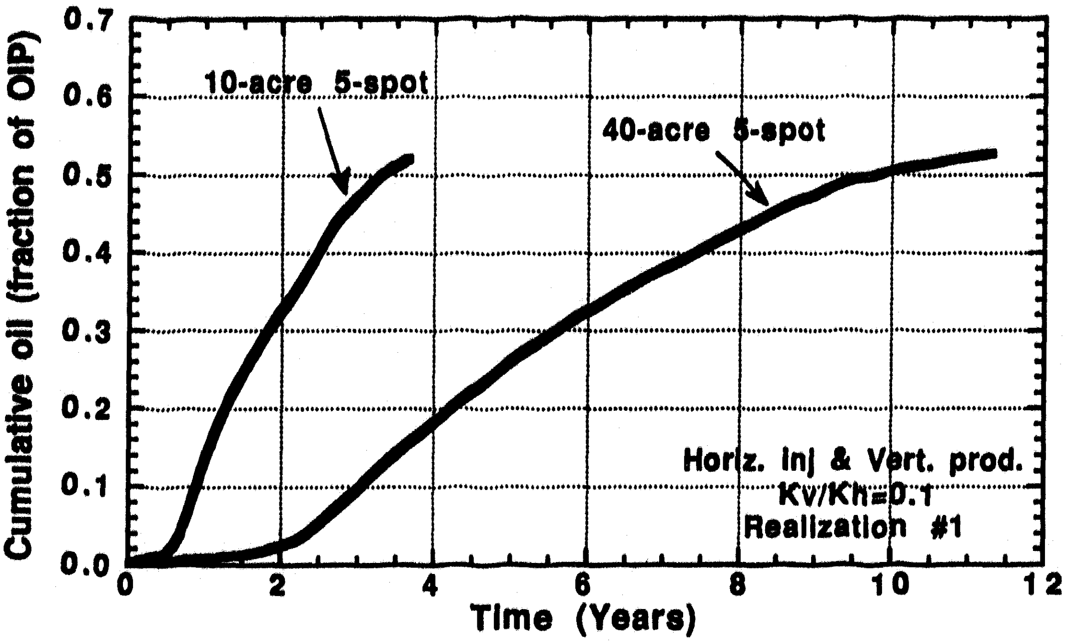

Fig. 83 Effect of well spacing from simulations with a horizontal injection well

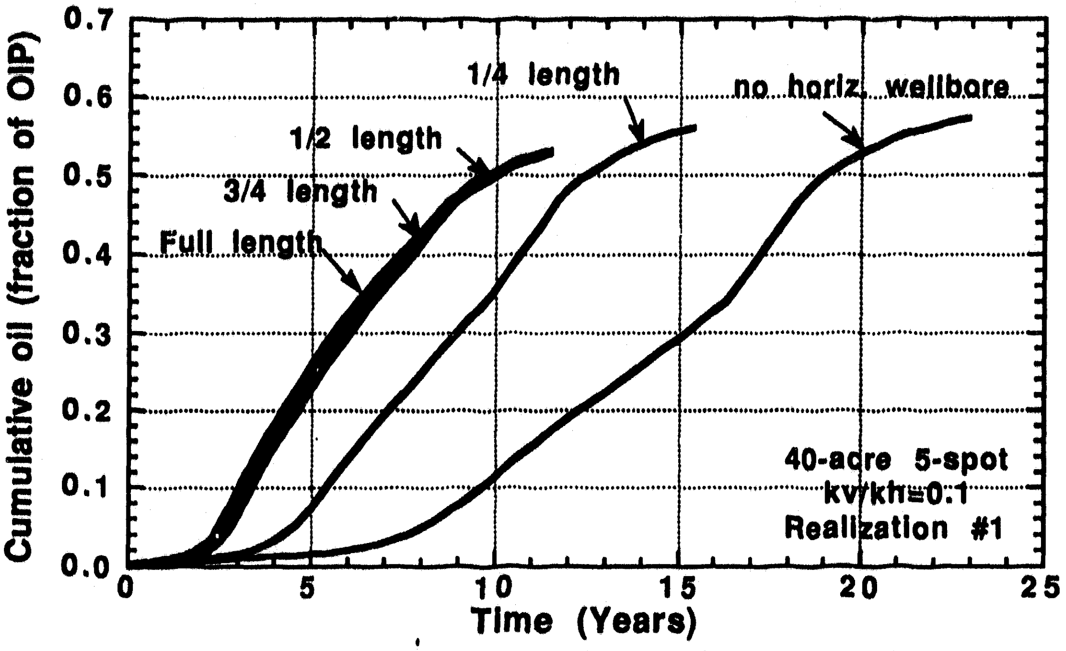

Fig. 84 Effect of the length of the horizontal wellbore on oil recovery

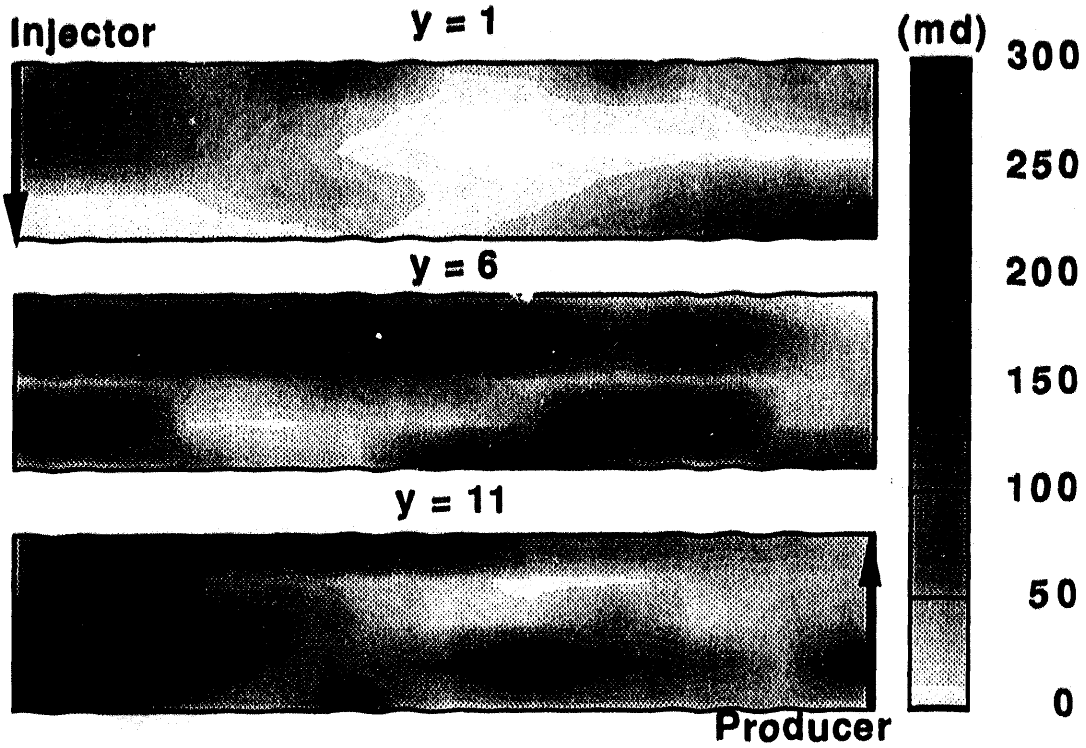

Fig. 85 Vertical x-z slices of the permeability field (Realization #1)

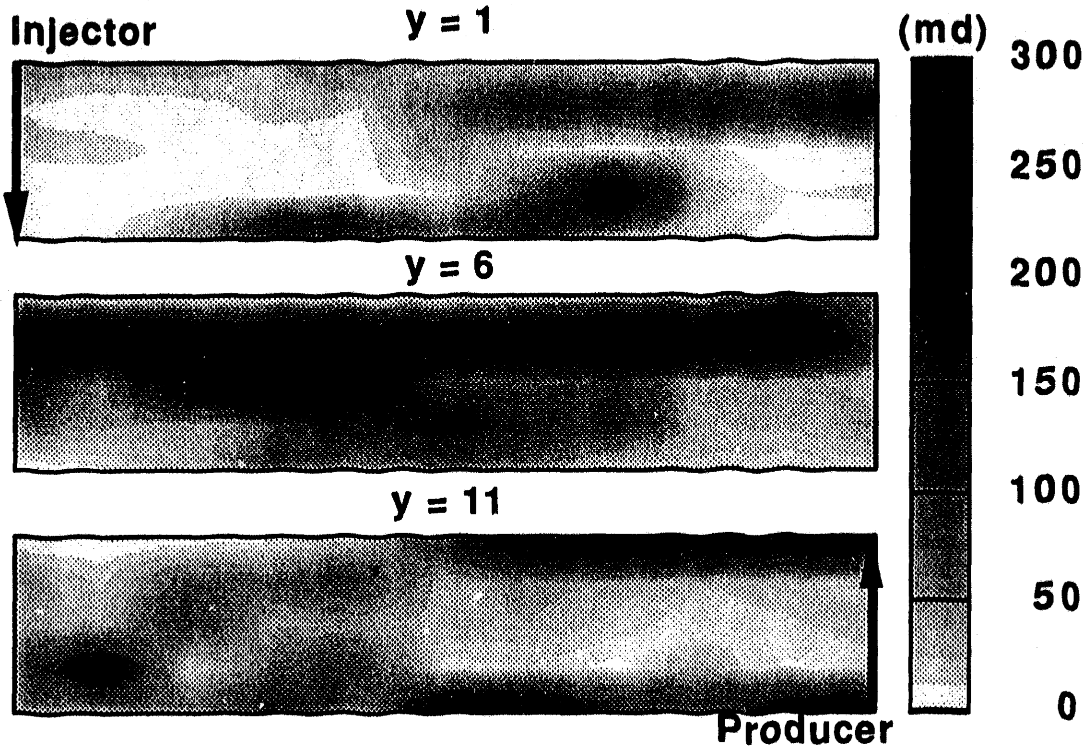

Fig. 86 Vertical x-z slices of the permeability field (Realization #2)

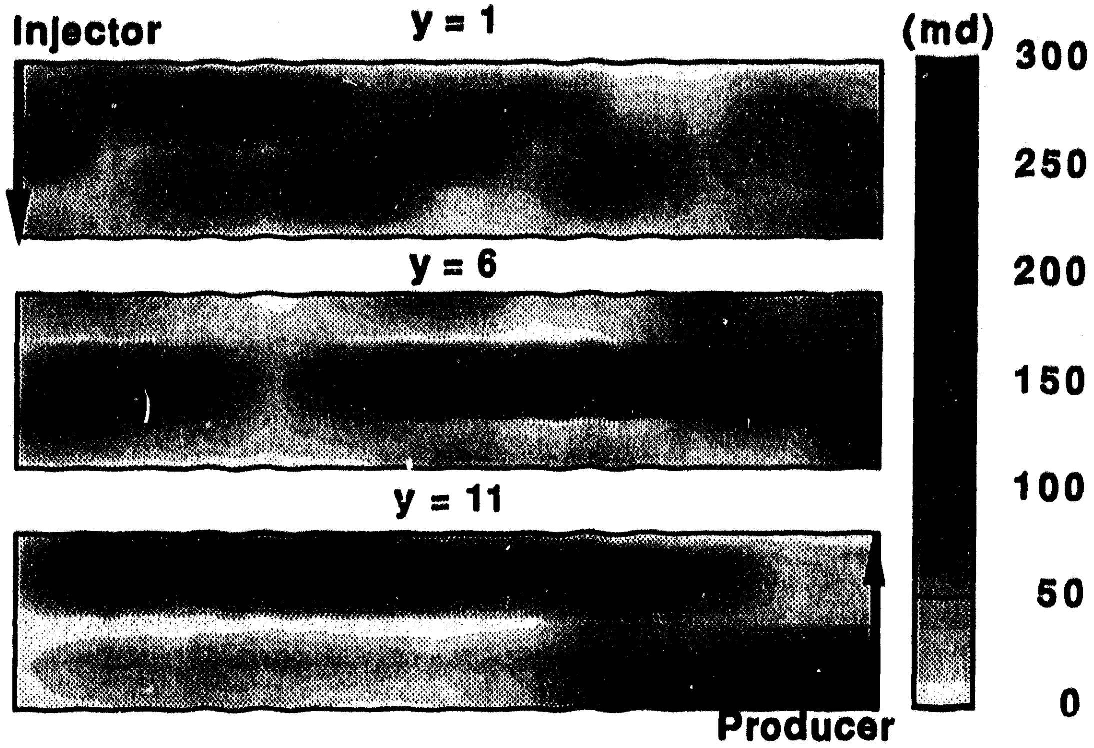

Fig. 87 Vertical x-z slices of the permeability field (Realization #3)

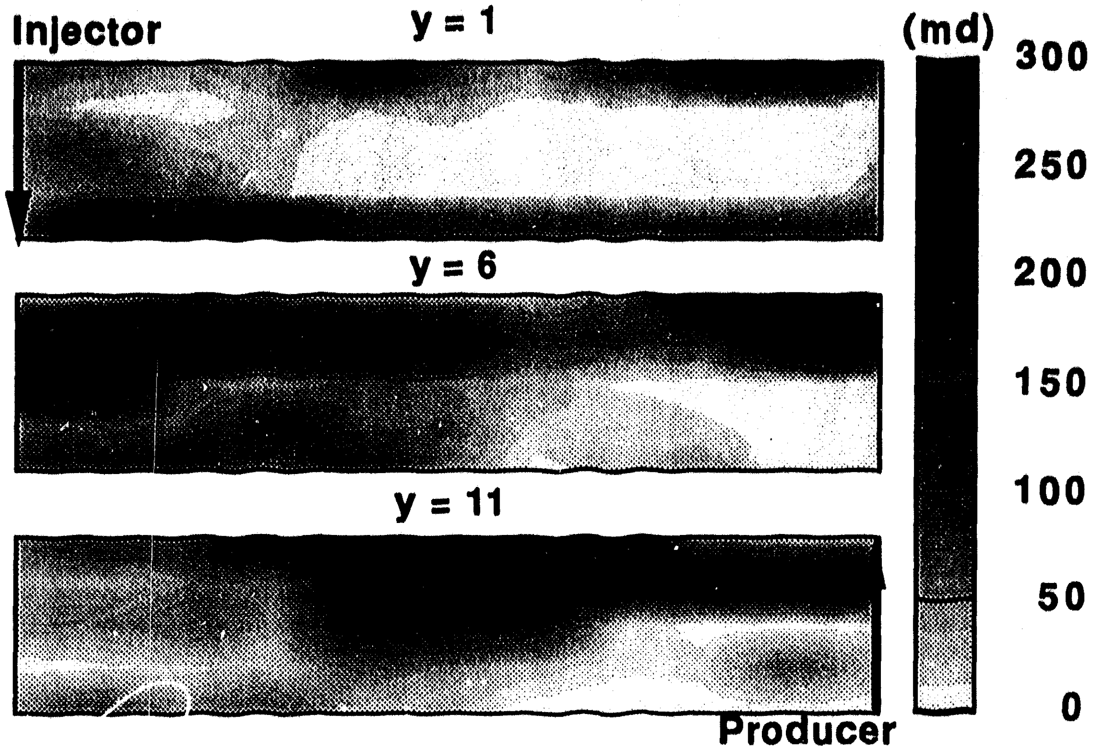

Fig. 88 Vertical x-z slices of the permeability field (Realization #4)

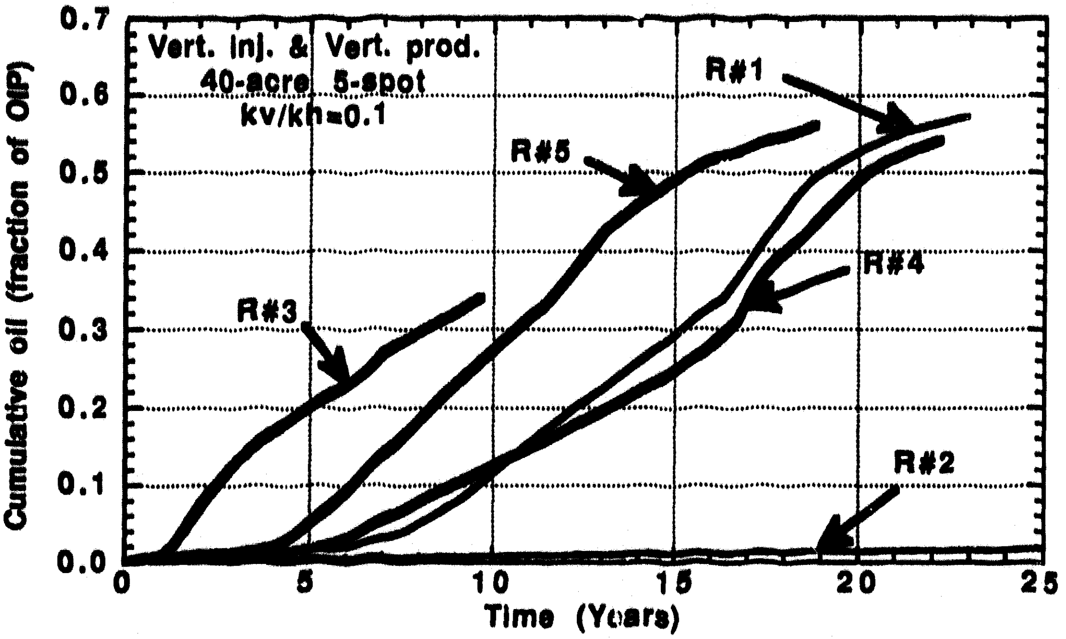

Fig. 89 Effect of different permeability field realizations on oil recovery for a vertical injection well

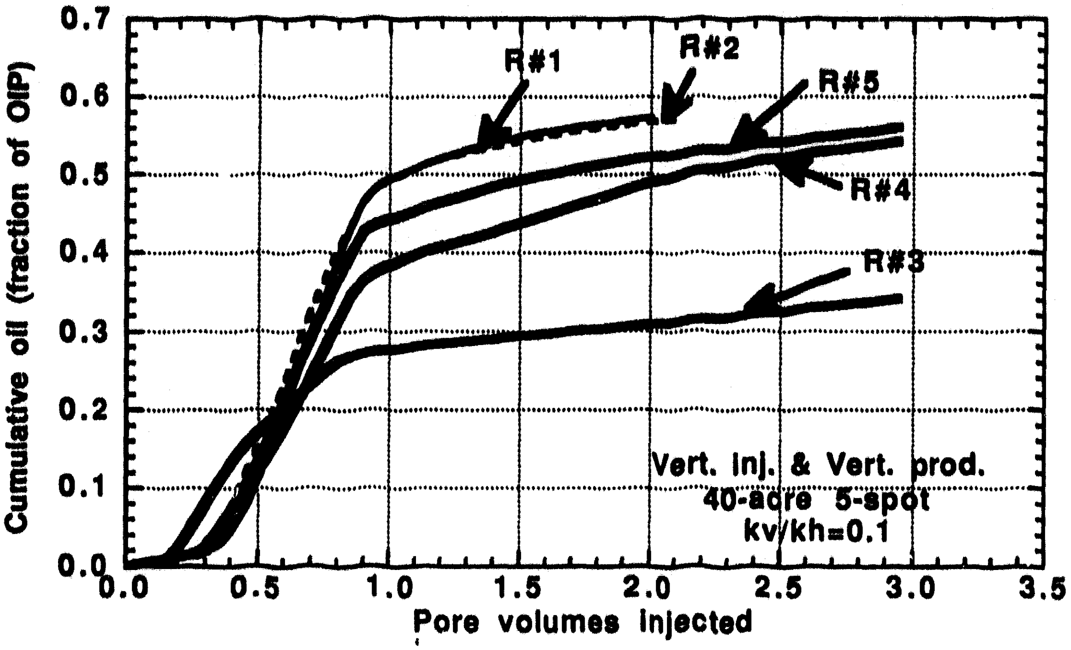

Fig. 90 Effect of different permeability field realizations on oil recovery for a vertical well

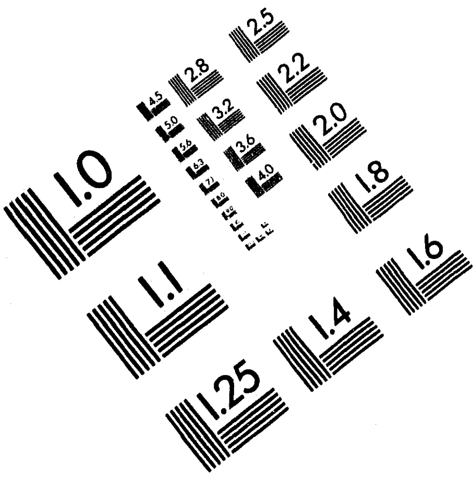

AIIM

Association for Information and Image Management

1100 Wayne Avenue, Suite 1100
Silver Spring, Maryland 20910

301/587-8202

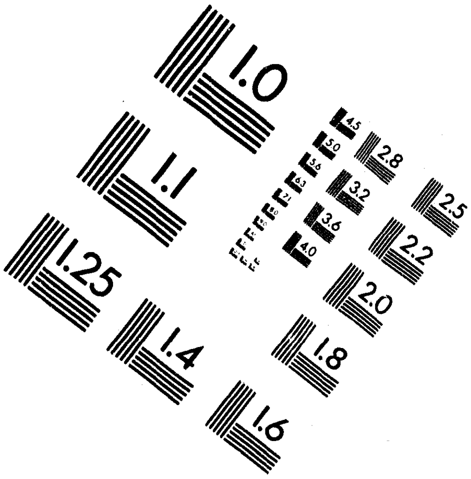

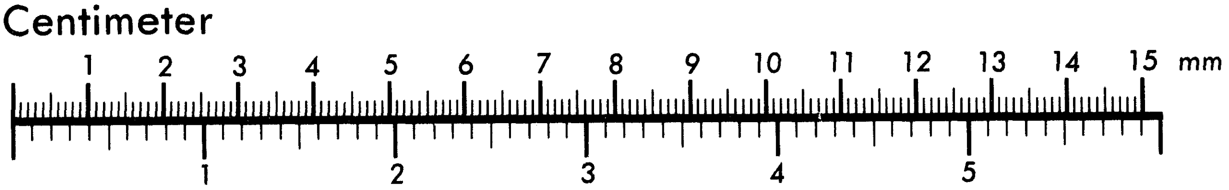

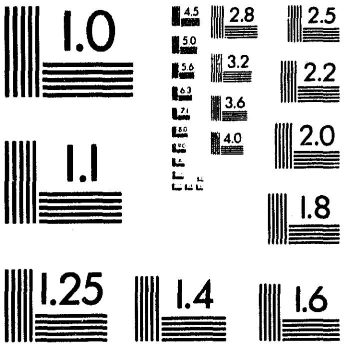

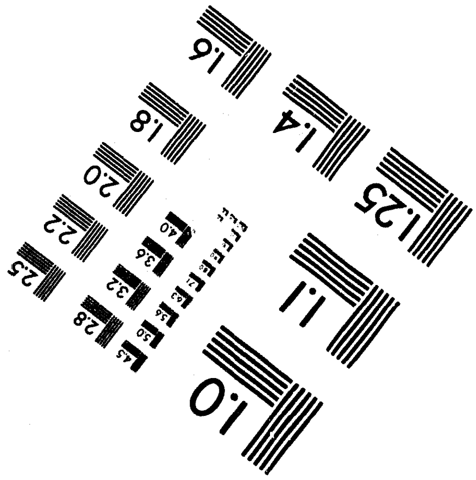

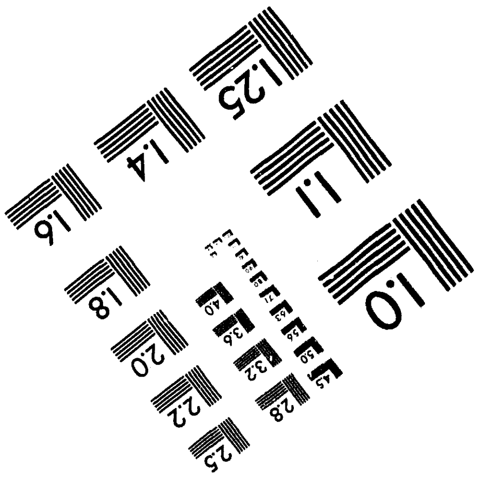

MANUFACTURED TO AIIM STANDARDS
BY APPLIED IMAGE, INC.

2 of 2

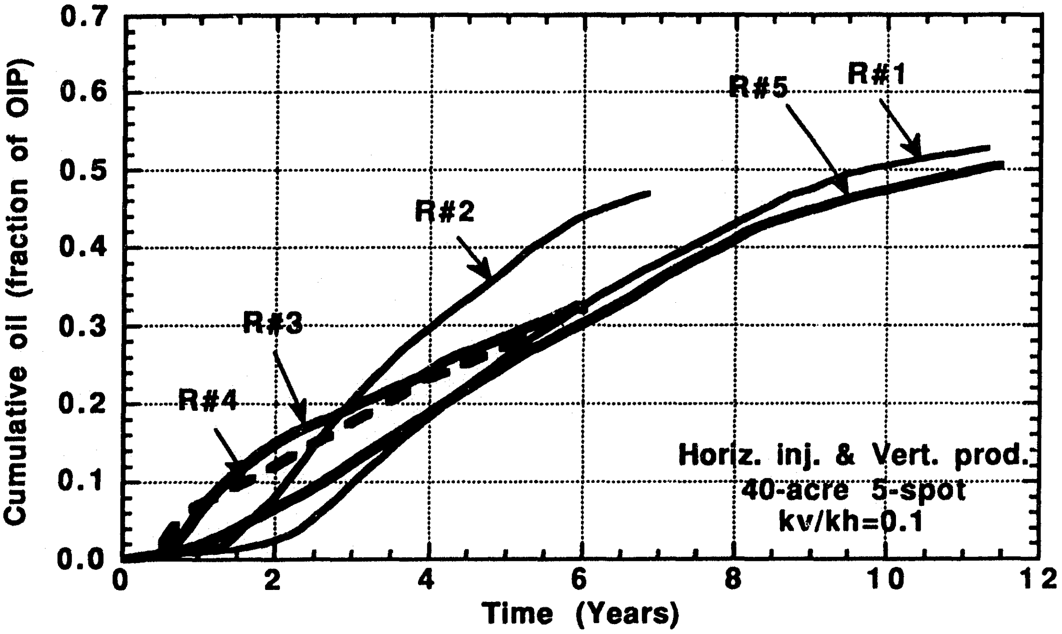

Fig. 91 Effect of different permeability realizations on oil recovery with a horizontal injector

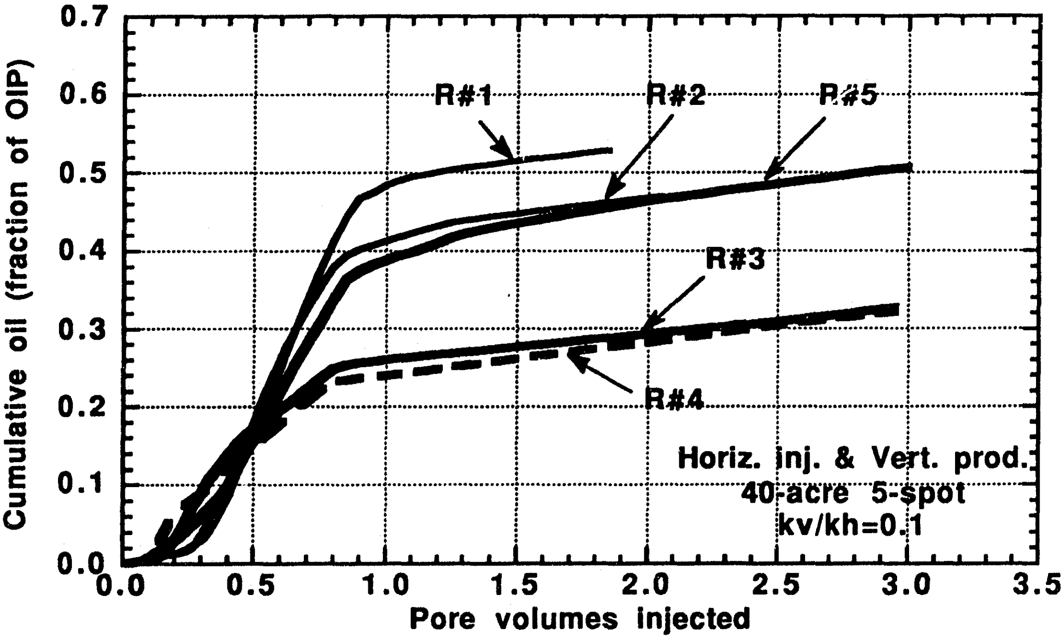

Fig. 92 Effect of the permeability field realizations on oil recovery for a horizontal injector

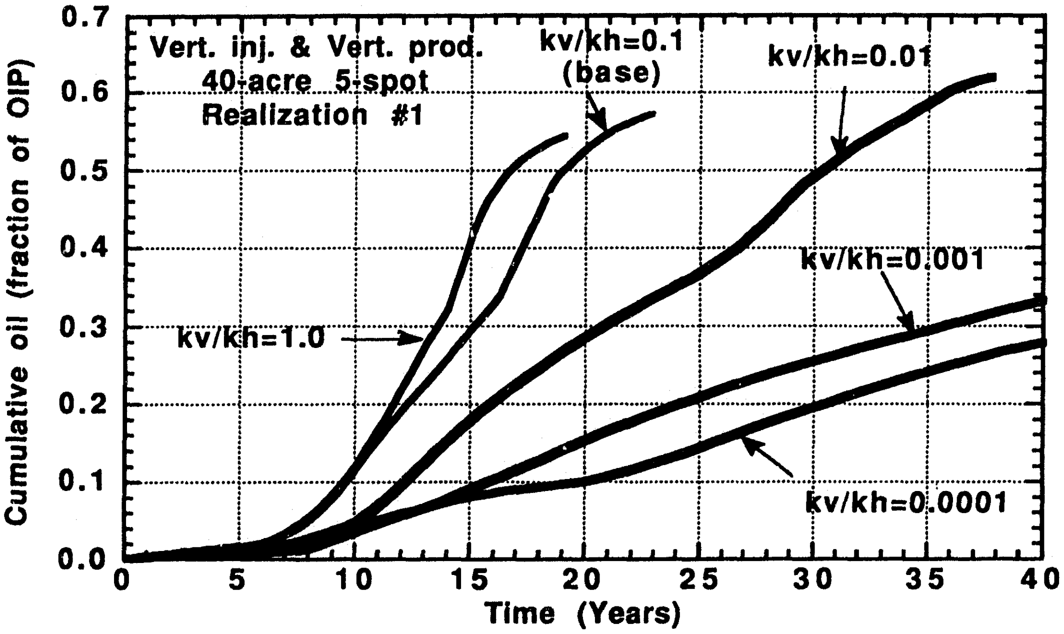

Fig. 93 Effect of the vertical to horizontal permeability ratio on oil recovery for a vertical injector

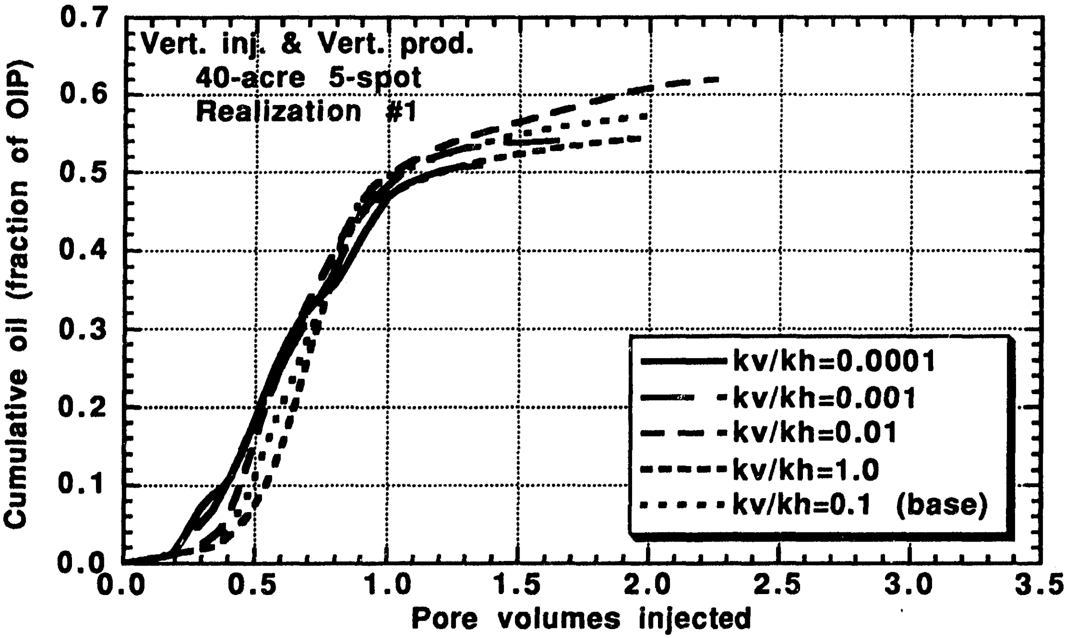

Fig. 94 Effect of the vertical to horizontal permeability ratio on oil recovery for a vertical injector

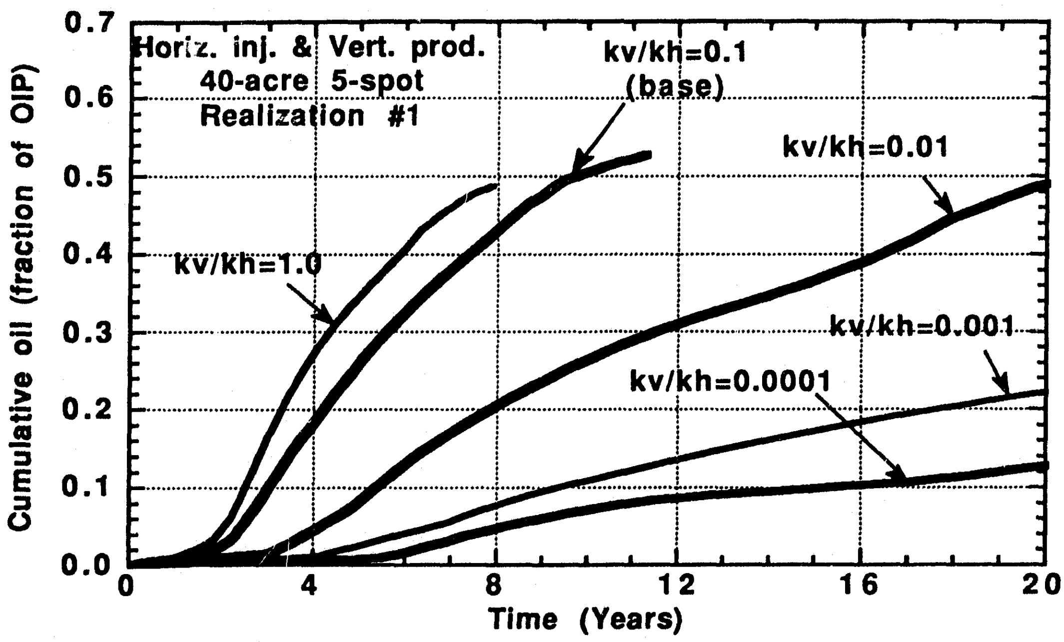

Fig. 95 Effect of the vertical to horizontal permeability ratio on oil recovery for a horizontal injector

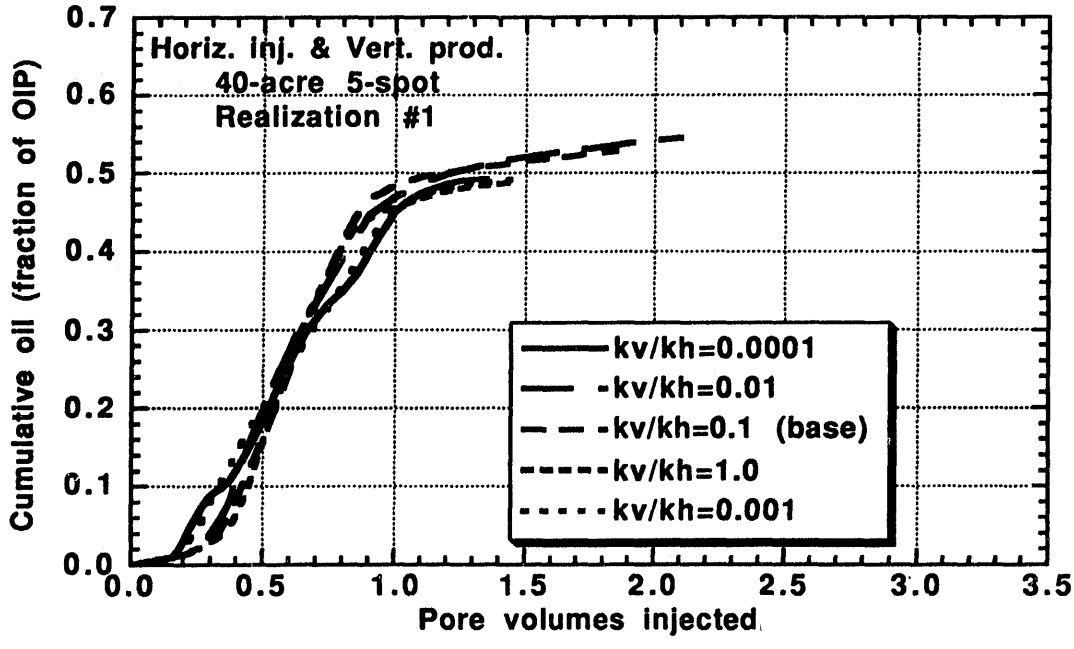

Fig. 96 Effect of the vertical to horizontal permeability ratio on oil recovery for a horizontal injector

☆U.S. GOVERNMENT PRINTING OFFICE: 1994 - 560-030/0[illegible]32

DATE FILMED

9/19/94

END